Studies on dielectric and ferroelectric properties of lead-free $Ba_{0.85}Ca_{0.15}Ti_{0.9}Zr_{0.1}O_3$ bulk ceramics and thin films

A Dissertation

Submitted by

Seelam Rangaswamy Reddy

(Reg. No. 716194)

in partial fulfillment of the requirements for the award of the degree of

Doctor of Philosophy

in

Chemistry

Department of Chemistry

National Institute of Technology

Warangal-506004

India

May 2020

DECLARATION

I, Seelam Rangaswamy Reddy, hereby declare that this dissertation work entitled "Studies on dielectric and ferroelectric properties of lead free $Ba_{0.85}Ca_{0.15}Ti_{0.9}Zr_{0.1}O_3$ bulk ceramics and thin films" submitted in partial fulfillment for the award of **Doctor of Philosophy** (in Chemistry) in the Department of Chemistry, National Institute of Technology, Warangal is a bonafide work which was carried out by me under the supervision of **Dr. Vishnu Shanker** and **Dr. Subir Kumar Roy**. I also declare that the content of this thesis have not been submitted previously in part or full in any University or Institute for the award of any degree or diploma.

Seelam Rangaswamy Reddy

Reg. No. : 716194

Department of Chemistry

CERTIFICATE

This is to certify that the work presented in the dissertation entitled **“Studies on dielectric and ferroelectric properties of lead free $Ba_{0.85}Ca_{0.15}Ti_{0.9}Zr_{0.1}O_3$ bulk ceramics and thin films”** submitted to the National Institute of Technology, Warangal by **Seelam Rangaswamy Reddy** bearing **Reg. No. 716194** for the award of **Doctor of Philosophy** in **Chemistry** is a record of bonafide research work carried out by him under the supervision of Dr. Vishnu Shanker (NIT, Warangal) Dr. Subir Kumar Roy (DMRL, Hyderabad). The results presented in this dissertation have not been submitted in either part or full elsewhere for any research degree.

Internal Supervisor	External Supervisor
Dr. Vishnu Shanker	**Dr. Subir Kumar Roy**
Department of Chemistry	Ceramics and Composites Group
National Institute of Technology	Defence Metallurgical Research Laboratory
Warangal-506004	Hyderabad-500058
Date:	**Date:**

Dedicated

To

My Parents

Acknowledgements

I would like to thank my external supervisor Dr. Subir Kumar Roy for his continuous support, encouragement, patience and guidance thorough out the Ph. D. program. Since I was new to the subject, he taught me all the basics from literature survey to experimental procedures. When I needed his help for my research related problems to personal problems, he was always there to support me. His constant motivation and encouragement helped me to give my best.

I am grateful to my internal supervisor Dr. Vishnu Shanker for believing in me, that I can do better. He polished my technical skills and presentation skills during the course work period. The discussions with him helped me to understand the research problems in different perspective. His continuous support and encouragement helped me to complete this long journey.

I gratefully acknowledge the provision of funding for the research described in this thesis by Defence Metallurgical Research Laboratory, DRDO. I express my gratitude to former Directors of DMRL, Dr. Amol Ghokhle, Dr. S.V. Kamat, Dr. Vikas Kumar, as well as the current Director Dr. G. Madhusudhan Reddy for giving the permission to carry out Ph.D. work and use the facilities of DMRL. I would also like to thank the Head of the Department, Department of Chemistry and Director, NIT, Warangal for giving me the opportunity to register for my Ph. D.

I would like to thank my Doctoral scrutiny committee chairperson (Prof. P. V. Srilakshmi) and members (Prof. K. V. Gobi, Dr. Venkatathri Narayanan, Dr. Asit Kumar Khanra and Prof. M. K. Mohan) of NIT, Waragal and research council members of DMRL, Hyderabad for their valuable and insightful suggestions.

I am grateful to Dr. V. V. Bhanu Prasad, Scientist ‘G’, DMRL, who gave me an opportunity to join his team as a research fellow and gave me to access all the facilities in the laboratory. His valuable support and suggestions throughout this long journey is great fully acknowledged.

I would like to thank Dr. P. Goshal and Mr. Vajinder Singh, Scientist, DMRL for microstructure analysis. The help of Dr. R. P. Mathur and Dr. Himalay Basumatary, Scientist, DMRL for the help in GIXRD and AFM experiments is great fully acknowledged. I would like to thank Dr. A. K. Singh, Scientist, DMRL for his help in XRD characterizations.

I am very thankful to Dr. A. R. James, Dr. A. Srinivas, Dr. Prabahar, Mr. M. L. V. Mahesh and Dr. Sarabjit Singh from DMRL for their help in research work and technical discussion. I would like to acknowledge the support from Dr. Abhay Joshi, Application engineer, Tektronix and Keithley for the electrical property measurements.

I would like to thank Dr. Pawan Kumar, NIT, Rourkela, Dr. Sandip Bysakh, CGCRI, Kolkata, Dr. Saket Asthana, IIT, Hyderabad and Dr. Joydip Joardar, ARCI, Hyderabad for their help in microstructure and electrical property characterizations.

I would like to express my gratitude to all the faculty of the Department of Chemistry, NIT, Warangal for sharing their knowledge and extending my knowledge base.

The support and help of staff members of the Ceramics and Composites Group (CCG), DMRL, Hyderabad and the staff members of Department of Chemistry, NIT, Warangal are gratefully acknowledged. I am also thankful to all admin and library staff from DMRL and NIT for their support in various aspects of the work.

I am grateful to my teachers Mr. Madhu, Mr. Ranganna, Mrs. Nitghtingale, Mr. E. Venkateswarlu, Mr. G. Rangaswamy Reddy, Mr. Trilok, Mr. K. R. K Murthy, Mr. E. J. Reddy and Prof. M. Sayaji Rao for their help, support and motivation at different stages of my life.

My special thanks to my colleagues and friends from DMRL Dr. Rajlaxmi, Dr. Ajeet Kumar, Mrs. Sruthi, Mr. Reshu Sinha, Mrs. Geetha Sree, Mrs. Sahitya, Mrs. Sailaja, Dr. Uma Devi, Dr. Pavan, Mr. Chandra Sekhar, Mrs. Renu, Ms. Swaleha, Mr. Govind, Ms. Soumya, Mr. Praveen and Mr. Samba for their constant motivation and support during the course of this work.

I am very thankful to Mr. Sai Kumar, Mr. Ambedkar, Mr. Suman, Dr. Ramaiah, Mr. Dhanunjay. Mr. Rama rao and all other scholars in the Department of Chemistry, NIT, warangal for their support and encouragement from the Ph.D. course work to thesis submission.

My special thanks to my friends Mr. Pavan Reddy, Mr. Ramesh Babu and Mr. Koteswar Rao, for their support at different stages of this research work.

Finally, I would like to thank my father Panduranga Reddy, my mother Rangalakshmi, my sister Mrs. Mahalakshmi, my uncles and Ms. Jayalakshmi for their support, patience and understanding throughout this long journey. I thank to my brothers Mr. Kishore Reddy, Mr. Dharmendra Reddy, my nephew Rakesh Reddy, my niece Neha, Neeraja, Prathyusha and all other family members for their continuous support and encouragement. Special thanks to my grandmother and grandfather for their blessing and wishes.

Table of contents

List of figures

List of tables

List of symbols

Symbol	**Unit**	**Description**
E	V/cm	Electric field
Q	C	Charge
P	C/cm^2	Polarization
E_c	kV/cm	Coercive field
P_r	C/cm^2	Remanent polarization
P_{SW}	C/cm^2	Switchable polarization
S		Strain
d_{33}, d_{31}	C/N or m/V	Piezoelectric coefficient
k_{33}, $k_{31,}$ k_p		Piezoelectric coupling factor
λ	Å	Wavelength of X-rays
θ	o	Incident angle
d_{hkl}	Å	Interplanar distance
h k l		Miller indices
W	J/cm^3	Energy storage density
η		Energy storage efficiency

C	F	Capacitance
ε_0	F/m	Permittivity of Vacuum
ε_r		Relative permittivity
$\tan \delta$		Dielectric loss
J	A/cm^2	Current density
T_C	^oC	Curie point
T_{CW}	^oC	Curie-Weiss temperature
γ		Diffusivity coefficient
H	GPa	Hardness
ν		Poisson’s ratio

Abstract

Ferroelectric materials have been exploited widely in the form of bulk ceramics, thin films, composites and nano-fibers for energy harvesting, energy storage, pulse power systems, tunable microwave devices, sensor, actuator, sonar and microelectronic (MEMs, NVRAM, DRAM etc.) applications. Currently available PZT ($PbZr_xTi_{1-x}O_3$) based ferroelectric materials in different forms are used for the various electronic applications due to its large piezoelectric coefficients (d_{33} = 590 pC/N for bulk and converse d_{33} = 100 pm/V for film) and higher polarization. However, it is well known that the usage of hazardous lead in the electronic components is being restricted globally. In this context intensive efforts were started to find the lead free ferroelectric materials. Recently, a lead free ferroelectric BCZT ($0.5Ba(Zr_{0.2}Ti_{0.8})O_3$-$0.5(Ba_{0.7}Ca_{0.3})TiO_3$) system was investigated which offered large piezoelectricity (d_{33} = ~620 pC/N). The large piezoelectricity for the BCZT system is comparable to the same of the high-end piezoelectric PZT5H.

The content presented in this dissertation is focused on the synthesis and characterization of lead free ferroelectric BCZT in the form of bulk ceramics, thin films and thicker films. BCZT nano-powders and films were synthesized following sol-gel technique. It is known that chemical synthesis technique offers advantages such as low temperature processing, large surface area covering, cost-effective and better stoichiometry control. The effect of sintering on the microstructure and electrical properties of the BCZT bulk ceramics were investigated. XRD analyses of the synthesized BCZT nano-powders, bulk ceramics and films indicated the presence of the polycrystalline perovskite structure. The powder-XRD patterns obtained from the slow scan of BCZT bulk ceramics as well as the Rietveld refinement of the

GIXRD patterns of the films indicated that the coexistence of tetragonal (*P4mm*) and rhombohedral (*R3m*) phases at room temperature. It was found that the chemical synthesis technique significantly reduced the phase formation and densification temperatures for the BCZT bulk ceramics. The density and electrical property measurements of the BCZT bulk ceramics indicated that the optimum sintering temperature is 1350 ^{o}C. The BCZT ceramics showed high piezoelectric coefficient (converse d_{33} = 680 pm/V) and T_C of 100 ^{o}C. The obtained piezoelectric coefficients for these BCZT bulk ceramics are comparable to that of the soft PZT ceramics. Furthermore, microwave sintering technique was used to produce dense BCZT ceramics. Relative density of 95.2% and T_m of 115 ^{o}C were achieved for the BCZT bulk ceramics by microwave sintering. The T_C of these BCZT ceramics is higher than the same obtained for the solid state route processed BCZT ceramics (93 ^{o}C). In the subsequent study, the effect of processing atmosphere on the microstructure and electrical properties of the BCZT films were systematically investigated. Air-processed BCZT films with ~200 nm thickness displayed giant piezoelectric coefficients (converse d_{33} = ~210 to 250 pm/V). The converse d_{33} of these films is much higher than that of the PZT based films. Processing of BCZT thin films in oxygen-rich atmosphere led to very slim P vs. E hysteresis loops, large dielectric breakdown strength, substantial decrease in coercivity and P_r which enabled to achieve superior energy storage properties. P_{max} of 106 μC/cm^2, P_r of 12.9 μC/cm^2, ESD of 64.8 J/cm^3 and ESF of 73 % was showed by the film crystallized at 800 ^{o}C in oxygen-rich atmosphere. Processing in oxygen-rich atmosphere also significantly reduced the dielectric loss and leakage current density in the BCZT films. Moreover, the oxygen-processed films exhibited excellent polarization fatigue resistance with the recovery of 97 to 99 % of polarization. Nano-mechanical properties were measured on the thicker BCZT films (thickness: ~750 nm) using nanoindentation technique. The results indicated the higher elastic modulus (227±28 GPa) for the films crystallized at 800 ^{o}C temperature. The higher values of elastic modulus of the film annealed at 800 ^{o}C could be correlated to the microstructure and relatively lower porosity.

Chapter 1

Literature Review

This chapter gives brief introduction about ferroelectric materials and their characteristics

Human civilization is greatly influenced by the discovery of various materials and associated materials technology. Historians have distinct time periods such as the Stone Age, the Bronze Age and the Iron Age based on the dominant material in those periods. Each new era was brought by continuous search for superior products by the mankind. Furthermore, this continuous effort from the mankind caused to emerge the “smart” materials technology in early 21st century. Smart materials exhibit various effects relating various inputs such as electric field, magnetic field, stress, heat and light with the outputs like charge/current, magnetization, strain, temperature, light etc. Ferroelectric, piezoelectric, ferromagnetic, multiferroic, conducting and elastic materials belong to the smart materials category. It is well known that conducting and elastic materials produce current and strain outputs respectively on applications of voltage and stress. On the other hand, piezoelectric and pyroelectric materials generate charge with the application of stress and heat respectively. Moreover, these materials exhibit converse effects (Converse piezoelectric and electrocaloric effects) and hence, both sensing and actuating functions can be realized in the same materials. Intelligent materials must have a drive/control or processing function which is adaptive to changes in environment. Ferroelectric materials also show most of these effects hence, these are considered as very smart materials [1].

Ferroelectricty was first discovered in single crystalline Rochelle salt (Sodium potassium tartrate tetra hydrate) in 1921. Since then ferroelectricity was extended for different types of materials such as poly crystalline materials, polymers and biomaterials. Ferroelectric materials have been used in various electronic applications in the form of bulk and thin films due to the unique combination of spontaneous polarization, piezoelectricity and pyroelectricity. For example, ferroelectric bulk materials can be used for capacitors, energy harvesting units, sensors, actuators, ultrasound transducers, sonars, gas igniters, buzzers, microphones etc [2]. Ferroelectric materials in the form of thin films are used for micro system applications such as microelectronic mechanical systems (MEMs), non-volatile random access memory (NVRAM), dynamic random access memory (DRAM), tunable micro wave circuits and high energy storage capacitors [3-5].

1.1 Classification of crystalline materials

All the crystalline materials were categorized in to 32 crystal point groups based on the symmetry elements present in the crystals. Among the 32 crystal point groups 11 are centro symmetric point groups and remaining 21 are non-centro symmetric groups which lacks the centre of inversion. Among the 21 non-centro point groups the crystals that belong to 20 groups can exhibit piezoelectricity. However 10 point groups among these 20 groups possess unique polar axis which generates spontaneous electric moment. The crystals with unique polar axis also develop electric charge when these are uniformly heated. This phenomenon is called as pyroelectricity. Therefore, all the pyroelectric crystals can show piezoelectricity. A subgroup of the pyroelectric materials is ferroelectric materials where spontaneous electric dipoles can be reversed by applying the electric field [2, 6]. The relation of pyroelectric coefficient with the temperature is given in equation (1.1).

$$D_i = \Delta P_{S,i} = p_i \, \Delta T \qquad (1.1)$$

Where D_i denotes the surface charge density, T denotes the temperature, $P_{s,i}$ is the vector of spontaneous polarization and p_i (C m^{-2} K^{-1}) is the vector of the pyroelectric coefficient [7].

1.2 Ferroelectricity

Ferroelectricity is the phenomenon of electric dipole reversibility or polarization reversal with altered applied electric field. Ferroelectric materials show permanent spontaneous polarization through spontaneous electric dipoles. All the ferroelectric materials are piezoelectric materials. In contradictory all the piezoelectric materials are not ferroelectric materials [2, 5, 6]. For example, ZnO and AlN are piezoelectric materials but these do not show the ferroelectricity [4]. Ferroelectric materials exhibit very high spontaneous polarization and high remanent polarization (P_r). In addition to this, ferroelectric materials also show high dielectric constant. The polarization response of ferroelectric materials with respect to the applied electric field is non-linear. The occurrence of hysteresis loop is due to the domain wall motion and with preferred individual domain orientation instead of aligning in the applied electric field direction during polarization reversal. The spontaneous polarization is the polarization associated from the spontaneously formed electric dipoles. Rochelle salt, $BaTiO_3$, Bi_4TiO_{12}, $PbTiO_3$, $(Na/K)NbO_3$, $SrTiO_3$, PMN ($Pb(Mg/Nb)O_3$), etc. are the examples for the ferroelectric materials.

1.3 Piezoelectricity

Piezoelectricity was first discovered in quartz and tourmaline by Curie brothers in 1880. The term piezo is derived from the Greek which means ‘to press’. Therefore, piezoelectricity is the generation of electricity by mechanical stress [2]. In piezoelectric materials the applied mechanical stress (X_{jk}) creates proportional electric charge i.e. dielectric displacement (D_i) and conversely an applied electric field (E_k) generates proportional strain (x_{ij}) due to contraction or expansion of the material. The former effect is called as "Direct piezoelectric effect" and the proportionality constant is called as "direct piezoelectric coefficient" [6]. The units for the direct piezoelectric coefficient are coulombs per Newton (C/N). The latter effect is known as converse piezoelectric effect and the proportionality constant is called "converse piezoelectric coefficient". The units for converse piezoelectric coefficient are meters/Volt (m/V). Here the electric field and dielectric displacement are vector properties whereas the stress and strain are tensor properties [7]. Hence, these are indicated with subscripts. The direct and converse piezoelectric effects are expressed as,

$$Di = d_{ijk} X_{jk} \qquad (1.2) \qquad \text{Direct piezoelectric effect}$$

$$x_{ij} = d_{kij} E_k \qquad (1.3) \qquad \text{Converse piezoelectric effect}$$

Where, d_{ijk} is the direct piezoelectric coefficient and d_{kij} is the converse piezoelectric coefficient. The direct and converse piezoelectric coefficients are thermodynamically identical. The sign of the piezoelectric coefficient is either +ve or –ve since the sign of the dielectric displacement or strain dependent on the direction of the applied mechanical stress or electric field. Mostly, piezoelectric response of the material is recorded in the direction of applied electric field or stress. This is known as 'longitudinal piezoelectric response'. The longitudinal piezoelectric coefficient is usually determined by applying the stress in 3 fold axis direction and by simultaneously measuring the dielectric displacement from the same direction (Here the coefficient is denoted as 'd_{33}'). Apart from this, piezoelectric coefficient is also measured in the direction perpendicular (transverse) to the 3 fold axis direction or vertical direction and it is denoted as 'd_{31}'. High piezoelectric coefficients are desired for the sensor and actuator applications.

However, the overall strength of the electromechanical effect is determined by the measurement of “piezoelectric coupling factors” such as k_{33}, k_{31} and k_p. Piezoelectric coupling factor (k) is the square root of the ratio of output electrical energy to total input mechanical energy or vice versa. Piezoelectric coupling factor is always less than unity since the conversion of either mechanical energy to electrical energy or electrical energy to mechanical energy is incomplete. The typical k values for quartz, $BaTiO_3$ and PLZT ceramics are 0.1, 0.35 and 0.72 respectively [2, 6]. Direct piezoelectric effect is used for sensing applications where as the converse effect is used for actuator applications. To exhibit piezoelectricity the crystals in material must have the polarity in one or some of its crystallographic axes. However, the crystals with polarity don’t deliver sufficient piezoelectric response due to orientation of the adjacent electric dipoles in different directions. In order to obtain maximum piezoelectric response the electric dipoles of the piezoelectric material must be aligned in one particular crystallographic axis by poling. The poling of the ferroelectric material is similar as the magnetization of the ferromagnetic material [2, 7]. Quartz (SiO_2), Zinc Oxide (ZnO), Polyvinylidene fluoride $(CH_2CF_2)_n$, Aluminum nitride (AlN), Lead zirconate titanate ($Pb(Zr/Ti)O_3$, etc. are the examples for piezoelectric materials.

1.4 Perovskite structure

Most of the commercial piezoelectric materials are exist with the perovskite crystal structure. The term ‘perovskite’ was driven from the perovskite mineral i.e. $CaTiO_3$. Perovskite structure is with ABO_3 composition. Perovskite structure is described using simple cube with larger cations (A) at the corners of the cube, smaller cations (B) at the centre of the cube and oxygen ions (O) at the centre of the faces. The oxygen ions are linked to the adjacent octahedra. However, some chlorides, fluorides, nitrides, hydrides, sulfides and carbides have the perovskite crystal structure.

Ferroelectric materials undergo phase transition from high temperature para electric phase to low temperature ferroelectric phase. This transition point is known as "Curie point". The crystal structure of the paraelectric phase is cubic whereas the same for ferroelectric phase is distorted cubic. In the distorted perovskite the smaller cation is moved little away from the centre of the octahedra. The asymmetry in the B-O bond length leads to distortion in the octahedra which generates polarity. The stability of the perovskite structure is evaluated by 'Goldschmidt tolerance factor' [8]. The tolerance factor (t) is calculated using the equation,

$$t = \frac{r_A + r_O}{\sqrt{2}\,(r_B + r_O)} \qquad (1.4)$$

where $r_{A,}$ r_B and r_O are the ionic radius of larger cation, smaller cation and anion, respectively. The (t) value will be in the range of 0.95-1.0 for the cubic phase and the same will be little above 1 for the ferroelectric phase. The magnitude of t for the perovskite can be tailored by substitution with the various cations to achieve the desired ferroelectric structure [6, 9]. $BaTiO_3$, PZT ($Pb(Zr/Ti)O_3$), $SrTiO_3$, $PbTiO_3$, $PbZrO_3$, $CsGeCl_3$, etc. are with perovskite structure. The perovskite structure of $BaTiO_3$ is shown in the Fig. 1.1 (a). The smaller cation in the distorted perovskite moves up and down under the altered electric field [10]. The up and down movements of smaller cation from the centre of octahedra in the distorted perovskite lead to positive and negative polarization states respectively [Fig. 1.1 (b) and 1.1 (c)].

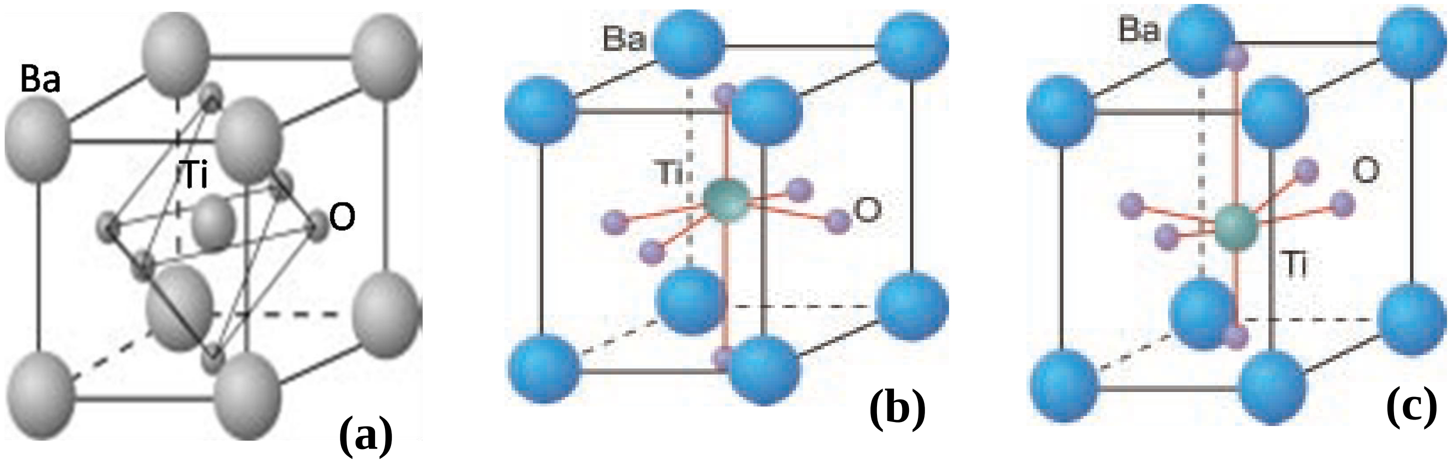

Fig. 1.1 (a) Perovskite structure of $BaTiO_3$ above the Curie point, (b) and (c) shows the positive and negative polarization states below the Curie point (After C. H. Ahn et al. [10]).

1.5 Phase transition in ferroelectric materials

Ferroelectric materials undergo phase transition when these materials are subjected to high temperature. Low-temperature ferroelectric phase is changed to high-temperature paraelectric phase in this transition. Moreover, the ferroelectric phase is with low symmetry whereas the paraelectric phase is with high symmetry [6]. The phase transition temperature is called as the 'Curie point' and it is denoted with 'T_C'. Thermodynamic properties such as dielectric, elastic and thermal properties show anomalies near the phase transition and it is accompanied with changes in dimensions of the unit cell [Fig.1.2]. Above the T_C dielectric constant of the ferroelectric materials is decreased with the temperature according to the Curie-Weiss law [7].

$$\varepsilon = \varepsilon_0 + \frac{C}{T-T_0} \approx \frac{C}{T-T_0} \qquad (1.5)$$

Where 'C' is the Curie constant and T_0 ($T_0 \leq T_C$) is the Curie-Weiss temperature. Both the Curie point and Curie-Weiss temperature may be identical for the second order phase transition of the ferroelectric materials. For first order phase transitions Curie-Weiss temperature is lower than that of the Curie point ($T_0<T_C$).

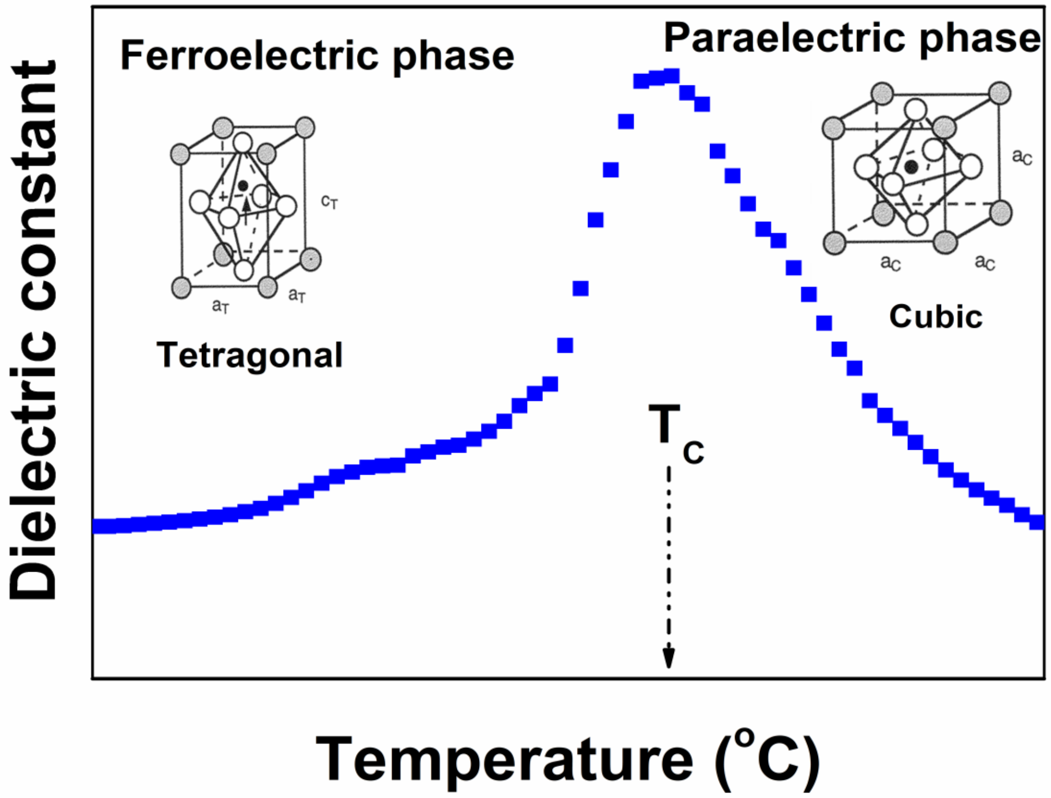

Fig. 1.2 Variation of dielectric constant with temperature at Curie point.

1.6 Ferroelectric hysteresis loops

Ferroic materials (Ferroelectric, ferroelastic or ferromagnetic materials) display hysteresis loops with respect to the external driving forces (Electric field, stress or magnetic field) due to presence of the domain structure. Each kind of ferroic material has its own hysteresis loop like finger print which contains the information related to its properties and structures [11]. Besides, polarization the applied electric field also generates strain in the ferroelectric materials due to the presence of ferroelastic domains. Therefore, ferroelectric materials exhibit polarization (P) vs. electric field (E) and strain (S) vs. electric field (E) hysteresis loops.

1.6.1 Polarization versus electric field hysteresis loops

Ferroelectric materials exhibit spontaneous polarization which can be reoriented between equivalent orientation states by an external electric field. Therefore, ferroelectric materials display P-E hysteresis loops under the applied electric field. This behavior is analogous to the magnetic induction (B) vs. magnetic field (H) loop of the ferromagnetic materials [12]. P-E hysteresis loop is simple and most effective tool for understanding the nature of the ferroelectric material. Ferroelectric materials display P-E hysteresis loop due to slow reversal or preferential orientation of individual electric dipoles and due to the domain wall motions. These materials possess spontaneous electric moment. The electric dipoles are aligned in the direction of applied electric field during switching. Fig.1.3 shows the electric dipoles are progressively aligned with applied electric field in positive bias region and these aligned electric dipoles are reversed when the electric field is changed to negative bias. The polarization of the ferroelectric material is increased with the applied electric field. However, the polarization of the ferroelectric material is saturated at particular electric field and this polarization is known as saturated polarization. After saturation at high end electric field the ferroelectric material behaves as linear dielectric material. The magnitude of saturated polarization (P_s) depends on the material composition, grain size, point defects and porosity [13, 14]. The point defects such as anion vacancies and cation vacancies affect the polarization as well as the nature of the hysteresis loop of the ferroelectric materials. In particular the oxygen vacancies in the oxide ceramic materials and some volatile cations are major contributors for the point defects formation in ferroelectric materials [15, 16].

Moreover, the polarization for the ferroelectric material also depends on the texture of the material [17]. These materials retain some of the polarization even after withdrawal of the applied electric field. The retained polarization is called as ‘remanent polarization’. The P_r is the basis for the NVRAM applications. Higher amount of P_r with very high endurance is deserved for the memory applications. The electric field required to nullify the polarization is known as ‘coercive field’ or ‘coercivity’ and it is denoted with ‘E_c’. Coercivity depends on the grain size, point defects and material composition. E_c is decreased as the grain size increases. Furthermore the defects increase the E_c by creating pinning centers during domain switching [13]. Ideally, for symmetrical P-E hysteresis loop $+P_r = -P_r$ and $+E_c = -E_c$. But in reality the nature and shape of the P-E hysteresis loop is affected by the charged defects, mechanical stresses, synthesis conditions and thermal process of the ferroelectric material [7].

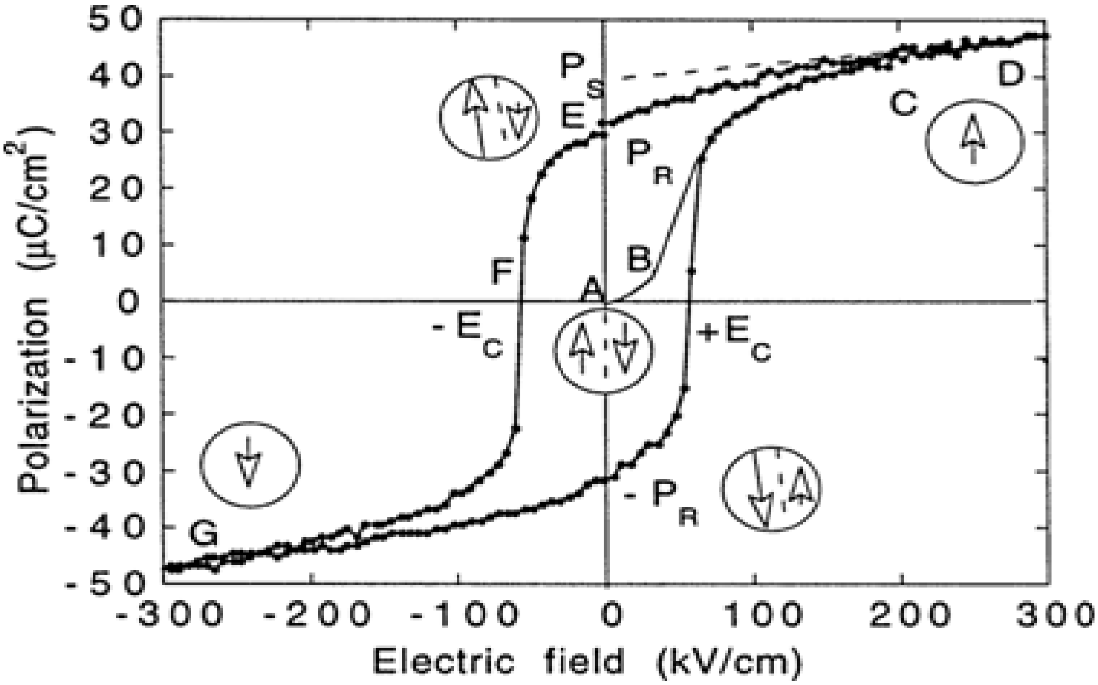

Fig. 1.3 Typical P-E hysteresis loop shows polarization reversal with applied electric field (After D. Damjanovic [7]).

Dielectric materials were classified in to four categories based on the variation of the dielectric displacement (D) with the applied electric field (E). Those are linear dielectric, ferroelectric, relaxor-ferroelectric and anti-ferroelectric materials. The term dielectric displacement is replaced with polarization (P) for the materials which have high dielectric constant or relative permittivity ($\varepsilon_r > 1$) [18]. For linear dielectric materials D is varied linearly with the applied electric field. The induced dielectric displacement is proportional to the applied electric field [Fig. 1.4 (a)]. The dielectric constant for the linear dielectric material is low due to the absence of permanent electric dipoles. Polyethelene terepthalate, Nylon-6, etc. show the linear dielectric behavior. In contrast to linear dielectric materials, the polarization response with the electric field is non-linear for ferroelectric, relaxor ferroelectric and antiferroelectric materials. Ferroelectric materials exhibit broad hysteresis loops with very high P_s as well as high P_r due to the contribution from the orientation polarization. Ferroelectric materials can be used for memory applications because of high P_r [Fig. 1.4 (b)]. Relaxor-ferroelectric materials display both double and single hysteresis loops based on relaxor-ferroelectric to ferroelectric transition with applied electric field [19]. In contrast to ferroelectric materials, relaxor-ferroelectric materials exhibit slim hysteresis loops with low P_r [Fig. 1.4 (c)]. Relaxor behavior is occurred due to the presence of microdomains or polar nanoregions instead of macroscopic domains. These microdomains quickly respond with the electric field than the macroscopic domains and this results slim hysteresis for relaxor-ferroelectric materials [11]. Anti-ferroelectricity is exhibited by the ordered crystal where two sub-lattices can be polarized in opposite direction. This arrangement causes zero net polarization in the absence of electric field. But in presence of the enough electric field macroscopic polarization is produced however, stronger field induces the ferroelectric phase in anti-ferroelectric materials. Anti-ferroelectrics materials show double hysteresis loop with very low P_r [Fig. 1.4 (d)]. High energy storage density is obtained for the anti-ferroelectric materials due to low P_r and double hysteresis loop [20].

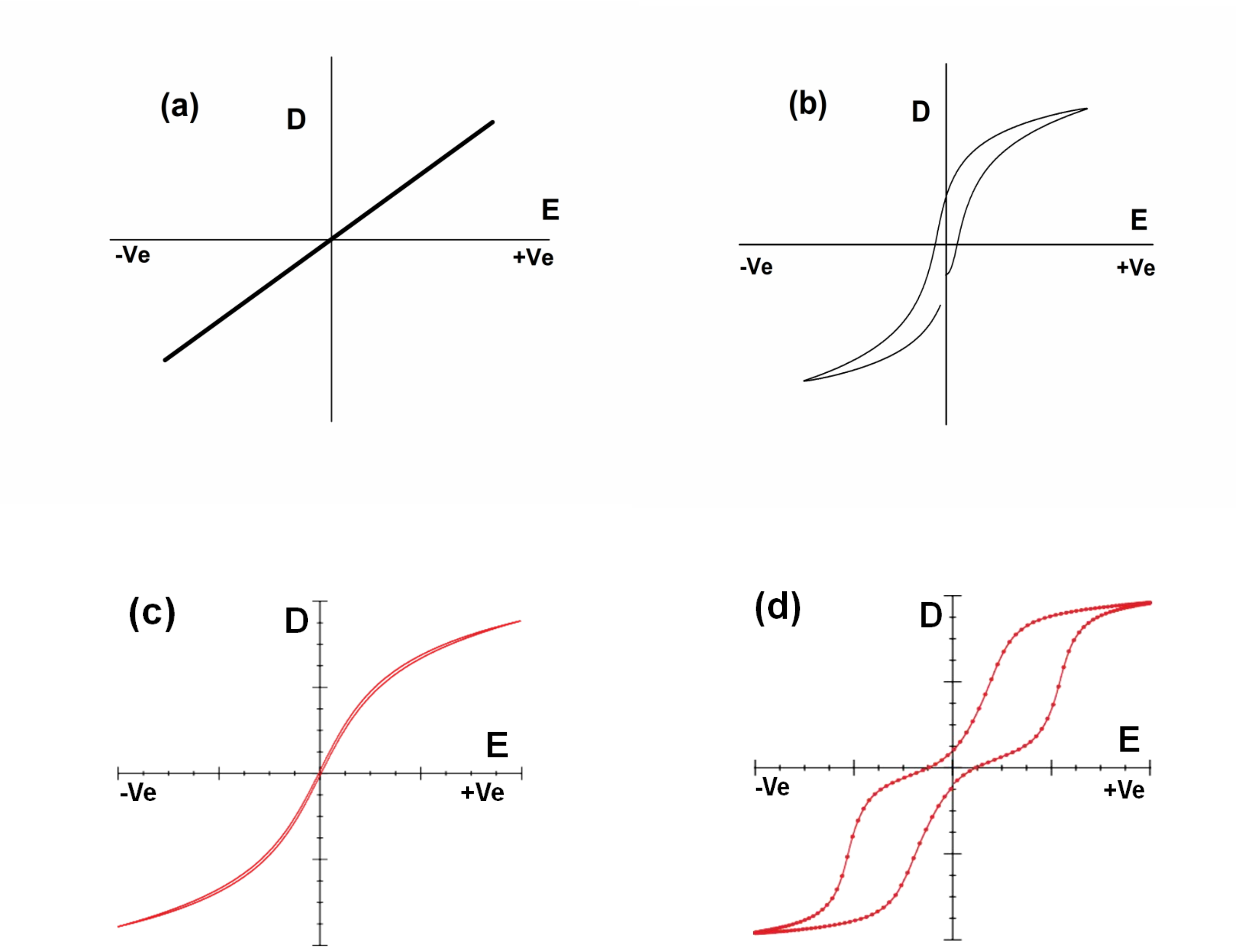

Fig. 1.4 Dielectric displacement (D) vs. electric field (E) for (a) linear dielectric, (b) ferroelectric, (c) relaxor-ferroelectric and (d) anti-ferroelectric materials (After L. Jin et al. [11]).

1.6.2 Strain versus electric field hysteresis loops

Tracking of strain (S) versus electric field (E) loops is as important as P-E hysteresis loop measurements since the S-E loops reveal the piezoelectric response of the material. In the ideal cases the strain response with the electric field should be linear as shown in Fig. 1.5 (a). However, this is possible when the material reaches to a truly single domain state. In reality, S-E loop is complicated because of the effects of converse piezoelectric effect from the lattice, switching and movements of domain-walls [7]. Ferroelectric ceramics usually consist of non-180^o domains. In addition to pure piezoelectric response of the material, the switching and movements of the non-180^o domain-walls make noticeable change in the dimensions of the material. Therefore, the total strain of the material is contributed by the linear converse piezoelectric effect and also by the domain-walls [21]. Domain-wall contribution to the strain leads to non linear S-E loop i.e. hysteresis loop for the normal ferroelectric materials (Fig. 1.5 (b)). In general both unipolar and bipolar S-E loops are recorded for the analysis of the piezoelectric properties. The bipolar strain loops of ferroelectric materials are found to display both positive and negative strain. Apart from the P-E and S-E loops, ferroelectric materials also show another kind of hysteresis loop that is piezoelectric coefficient (d_{33}) vs. DC bias field (E_{DC}) loops, especially for thin films [11].

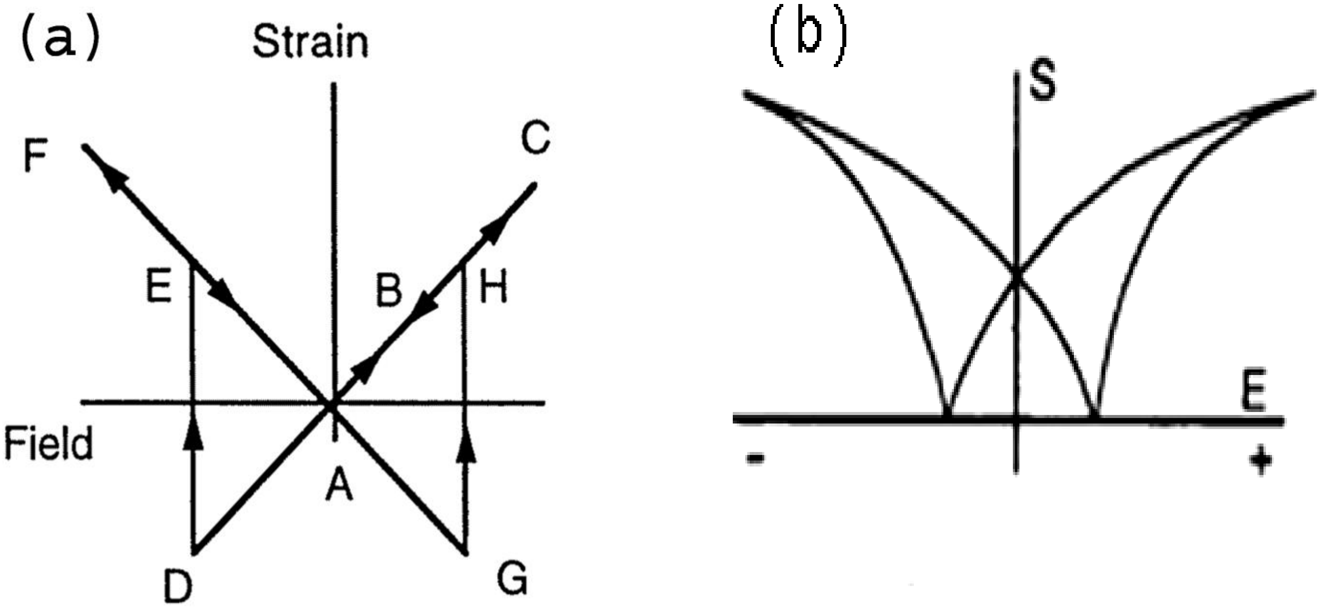

Fig.1.5 (a) Ideal S-E loop and (b) S-E hysteresis loop for ferroelectric material in reality (After D. Damjanovic [7] and G. H. Haertling [2]).

1.7 Energy storage density (ESD) and energy storage efficiency (ESF)

Dielectric materials can be utilized for high energy density capacitors, pulsed-power systems, and as inverters of hybrid electric vehicles. However, high ESD and ESF are required for this purpose. The ESD (U_e) for a linear dielectric capacitor is calculated from the dielectric constant (ε_r) using the equation (1.6).

$$U_e = \frac{1}{2}\varepsilon_r\varepsilon_0 E^2 \qquad (1.6)$$

Where, ε_0 is vacuum permittivity and E is the electric field [22]. The energy density of the linear dielectric material has square relationship with the electric field; hence high breakdown field is required to obtain high ESD. Moreover, the dielectric constant must be large to achieve high

ESD. However, linear dielectric materials exhibit low dielectric constants than that of the non-linear dielectric materials. Therefore, the linear dielectrics display low ESD. The ESD (W) of a non-linear dielectric material (ferroelectric or anti-ferroelectric material) is calculated from the P-E hysteresis loop using the equation (1.7).

$$W = \int_{P_r}^{P_{max}} E dP \qquad 0 \leq \mathrm{E} \leq \mathrm{E}_{\mathrm{max}} \tag{1.7}$$

In which P_{max} and P_r are the maximum and remanent polarizations, P is the polarization caused by the applied electric field (E). ESD could be calculated from either positive or negative bias region. Based on the above equation the non-linear dielectric materials must exhibit high polarization and large dielectric breakdown strength in order to obtain high energy density. In addition to these, the P_{max}-P_r value should be large. The ESF is the ratio of ESD to sum of ESD and energy loss [23]. The ESF (η) is expressed with the equation (1.8).

$$\eta = \frac{W}{W+W_{loss}} \tag{1.8}$$

Where, W is the ESD and W_{loss} is the energy loss. Energy loss is calculated from the area inside the P-E hysteresis loop [Fig. 1.6]. For real applications ESF is also considerable factor and it should be as high as possible. High energy efficiency limits the waste heat which improves the reliability and life time of the capacitor. Non-linear dielectric materials exhibit very high energy densities due to the high dielectric constant, although these often show strong hysteretic polarization response. Non-linear dielectric thin films display very high energy densities than that of the bulk materials since the breakdown field of the films is substantially high. Bulk non-linear dielectric materials show low breakdown field because of the massive structural defects such as pores, and intergranular secondary phases [24]. Among the non-linear dielectrics antiferroelectric materials exhibit very high energy densities because of their characteristic double P-E hysteresis loops. However, the performance of antiferroelectric materials dependent on the phase transition from antiferroelectric to ferroelectric caused by changes in the composition, electric field and temperature [25]. Therefore, ferroelectric materials are the good choice for achieving high energy densities. Ferroelectric materials show high dielectric constant and high polarization. However, these materials display broad hysteresis loops with high P_r which increases the energy loss. The P_r has to be minimized in order to obtain high ESD from the ferroelectric materials. This can be achieved by inducing the relaxor behavior in ferroelectric materials [26].

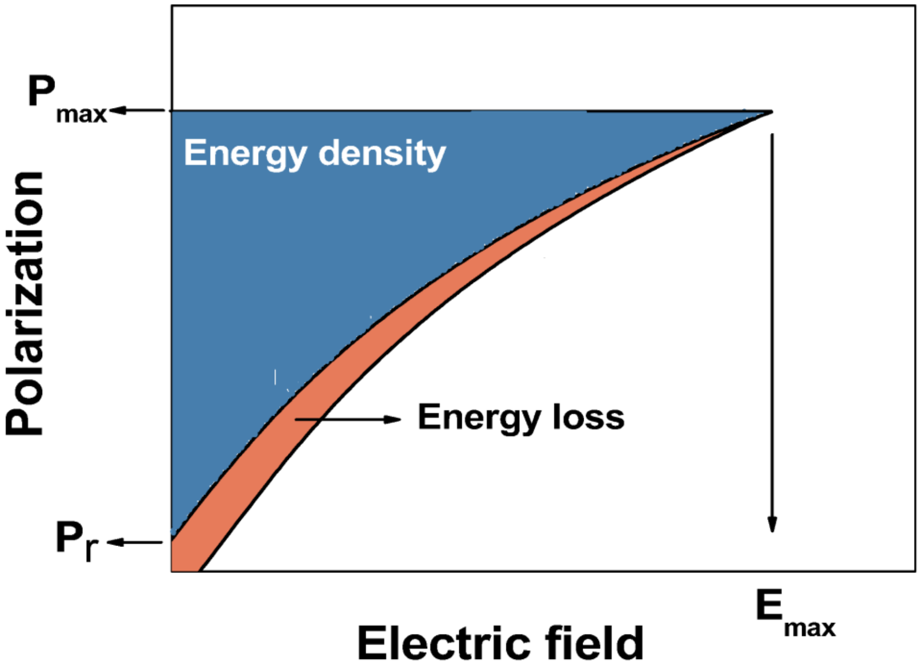

Fig. 1.6 Schematic diagram for energy storage.

1.8 Ferroelectric thin films

Ferroelectric thin and thick films have been widely used for various applications due to the advantages such as smaller size, low weight, good processing compatibility with silicon technology and easier integration to IC technology. In addition to these, thin films also offer benefits like lower operating voltage, higher speed and the ability to fabricate unique micro level structures. Moreover, the annealing temperatures for thin films are significantly lower as compared to the sintering temperatures of the bulk ceramics [2]. Ferroelectric thin films can be used as tunable microwave devices, microsensors in MEMS, NVRAM, DRAM, high energy density capacitors, and high frequency electrical components. Apart from this, ferroelectric thick films (2-20 µm) are used for piezoelectric and electrooptic devices. The reason for the utilization of thick film for these is to obtain maximum piezoelectric strain and electrooptic output. Ferroelectric films are used in NVRAM because of the interesting features like write and read cycle times are in sub-100 ns, non-volatility and low power consumption. However, for the utilization of the ferroelectric thin film in NVRAM application, high endurance of 10^{14} cycles is essential, especially for large scale applications.

Dielectric and piezoelectric responses of the ferroelectric films are different from that of the bulk ceramics. It is known that the thin films show high dielectric loss as compared with the bulk ceramics. The variation in dielectric constant for the films as compared to bulk is due to the mechanical stress and clamping effect of the film by the substrate which influence both the lattice and domain contributions to the permittivity. The high dielectric loss of the films is caused by the charge-defects, local polar-regions and the field–induced quasi-Debye contribution. Piezoelectric response of the thin films is significantly lower than that of its bulk counterpart due to the clamping effect. Moreover, in films the extrinsic piezoelectric response caused by the domain-wall motions is affected by the defects and substrate [5].

1.9 Polarization fatigue

Ferroelectric materials have been extensively investigated for the non-volatile memory applications because of the availability of high P_r. However, these materials loose the switchable polarization systematically under the repetitive bipolar switching cycles [27, 28]. This phenomenon is known as ‘polarization fatigue’. The polarization switching process can be presented by the P-E hysteresis loop and is described by the amplitude of cycling, E_c, P_r, switchable polarization (P_{sw}) and non-switchable polarization. Polarization switching creates or redistributes the defects in the capacitor. These defects degrade the P_{sw}. Apart from this, the electrodes of the capacitor injects electrons or positive charge carriers in to the ferroelectric material. These injected charges cause the non-switching at electrode-material interface, domain-wall pinning and local imprint mechanism. Hence, the defects formation or redistribution as well as injected charges from the electrodes result into the fatigue process [29]. The degradation of P_{sw} with cycling hampered the full commercialization of ferroelectric materials for memory applications. Moreover, the reliability of the energy storage performance of ferroelectric or anti-ferroelectric materials is also dependent on the endurance or fatigue resistance since the ESD is calculated from the P-E loops. Therefore, the ferroelectric materials with high endurance are deserved for the energy storage and memory applications. Polarization fatigue occurrence is illustrated by plotting P_r, P_{sw} or charge density (Q_{sw}) versus number of switching cycles (N). The measured P-E loop on fatigued ferroelectric capacitor is with reduced polarization, increased E_c and with tilted shape as compared with the P-E loop of the virgin ferroelectric capacitor [Fig.1.7].

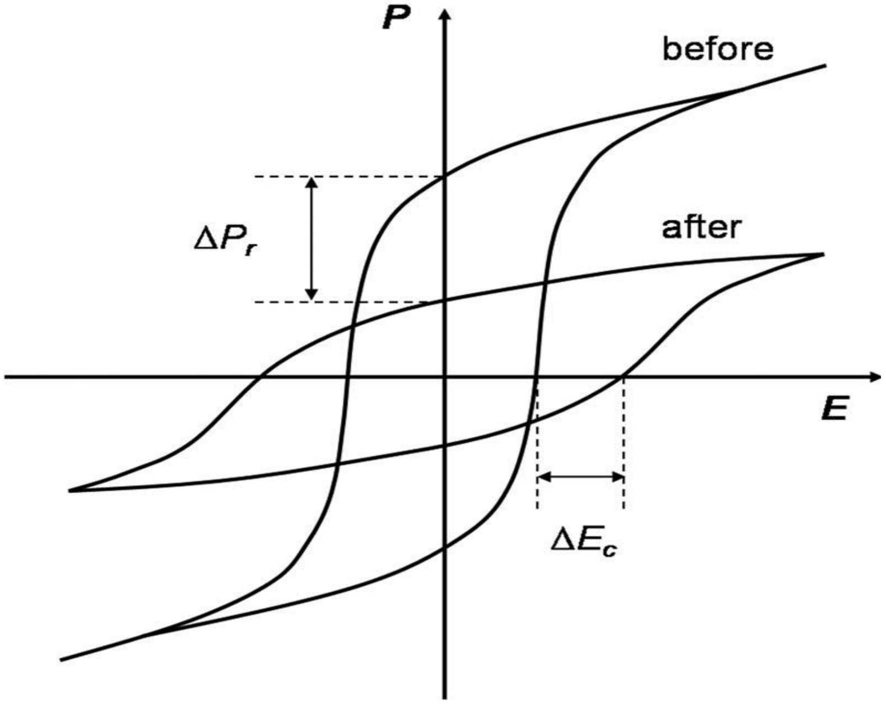

Fig. 1.7 P-E hysteresis loops recorded before and after fatigue test showing the variation in polarization and coercive field (After X. J. Lou [28]).

1.10 Lead free ferroelectric materials

So far PZT ($PbZr_xTi_{1-x}O_3$) based ferroelectric bulk materials have been widely used for electronic applications because of its very high polarization and piezoelectric properties (d_{33} = 225-590 pC/N) near the 'Morphotropic phase boundary (MPB)' separating tetragonal and rhombohedral phases [30]. At MPB, transition takes place between the two ferroelectric phases. Ferroelectric materials with composition-induced phase transition between two ferroelectric phases exhibits large polarization and strain at MPB due to the easier rotation of polarization direction by the external stress or electric field [1]. The outstanding ferroelectric and piezoelectric properties of PZT system motivated the researchers to investigate the possible lead based ferroelectric compositions such as $Pb(Mg_{1/3}Nb_{1/3})O_3$-$PbTiO_3$ (PMN-PT), $Pb(Zn_{1/3}Nb_{2/3})O_3$-$PbTiO_3$ (PZN-PT), $Pb(Ni_{1/3}Nb_{1/3})O_3$-$Pb(Zr,Ti)O_3$ (PNN-PZT) and $Pb_2Nb_2O_6$ [31-34]. However, the European community started restrictions on the use of hazardous elements in the electronic components. Since then the usage of lead based ferroelectrics are being restricted globally due to its toxic lead element. Continuous exposure to lead causes severe damage to nerves, brain and kidneys [35]. This triggers the researchers in worldwide to discover alternative materials. In this context several lead free compositions were investigated. Among all lead free compositions bismuth layer structured ferroelectric materials (BLSF), Alkali niobates and $BaTiO_3$ based material systems were extensively studied because of their high ferroelectric and piezoelectric properties [36].

Bismuth layer structured ferroelectric materials usually exist with $Bi_2A_{x-1}B_xO_{3x+3}$ compositions. BLSF structure comprised with pseudo perovskite layers stacked between $(Bi_2O_2)^{2+}$ sheets [37]. $Bi_4Ti_3O_{12}$ (BIT) is well known typical bismuth layer structured ferroelectric with high Curie point (> 600 ^{o}C), therefore it can be considered for high temperature piezoelectric applications. However, BIT shows low resistivity and high coercive filed which makes difficult to obtain sufficient piezoelectric properties. Later, the researchers made attempts to improve the resistivity of BIT by doping with the donor ions (Eg: Nb^{5+}, Ta^{5+}, Sb^{5+}, V^{5+}) [38]. The BIT compositions doped with Nb^{5+} and V^{5+} showed improved resistivity and T_C [39, 40]. Thereafter, many efforts were made to improve the piezoelectric properties of Bi-based ferroelectric compositions which resulted in synthesis of the new compositions such as $(Bi_{0.5}Na_{0.5})TiO_3$, $(Bi_{0.5}K_{0.5})TiO_3$, $(Na_{1/2}Bi_{1/2})_{1-x}Ca_xBi_4Ti_4O_{15}$, $SrBi_2Ta_2O_9$ and $(Bi_{0.5}Na_{0.5})_{0.94}Ba_{0.06}TiO_3$ [41-45]. Yttrium oxide doped $(Bi_{0.5}Na_{0.5})_{0.94}Ba_{0.06}TiO_3$ ferroelectric ceramics were reported with piezoelectric coefficient (d_{33}) of 137 pC/N and electromechanical coupling factor (k_p) of 30% [46]. Y.R Zhang et al. [47] reported the $(Na_{0.28}K_{0.22})_{0.5}Bi_{0.5}TiO_3$ ceramics with d_{33} of 192 pC/N, P_r of 19.5 µC/cm^2 and k_p of 32%. Another research group demonstrated high strain (S_{max}/E_{max} = 617 pm/V) and d_{33} of 190 pC/N for the $SrZrO_3$ modified $Bi_{1/2}(Na_{0.80}K_{0.20})_{1/2}TiO_3$ ceramics [48]. R. A. Malik [49] reported the solid-state route processed $0.96(Bi_{1/2}(Na_{0.84}K_{0.16})_{1/2}(Ti_{0.9825}Nb_{0.0175})O_3)$-$0.04SrTiO_3$ ceramics with ε_r of 1500 and with high strain (S_{max}/E_{max} = 876 pm/V). However, it is difficult to achieve highly dense ceramics for these compositions since the bismuth evaporation is investable at higher temperatures.

Alkali niobates are other interesting piezoelectric materials and these are indicated with chemical formula of ABO_3. In 1950s and 1960s some of the new compositions from alkali niobate family were investigated. Among these, solid solution of $0.5NaNbO_3$-$0.5KNbO_3$ (KNN) is widely studied due to its high piezoelectric properties as compared with other alkali niobates. KNN has several thermal induced phase transitions and MPBs. It exhibits ferroelectric-paraelectric phase transition at 400 ^oC temperature [50]. For the un-doped KNN ceramics, d_{33} of 70 pC/N and k_p of 25% were reported [51]. However, the piezoelectric properties of KNN are much lower as compared to the PZT based ceramics. Therefore, several attempts were made in order to improve the piezoelectric properties of KNN ceramics. In this context, $(K_{0.44}Na_{0.52}Li_{0.04})(Ta_{0.1}Sb_{0.06}Nb_{0.84})O_3$ ceramics with CuO dopant was reported with d_{33} of 260 pC/N and with P_r of 13.5 µC/cm^2 [52]. S. Zhang et al. [53] reported d_{33} of 265 pC/N, P_r of 25 µC/cm^2 and T_C of 368 ^oC for the solid state route synthesized $0.948(K_{0.5}Na_{0.5})NbO_3$-$0.052LiSbO_3$ ceramics. Saito et al. [54] demonstrated the textured $(K_{0.44}Na_{0.52}Li_{0.04})(Nb_{0.84}Ta_{0.10}Sb_{0.06})O_3$ ceramics with high d_{33} of 416 pC/N, k_p of 61% and T_C of 253 ^oC. The invention of these textured ceramics with high d_{33} prompted the efforts to improve the piezoelectric properties of alkali niobates. Thereafter, a research group revealed d_{33} of 424 pC/N, k_p of 52.1% and high strain (S_{max}/E_{max} = 768 pm/V) for the sol-gel synthesized $(Na_{0.52}K_{0.4425}Li_{0.0375})(Nb_{0.86}Ta_{0.06}Sb_{0.08})O_3$ ceramics [55]. However, KNN commercialization is hampered by the drawbacks such as low sinterability due to the volatility of alkali metal ions, and hygroscopic nature of the precursor reactants which causes non-stoichiometry [56, 57].

$BaTiO_3$ is a basic and popular ferroelectric ceramic with perovskite crystalline structure. It is one of the most exploited materials for capacitor and piezoelectric applications. $BaTiO_3$ undergoes several phase transitions from low temperature to high temperature, including rhombohedral to orthorhombic, orthorhombic to tetragonal and tetragonal to cubic. Phase transition from tetragonal to cubic takes place at 120 ^oC, and cubic perovskite is converted to hexagonal form at 1460 ^oC temperature [58, 6]. However, $BaTiO_3$ ceramics exhibit low piezoelectric coefficient (d_{33} = 190 pC/N) than that of the PZT based ceramics [59]. Researchers made enormous efforts to improve the piezoelectric properties of the $BaTiO_3$ ceramics through the different synthesis routes as well as by adding dopants. Researchers reported that calcium doped $BaTiO_3$ ceramics with higher dielectric constant [60]. T. Mitsui et al. [61] demonstrated the BCT ($Ba_{1-x}Ca_xTiO_3$) ceramics with improved T_C of 136 ^oC for x = 0.08. Moreover, $BaTiO_3$ takes hexagonally closed-packed-stacking structure at high temperature due to the larger ionic radius of Ba^{2+}, hence the barium substitution with calcium (smaller ionic radius) improves the stability of perovskite phase. D. Fu et al. [62] reported the biphasic polycrystalline BCT ($B_{0.65}Ca_{0.35}TiO_3$) ceramics with d_{33} of 250 pC/N. It was demonstrated that zirconium addition to $BaTiO_3$ results the substitution of titanium and forms $BaZr_xTi_{1-x}O_3$. Zr^{4+} ion (ionic radius = 0.72 A^o) addition to $BaTiO_3$ reduces the dielectric loss due to its bigger size and higher stability as compared to the Ti^{4+} ion (ionic radius = 0.60 A^o) [63, 64].

Table 1.1 Electrical properties of lead based and lead free ferroelectric materials

Composition	**d_{33} (pC/N)**	**Converse d_{33} (pm/V)**	**ε_r (RT)**	**T_C (°C)**	**Ref.**
PZT8	225	250	1000	300	[30]
PZT5A	375	600	1700	365	do
PZT5H	590	800	3400	190	do
$((Bi_{0.5}Na_{0.5})_{0.94}Ba_{0.06}TiO_3)+0.5Y_2O_3$	137	--	--	320	[46]
$((Na_{0.28}K_{0.22})_{0.5}Bi_{0.5}TiO_3)$	192	--	1007	--	[47]
BNKTN-$SrTiO_3$	--	876	1500	275	[49]
KNN-$0.052LiSbO_3$	265	--	1380	368	[53]
KNN-LTS	424	768	1902	265	[55]
BCZT	~620	1140	3060	93	[65]

Recently a new lead-free ferroelectric $Ba_{0.85}Ca_{0.15}Ti_{0.9}Zr_{0.1}O_3$ ((1-x) $Ba(Zr_{0.2}Ti_{0.8})O_3$-x$(Ba_{0.7}Ca_{0.3})TiO_3$ where x=0.5) system with outstanding piezoelectric properties was investigated. Conventional solid-state route synthesized $Ba_{0.85}Ca_{0.15}Ti_{0.9}Zr_{0.1}O_3$ (Here afterwards abbreviated as BCZT) ceramics showed large d_{33} of ~620 pC/N, lower E_c of 1.68 kV/cm, high dielectric constant of 3060 and converse d_{33} of 1140 pm/V. Phase diagram of this system exhibits a MPB starting from a tricritical triple point of a cubic (C), rhombohedral (R) and tetragonal phases (T). The surprising high piezoelectric properties originate from the composition proximity of the MPB to the tricritical triple point, which eliminates the polarization anisotropy [65]. The existence of C-R-T triple point in the BCZT system is akin to the high-piezoelectric lead based systems [66]. The piezoelectricity (d_{33} = 620 pC/N) of this composition is much higher than that of the other lead-free systems and it is comparable to ultrasoft PZT5H (d_{33} = 590 pC/N). Apart from this, the converse d_{33} of this system is much higher than that of the PZT based ceramics (~250-800 pm/V) [30]. Furthermore, unlike bismuth based and alkali niobate based ferroelectric materials there is no volatile element in the BCZT composition therefore, BCZT system can maintain predefined stoichiometry even after high temperature sintering. The large piezoelectric response of BCZT system makes it as promising candidate for lead free piezoelectric applications.

The outstanding piezoelectric properties of BCZT system had caught the attention of researchers worldwide towards this composition. In this context many research groups put efforts on BCZT ceramics to improve the electrical properties as well as T_C. S. Su et al. [67] demonstrated d_{33} of 630 pC/N, k_p of 56% and T_C of 80 ^oC for the solid-state route synthesized BCZT ceramics through the optimization of poling. It was reported that P_r of 10.7 µC/cm^2, converse d_{33} of 1310 pC/N and T_C of 75 ^oC for the solid-state route processed

$0.55Ba(Zr_{0.2}Ti_{0.8})O_3$-$0.45(Ba_{0.7}Ca_{0.3})TiO_3$ ceramics [68]. H. Bao et al. [69] demonstrated higher T_C of 114 °C for the modified BCZT system with $0.47Ba(Zr_{0.15}Ti_{0.85})O_3$-$0.53(Ba_{0.8}Ca_{0.2})TiO_3$ composition, however, this modified system showed lower dielectric and piezoelectric electric properties since the composition is deviated from the tricritical triple point. Therefore, it is essential to improve the T_C of the BCZT system without any modification in the MPB composition for high temperature piezoelectric devices. Moreover, the energy storage properties investigation on the BCZT system is scarce, which is essential to consider the same for pulse power applications.

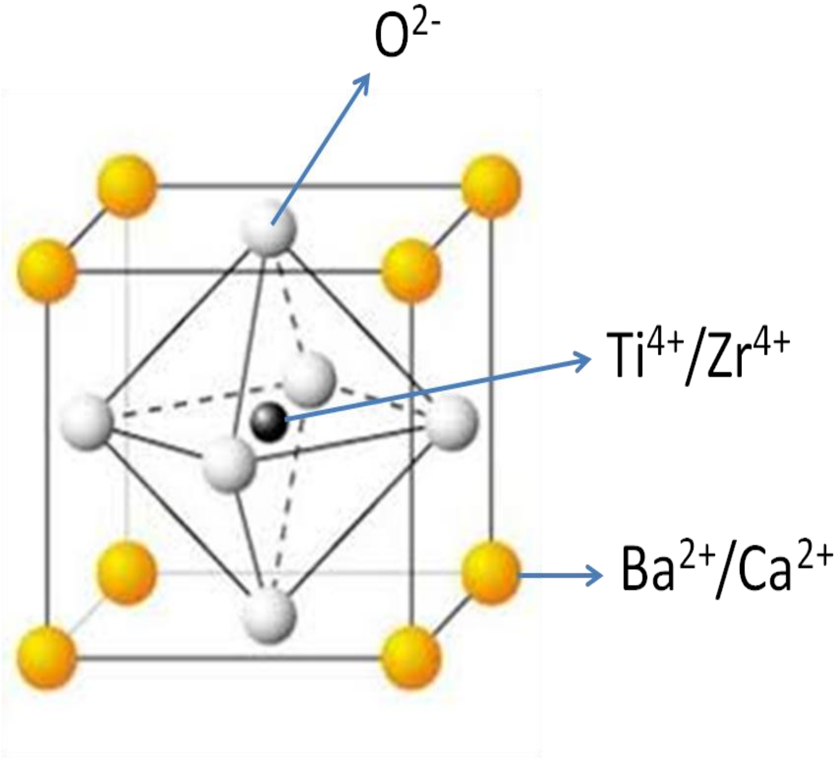

Fig. 1.8 Schematic illustration of the BCZT unit cell.

Apart from bulk ceramics, some researchers have been working on the BCZT thin films as well since the world is fascinated towards the development of portable and microelectronic devices. Z. M. Wang et al. [70] demonstrated P_r of 22.15 μC/cm^2 and E_c of 68.06 kV/cm for the sol-gel derived 800 nm thick BCZT films. Converse d_{33} of 80 pm/V and ε_r of 1010 were reported for the pulsed laser deposited 600 nm thick BCZT films [71]. W. L. Li et al. [72] revealed converse d_{33} of 258 pm/V for the magnetron sputtered 200 nm thick BCZT films. However, investigation of energy storage properties on BCZT films was not reported, which is essential since the ferroelectric thin films show substantially high energy storage performance than the bulk ceramics. Magnetron sputtering is a physical vapor deposition technique. It is well known that the physical vapor deposition methods have the disadvantages such as low deposition rates, difficulty in stoichiometry control, high crystallization temperatures and high capital investments. Therefore, it is necessary to develop the BCZT films with excellent ferroelectric, piezoelectric and energy storage properties to substitute the lead based ferroelectric films through the cost-effective route. It is known that the sol-gel deposition technique has the advantages like fine stoichiometry control, large surface covering with uniform thickness, economical and low temperature annealing [2]. Sol-gel technique is also widely used for the synthesis of ferroelectric bulk ceramics due to low processing temperatures, good homogeneity and it also reduces the time required for sintering as compared to the conventional solid-state reaction method.

1.11 Motivation and objectives of the research activity

Since the lead based ferroelectric materials are being restricted worldwide it is essential to explore the new lead-free ferroelectric BCZT composition in the form of bulk ceramics and thin films. At the same time the T_C of the BCZT system has to be improved, and BCZT thin film materials must be developed with enhanced electrical properties. Therefore, the main objective of this research activity is to develop the BCZT bulk ceramics with improved T_C and enhanced electrical properties. Moreover, it is essential to synthesize the BCZT films with excellent ferroelectric, piezoelectric, energy storage and mechanical properties through the cost-effective route. Therefore, the objectives of the research activities described in this thesis are like the following:

1) Synthesis of BCZT nano-powders following sol-gel technique, and study of the phase and morphology of the powder.
2) Processing of BCZT ceramics through the different sintering techniques at various temperatures, and analyses of the phase, microstructure, ferroelectric and piezoelectric properties.
3) Development of the BCZT thin films following sol-gel deposition technique in ambient air as well as in oxygen-rich atmosphere, and study of the crystal structure, microstructure, ferroelectric and piezoelectric properties.
4) Development of the thicker BCZT films in oxygen-rich atmosphere, and analyses of the phase, microstructure, electrical and mechanical properties.
5) Correlation of the electrical properties of the BCZT bulk ceramics and films with their microstructure.

1.12 References

1. K. Uchino, Ferroelectric devices, CRC press, New York, 2010.
2. G. H. Haertling, J. Am. Ceram. Soc., **82 [4]** (1999) 797-818.
3. M. H. Park, H. J. Kim, Y. J. Kim, T. Moon, K. D. Kim, C. S. Hwang, Adv. Energy Mater., **4** (2014) 1400610.

4. S. Trolier-McKinstry, P. Muralt, J. Electroceram., **12** (2004) 7–17.
5. N. Setter, D. Damjanovic, L. Eng, G. Fox, S. Gevorgian, S. Hong, A. Kingon, H. Kohlstedt, N. Y. Park, G. B. Stephenson, I. Stolitchnov, A. K. Taganstev, D. V. Taylor, T. Yamada, S. Streiffer, J. Appl. Phys., **100** (2006) 051606.
6. B. Jaffe, W. R. Cook Jr., H. Jaffe, Piezoelectric ceramics, Academic press, New York, 1971.
7. D. Damjanovic, Rep. Prog. Phys., **61** (1998) 1267.
8. R. S. Roth, J. Res. Nat. Bur. Std., **58** (1957) 75.
9. E. A. Wood, Acta cryst., **4** (1951) 353.
10. C. H. Ahn, K. M. Rabe, J. M. Triscone, Science., **303** (2004) 488.
11. L. Jin, F. Li, S. Zhang, J. Am. Ceram. Soc., **97[1]** (2014) 1-27.
12. B. Xu, L. E. Cross, J. J. Bernstein, Thin solid films., **377-378** (2000) 712-718.
13. Y. Tan, J. Zhang, Y. Wu, C. Wang, V. Koval, B. Shi, H. Ye, R. McKinnon, G. Viola, H. Yan, Sci. reports., **5** (2015) 9953.
14. E. W. Yap, J. Glaum, J. Oddershede, J. E. Daniels, Script. Mater., **145** (2018) 122-125.
15. C. H. Park, D. J. Chadi, Phys. Rev. B., **57** (1998) R13961(R).
16. S. B. Desu, D. P. Vijay, Mater. Sci. Eng. B., **32** (1995) 75-81.
17. J. L. Jones, S. C. Vogel, E. B. Slamovich, K. J. Bowman, Script. Mater., **51** (2004) 1123-27.
18. I. Burn, D. M. Smyth, J. Mater. Sci., **7** (1972) 339-343.
19. Prateek, V. K. Thakur, R. K. Guptha, Chem. Rev., **116** (2016) 4260-4317.
20. X. Hao, Z. Yue, J. Xu, S. An, C. W. Nan, J. Appl. Phys., **110** (2011) 064109.
21. M. E. Caspari, W. J. Merz, Phys. Rev., **80 [6]** (1950) 1082.

22. B. Chu, X. Zhou, B. Neese, Q. M. Zhang, F. Bauer, IEEE trans. Dielect. Electric. Insul., **13 [5]** (2006) 1162.
23. B. Peng, Q. Zhang, X. Li, T. Sun, H. Fan, S. Ke, M. Ye, Y. Wang, W. Lu, H. Niu, J. F. Scott, X. Zeng, H. Huang, Adv. Electron. Mater., (2015) 1500052.
24. D. K. Kwon, M. H. Lee, IEEE. Trans. Ultrason. Ferroelec. Freq. Con., **59 [9]** (2012) 1894.
25. B. Xu, Y. Ye, L. E. Cross, J. Appl. Phys., **87 [5]** (2000) 2507.
26. L. Zhu, Q. Wang, Macromolecules., **45** (2012) 2937-54.
27. E. M. Alkoy, K. Uchiyama, T. Shiosaki, S. Alkoy, J. Appl. Phys., **99** (2006) 106106.
28. X. J. Lou, J. Appl. Phys., **105** (2009) 024101.
29. A. K. Tagantsev, I. Stolichnov, E. L. Colla, N. Setter, J. Appl. Phys., **90[3]** (2001) 1387.
30. T. R. Shrout, S. J. Zhang, J. Electroceram., **19** (2007) 111-124.
31. S. Sun, X. Pan, P. Wang, L. Zhu, Q. Huang, D. Li, Z. Yin, Appl. Phys. Lett., **84[4]** (2004) 574.
32. J. Kuwata, K. Uchino, S. Nomura, Ferroelectrics., **37** (1981) 579-82.
33. G. Robert, M. Demartin, D. Damjanovic, J. Am. Ceram. Soc., **81[3]** (1998) 749-53.
34. M. Pastor, P. K. Bajpai, R. N. P. Choudhary, Bull. Mater. Sci., **28[3]** (2005) 199-203.
35. E. Ringgaard, T. Wurlitzer, J. Europ. Ceram. Soc., **25** (2005) 2701-06.
36. I. Coondoo. N. Panwar, A. Kholkin, J. Adv. Dielectric., **3[2]** (2013) 1330002.
37. R. E. Newnham, R. W. Wolfe, J. F. Dorrian, Mat. Res. Bull., **6** (1971) 1029-40.
38. M. Villegas, A. C. Caballero, C. Moure, P. Duran, J. F. Fernandez, J. Am. Ceram. Soc., **82 [9]** (1999) 2411-16.

39. H. S. Shulman, M. Testorf, D. Damjanovic, N. Setter, J. Am. Ceram. Soc., **79 [12]** (1996) 3124-28.
40. Y. Noguchi, M. Miyayama, Appl. Phys. Lett., **78 [13]** (2001) 1903-05.
41. X. Tian, Z. Wu, Y. Jia, J. Chen, R. K. Zheng, Y. Zhang, H. Luo, Appl. Phys. Lett., **102** (2013) 042907.
42. A. Sasaki, T. Chiba, Y. Mamiya, E. Otsuki, Jpn. J. Appl. Phys., **38** (1999) 5564-67.
43. T. Takenaka, K. Sakata, Ferroelectrics., **118** (1991) 123-133.
44. M. Miyayama, Y. Noguchi, J. Europ. Ceram. Soc., **25** (2005) 2477-82.
45. X. Wang, H. L. W. Chan, C. L. Choy, Solid state Comm., **125** (2003) 395-99.
46. C. Zhou, X. Liu, W. Li, C. Yuan, Mater. Res. Bull., **44** (2009) 724-27.
47. Y. R. Zhang, J. F. Li, B. P. Zhang, J. Am. Ceram. Soc., **91 [8]** (2008) 2716-19.
48. A. Hussain, J. U. Rahman, A. Zaman, R. A. Malik, J. S. Kim, T. K. Song, W. J. Kim, M. H. Kim, Mater. Chem. Phys., **143** (2014) 1282-88.
49. R. A. Malik, J. K. Kang, A. Hussain, C. W. Ahn, H. S. Han, J. S. Lee, Appl. Phys. Exp., **7** (2014) 061502.
50. M. Ahtee, A. M. Glazer, Acta Cryst., **A32** (1976) 434.
51. H. Birol, D. Damjanovic, N. Setter, J. Europ. Ceram. Soc., **26** (2006) 861-66.
52. N. M. Hagh, K. Kerman, B. Jadidian, A. Safari, J. Europ. Ceram. Soc., **29** (2009) 2325-32.
53. S. Zhang, R. Xia, T. R. Shrout, G. Zang, J. Wang, J. Appl. Phys., **100** (2006) 104108.
54. Y. Saito, H. Takao, T. Tani, T. Nonoyama, K. Takatori, T. Homma, T. Nagaya, M. Nakamura, Nature., **432** (2004) 84.

55. Y. Huan, X. Wang, Z. Shen, J. Kim, H. Zhou, L. Li, J. Am. Ceram. Soc., **97 [3]** (2014) 700-03.
56. M. D. Maeder, D. Damjanovic, N. Setter, J. Electroceram., **13** (2004) 385-92.
57. E. Hollenstein, M. Devis, D. Damjanovic, N. Setter, Appl. Phys. Lett., **87** (2005) 182905.
58. A. V. Hippel, Rev. Mod. Phys., **22 [3]** (1950) 221.
59. H. Takahashi, Y. Numamoto, J. Tani, S. Tsurekawa, Jpn. J. Appl. Phys., **45 [9B]** (2006) 7405-08.
60. Y. Sakabe, N. Wada, T. Hiramatsu, T. Tonogaki, Jpn. J. Appl. Phys., **41** (2002) 6922-25.
61. T. Mitsui, W. B. Westphal, Phys. Rev., **124 [5]** (1961) 1354.
62. D. Fu, M. Itoh, S. Koshihara, Appl. Phys. Lett., **93** (2008) 012904.
63. S. Mahajan, O. P. Thakur, C. Prakash, K. Sreenivas, Bull. Mater. Sci., **34 [7]** (2011) 1483-89.
64. J. Zhai, D. Hu, X. Yao, Z. Xu, H. Chen, J. Europ. Ceram. Soc., **26** (2006) 1917-20.
65. W. Liu, X. Ren, PRL., **103** (2009) 257602.
66. D. E. Cox, B. Noheda, G. Shirane, Y. Uesu, K. Fujishiro, Y. Yamada, Appl. Phys. Lett., **79 [3]** (2001) 400.
67. S. Su, R. Zuo, S. Lu, Z. Xu, X. Wang, L. Li, Cur. Appl. Phys., **11** (2011) S120-S123.
68. M. C. Ehmke, S. N. Ehrlich, J. E. Blendell, K. J. Bowman, J. Appl. Phys., **111** (2012) 124110.
69. H. Bao, C. Zhou, D. Xue, J. Gao, X. Ren, J. Phys. D: Appl. Phys., **43** (2010) 465401.
70. Z. M. Wang, K. Zhao, X. L. Guo, W. Sun, H. L. Jiang, X. Q. Han , X. T. Tao, Z. X. Cheng, H. Y. Zhao, H. Kimura, J. Mater. Chem. C., **1** (2013) 522-30.

71. A. Piorra, A. Petraru, H. Kohlstedt, M. Wuttig, E. Quandt, J. Appl. Phys., **109** (2011) 104101-5.

72. W. L. Li, T. D. Zhang,Y. F. Hou, Y. Zhao, D. Xu, W. P. Cao, W. D. Fei,. RSC Adv., **4** (2014) 56933-7.

Chapter 2

Experimental techniques

This chapter deals with the detailed description of the materials and reagents as well as the methodology used for the synthesis of BCZT powders, bulk ceramics and thin films. And it also presents the characterization techniques that were used for the analysis of phase, microstructure and electrical properties of the BCZT materials.

2.1 Materials and reagents

The materials and reagents used in this research activity are barium acetate (Sigma Aldrich, purity 99.5%), calcium carbonate (Sigma Aldrich, purity 99.95%), polyvinyl pyrrolidone (Sigma Aldrich), zirconium n-propoxide solution (Sigma Aldrich, 70 wt% in 1-propanol), titanium isopropoxide (Sigma Aldrich, purity 97%), acetic acid (Merck, purity 99.8%), 2-propanol (Merck, purity 99.7%), 2-methoxy ethanol (Alfa Aesar, purity 99%), acetyl acetone (Sigma Aldrich, purity 99%) and distilled water.

It is known that the properties of the ceramic materials are mostly dependent on the processing technique and the way it was synthesized. Therefore, it is necessary to monitor and control the steps for the synthesis and the processing equipment to obtain the best results. Preparation of ferroelectric ceramics includes powder synthesis and processing.

2.2 Powder synthesis methods

So far many synthesis techniques such as solid-state reaction method, co-precipitation, hydrothermal and sol-gel techniques were developed for the synthesis of ferroelectric ceramic powders.

2.2.1 Solid-state reaction method

It is widely used for the synthesis of ferroelectric ceramics due to the advantages such as simplicity and low cost of starting materials. The name solid-state reaction is given because of the starting solid raw materials. In this method the precursor powder for making the ceramics is synthesized by using individual oxides, carbonates or nitrates of the metal. Calculated amounts of metal oxides, metal carbonates or metal nitrates as per stoichiometry of the composition were mixed thoroughly using the ball mill. An organic solvent is used to make the slurry with the metal precursors for milling. The milled slurry is dried to evaporate the solvent. Then the dried powder is calcined to decompose the carbonates or nitrates, and to obtain the phase. The powders prepared from this method are with larger grains. However, the solid-state reaction method has the drawbacks such as high processing temperatures and lack of proper homogeneity [1]. Moreover, the high processing temperature causes to low sinterability where the metal ions evaporation is inevitable.

2.2.2 Hydrothermal method

In hydrothermal thermal synthesis of numerous simultaneous reactions takes place between the dissolved and solid species in aqueous solution to form anhydrous multi-component oxides. This method provides media for an effective reaction environment for the synthesis of numerous smart ceramics from the variety of precursor reagents (Water soluble salts, hydroxides and oxides). Phase-pure ceramics can be synthesized with hydrothermal method using inexpensive precursors at moderate temperatures and pressures. To take these advantages of hydrothermal method it is necessary to select the proper precursor system, and optimization of the processing variables like reagent concentrations and ratios, p^H, temperature and pressure [2]. In this method the reagents are converted in to precipitate, and taken in the hydrothermal vessel or autoclave. The autoclave with the precipitate is heated under high pressure to obtain the anhydrous oxide [3]. However, the hydrothermal synthesis has the disadvantages such as raw materials limited to soluble salts and long reaction time [4].

2.2.3 Sol-gel technique

Sol-gel technique has been extensively used for the fabrication of ceramics due to the advantages such as improved compositional homogeneity and lower densification temperatures. These advantages are aroused because of the careful control on composition by mixing the constituents at molecular or atomic level in the solution. Other advantage of the technique is that the suitable manipulation of the precursor sol which allows for the processing of the ceramics in more variety of forms. Powders, bulk monoliths, thin films, fibers, nano-materials, xerogels and aerogels can be fabricated following the sol-gel route. Out of all these advantages with sol-gel route, however, many parameters such as starting chemicals, solvent type, solution concentration, solution reactions and firing procedures can affect the phase assemblage and properties of the final product. Therefore, all these parameters need to be optimized in order to obtain the desired products with designed properties [5].

In sol-gel route the components are dissolved in solvents, and made into a solution. This is a multi-component ionic or molecular solution which is with the possibility for the atomic-scale mixing for ultra-homogenization. The precursor chemicals in sol-gel route either may be inorganic nitrates, inorganic chlorides or metal alkoxides, and the solvent is water or a short-chain alcohol. The stability of the precursor solution is the basis for the next steps of the process. Precursor solution is progressively converted in to gel due to hydrolysis and poly-condensation. Gelation of the sol is controlled by the p^H, ionic strength, temperature and time. Based on the degree of gelation the solution can be utilized to produce the different forms of products. Shaping of the viscous sol or gel is the key point for the synthesis of products such as spheres, fibers, thin sheets, films and small cubes. Heat treatment of the gel leads to the formation of xerogel. Calcination process varies and is dependent on the type of product being made. However, the time and temperature required in this method is substantially lower than that of the solid-state method due to high reactivity of the xerogel [6]. The calcined xerogel is crushed in to powder with mortar-pestle.

2.3 Steps involved in the processing of BCZT ceramics

2.3.1 Synthesis of BCZT nano-powder

BCZT ($Ba_{0.85}Ca_{0.15}Ti_{0.90}Zr_{0.10}O_3$) powder was synthesized by following the sol-gel technique. The raw materials for the synthesis of the BCZT powder are barium acetate, calcium carbonate, zirconium n-propoxide and titanium isopropoxide. Acetic acid, distilled water and 2-propanol are solvents, and acetyl acetone was used as chelating agent for the stabilization of zirconium and titanium ions. For the synthesis of the BCZT precursor sol, firstly Ba-Ca solution was prepared by dissolving the calculated amounts of barium acetate and calcium carbonate in acetic acid and distilled water. Similarly Ti-Zr solution was prepared by adding the calculated amounts of Ti and Zr precursors in the mixed solution of 2-propanol and acetyl acetone. Ba-Ca solution and Ti-Zr solutions were mixed and processed using hot plate with simultaneous heating and stirring at 70-80 ^{o}C temperature for 40 minutes to obtain homogeneous BCZT precursor sol (Fig. 2.2). The BCZT precursor sol was evolved in to gel after 2-3 days of ageing due to the hydrolysis and poly-condensation reactions.

Fig. 2.1 Image of synthesized BCZT gel.

The obtained BCZT gel was dried in oven, and decomposed in conventional box-type furnace at 400 ^{o}C temperature in air for 30 min. Finally the decomposed BCZT gel was calcined at 900 ^{o}C temperature for 1 hour in air.

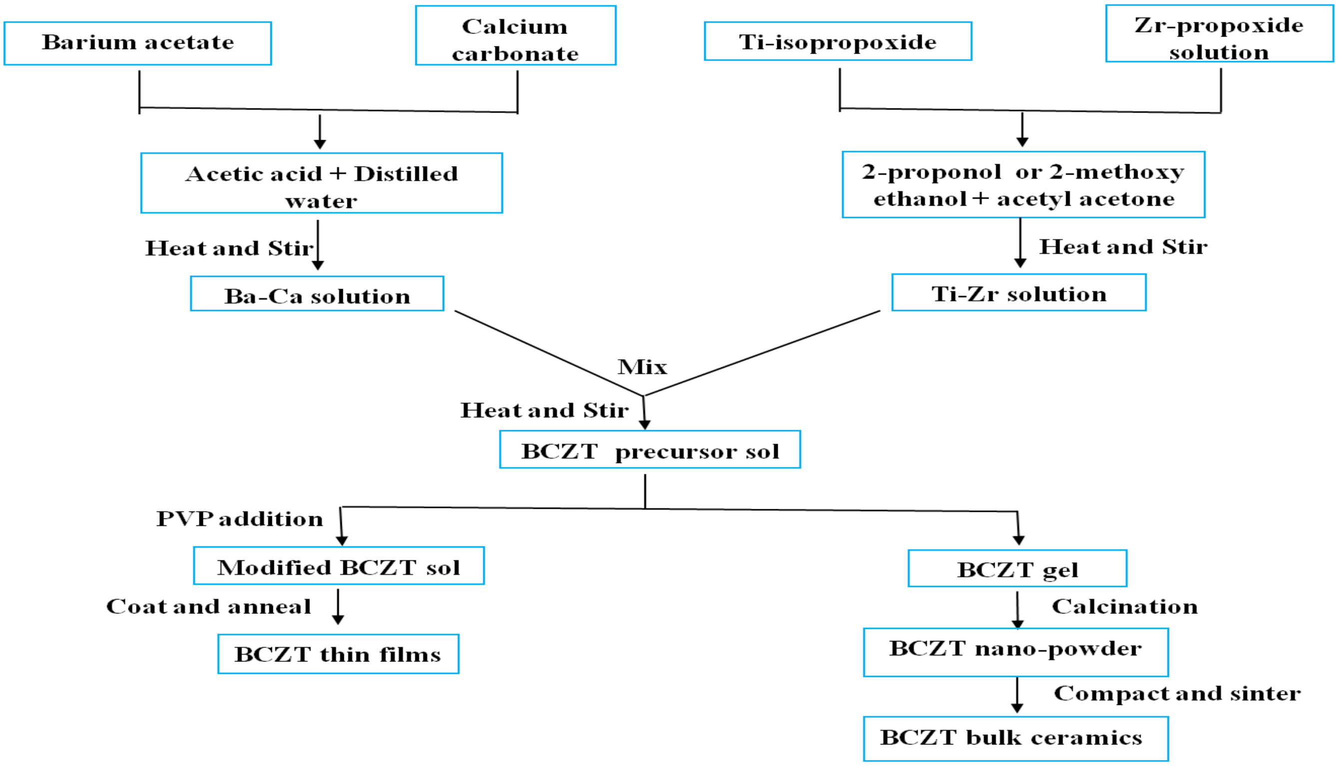

Fig. 2.2 Flow sheet for the processing of BCZT bulk ceramics and thin films.

2.3.2 BCZT nano-powder compaction by cold isostatic pressing (CIP)

CIP is a common method for the processing of various types of green ceramic bodies. CIP produces high dense compacted green bodies because of the high all-round pressure during the pressing of the powder. In this method the powder compaction success depends on the size and shape of the rubber mold in which the compaction is carried out [7]. The BCZT nano-powder was compacted by CIP. The synthesized nano-powder was ground by mortar-pestle to obtain fine powder. The BCZT powder was properly filled in the cylindrical shape rubber mold (Size of 1 cm diameter and 9 cm length), and it was sealed with stopper before pressing. For the compaction of BCZT nano-powder a pressure of 250 MPa was applied to obtain dense green body. The compacted BCZT green bodies were sintered for the densification and grain growth.

2.3.3 Sintering

Sintering is a method of consolidation of powder compacts by heating at temperatures near to their melting points. It is used widely for the fabrication of bulk ceramics, and in powder metallurgy. In sintering inter-particle pores in a granular material are eliminated by the atomic diffusion driven by the capillary forces. The density of the sintered compact is improved remarkably due to the decreased porosity and particle fusion [8, 9]. Sintering also helps in the improvement of average grain size distribution, elastic modulus, thermal conductivity and crystal structure [10, 11]. However, the density, mechanical and electrical properties of the ceramic depends on the way it was sintered. BCZT green bodies were sintered using the conventional furnace as well as the furnace with microwave heating facility.

2.3.4 Dimensioning and electroding

As sintered BCZT cylinder is irregular in shape. Since the electrical properties are dependent on the geometry of the specimen it is necessary to cut and finish the ceramic in perfect shape. The sintered cylinder was ground using conventional grinding machine with diamond as an abrasive medium. Then the grinded BCZT cylinders were sliced in to 1 mm thick discs using the isomet low speed precision cutter (Make: Buehler]. Finally BCZT discs were polished with the SiC abrasive paper to make smooth surfaces.

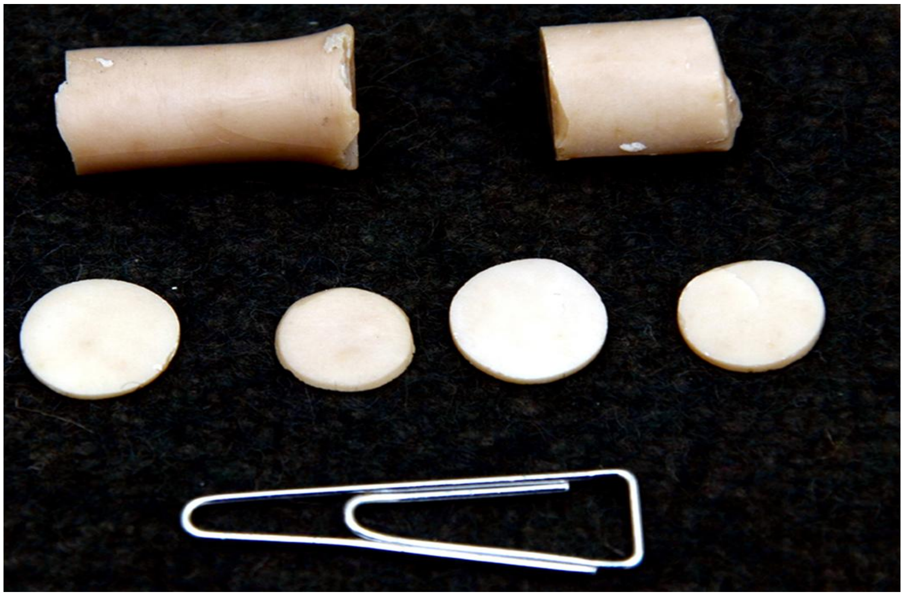

Fig. 2.3 Image of BCZT bulk ceramics.

Electroding is a process of applying of conductive layer to the surfaces of the ferroelectric material. Generally electroding is done by conventional evaporation or by sputtering of the electrode materials. Electroding for a ferroelectric material is necessary to make the electrical contacts for electrical property measurements and for poling. The electrode materials are usually metals such as gold, platinum, silver and alluminium. Electroding for BCZT ceramic discs were carried out by applying silver paste. Silver paste coated BCZT discs were heated to evaporate the solvents. Then the electrodes were tested to ensure the contacts are ohmic.

2.3.5 Poling

Electroded BCZT discs were poled to orient the domains in the individual grains of the ceramic in the direction of the applied electric field. Piezoelectric response of the individual crystal is cancelled due to the random distribution of domains in the ferroelectric ceramic. Therefore, ferroelectric ceramics must be poled by applying strong electric field usually at elevated temperatures in order to align the dipoles. Poling makes the ferroelectric ceramic electromechanically active. The extent of domain alignment is dependent on the applied electric field and the temperature. Magnitude of electric field required for poling the ceramic is determined through the coercive field. However, the alignment is never complete, and the extent of alignment depends on the crystal structure of the ceramic [1].

2.4 Thin film deposition techniques

So far various techniques for the deposition of films were emerged due to the utilization of ferroelectric thin films in MEMs. Earlier thin film depositions were carried out by the physical techniques such as ion-beam sputtering, rf planar magnetron sputtering or dc magnetron sputtering. Progressively metal-organic chemical vapor deposition (MOCVD) and chemical solution deposition techniques (CSD) which include sol-gel and metallo-organic decomposition methods were developed. Later the pulsed laser deposition technique (PLD) was also investigated for the fabrication of the ferroelectric thin films [12]. Thin film deposition techniques are broadly classified in to physical vapor deposition methods (vacuum methods) and chemical methods (non-vacuum methods). Physical vapor deposition (PVD) includes different types of sputtering techniques and PLD whereas the chemical methods include MOCVD and CSD techniques.

Ferroelectric thin films are deposited either on Pt coated or on ceramic electrode ($LaNiO_3$, $La_{0.5}Sr_{0.5}CoO_3$ or $SrRuO_3$ …etc) coated silicon substrates [13, 14]. Besides the silicon substrate nowadays $SrTiO_3$, MgO or $LaAlO_3$ substrates are also used for the film deposition [15].

2.4.1 Physical vapor deposition methods

These methods are extensively used for the thin film fabrication due to the benefits like dry processing, cleanliness and epitaxial growth. However, these techniques have the drawbacks such as low deposition rates, difficulty in stoichiometry control, high crystallization temperatures and high capital equipment acquisition. Physical vapor deposition methods require a vacuum to obtain sufficient flux of atoms or ions capable of depositing on the substrate [1].

2.4.1.1 Sputtering

Sputtering is the process of ejection of surface atoms from the target by momentum transfer from bombarding ions to surface atoms [16]. Since the sputtering produces a vapor of target material it is used for making various types of coatings such as planarized coatings for multilayered circuits, magneto-optical storage media, compact disks, optical multi layered coatings for mirrors and filters, luminescent coatings and thin films. Sputtering for film deposition is categorized into glow discharge (diode, triode and magnetron) and ion beam based on the sputtering source. In all the cases the particles are ejected through the momentum exchange from energetic particles to the target. However, the various sputtering source configurations cover quite different process and all have their particular advantages. Sputtering especially with ion beam and rf planar diode sources is widely used for film deposition [17]. In sputtering technique the target is made from the film forming material and it is held on a sputtering electrode receiving a voltage, and the substrate is disposed at predefined distance and opposite to the target. High-density plasma is made by producing a cusp field between the target and substrate. And a bias voltage is applied to the substrate surface in order to make ions of the plasma fall on the substrate for the film deposition [18]. Sputtering technique suffers from the problem of impurities raised mainly due to the erosion of surfaces of sputtering chamber than the intended target and by the working gas pressures (1-100 Pa) needed to ignite the electrical discharge.

2.4.1.2 Pulsed laser deposition

PLD is used for the deposition of insulators, semiconductors, metals, and polymer materials due to the salient features such as stoichiometry transfer, excited oxidizing species, simplicity in initial setup and compatibility with background pressures in the range from ultrahigh vacuum to 1 Torr. PLD technique is particularly attractive for the complex material film growth since it allows the stoichiometry transfer of the material. In this technique the photonic energy is coupled to the target material through the electronic processes. An intense laser pulse passes through the optical window of vacuum chamber and is focused onto the material to be deposited (target), where it is partially absorbed. The absorbed laser vaporizes or ablates significant amount of the target material in the form of luminous plasma plume. The ablated plume is re-condensed for film growth on the substrate surface. Growth process in reactive PLD may be supplemented by a passive or reactive gas or ion source [19]. However, the PLD technique has the disadvantages such as production of microscopic ejecta, impurities in target material, formation of crystallographic defects in the films due to the bombardment by high kinetic energy particles and inhomogeneous flux. Another drawback of the PLD method is that the thickness distribution of the film is non-uniform because of the highly forward-directed nature of the ablated plume [20].

2.4.2 Chemical deposition techniques

Chemical methods for the thin film deposition have the advantages such as better stoichiometry control, large area covering, cost-effectiveness and low temperature processing.

2.4.2.1 Chemical vapor deposition (CVD)

CVD is versatile method for the manufacturing of coatings, powders, fibers, composites and monolithic components due to the benefits like high deposition rates, cost-effectiveness, easier deposition of complex structures, low vacuum and flexibility to make changes in composition during the deposition as compared to the PVD techniques. This technique is essential for producing the semiconductors, and other electronic components. In CVD method the solid material is deposited on a heated substrate through the chemical reaction in vapor state. It is a vapor transfer process in which the deposition species are atoms or molecules or a combination of both. CVD technique is classified in to MOCVD, plasma CVD and many others based on the application, process and reactor used or type of precursors used for deposition [21]. For the deposition of thin film by CVD technique the precursor gas or gases are flown in to the chamber containing heated objects. Chemical reactions occur in the precursor gases near the heated object and it leads to film deposition on the hot surface. Film deposition is accompanied with the release of chemical by-products. These by-products and the non-reacted precursor gases are exhausted from the CVD chamber. However, CVD method has the several drawbacks such as volatile starting materials, deposition at elevated temperatures and toxic by-products [22].

2.4.2.2 Modified sol-gel technique for thin film deposition

As already discussed in section 2.2.3 the sol-gel technique is excellent technique for the deposition of films due to the advantages such as good homogeneity, low temperature annealing, large area covering and uniform deposition over the substrate. However for thin film deposition the gelation of sol has to be avoided or significantly delayed for stable precursor sol formation by suitable precautions in order to obtain the homogeneous coatings. Metal-alkoxide precursors used in the sol-gel technique undergo hydrolysis by the attack of water molecules. Extent of hydrolysis of sol is influenced by the nature of alkyl group (long/short chain, branched), water concentration, solvent type and temperature. Hydrolysis of metal alkoxide leads to the formation of metal hydroxide with simultaneous release of alcohol (Equation 2.1).

$$M(OR)_z + z\,H_2O \longrightarrow M(OH)_z + z\,ROH \qquad (2.1)$$

Hydrolysis and condensation lead to the formation of three dimensional networks. Based on the degree and type of poly-condensation colloidal particles in liquid phase (sol) are gradually converted to solid phase (gel). Poly-condensation reactions in the sol take place by alkoxolation (Equation 2.2) or oxolation (Equation 2.3) for the formation of metal-oxygen-metal bonds by the elimination of alcohol or water.

$$-M\text{-}OH + RO\text{-}M- \longrightarrow -M\text{-}O\text{-}M + ROH \qquad (2.2)$$

$$-M\text{-}OH + OH\text{-}M- \longrightarrow -M\text{-}O\text{-}M + H_2O \qquad (2.3)$$

Gelation of sol occurs due to the aggregation of the colloidal particles. Lewis acid properties of metal alkoxide are the reason for the hydrolysis-condensation of the sol. Therefore, gelation can be avoided or delayed through the chemical modification of the alkoxides. Chemical modification of the metal alkoxide is done simply through the solvent since the solvent acts as a true reagent. Organic solvents with hetero atoms like nitrogen or oxygen can interact strongly with the metal and replace the alkoxide group from it at molecular level. The new alkoxy groups make stable coordination with the metal which ultimately decreases the hydrolysis ability of the modified metal alkoxide. Moreover, the stability of the sol can be increased by the addition of bi-dentate ligands such as acetyl acetone or acetic acid to the sol. This helps to deposit the films in ambient atmosphere using the precursor sol [23]. The precursor sol made from the reagents such as metal alkoxides, metal acetates or metal nitrates and solvents is deposited on the substrate using a spin coater. The wet coatings are dried and decomposed to remove the solvent and organic moieties of the reagents. Finally the coating is annealed for the crystallization.

2.5 Steps involved in the deposition of BCZT films

2.5.1 BCZT precursor sol coating

BCZT ($Ba_{0.85}Ca_{0.15}Ti_{0.90}Zr_{0.10}O_3$) thin films were processed on Si/SiO_2/TiO_2/Pt (100) substrates following sol-gel spin coating technique. The BCZT precursor sol was made as described in the section 2.3.1. However, for the preparation of the BCZT sol for thin film deposition the solvent 2-methoxy ethanol was used instead of 2-propanol in order to avoid the gelation of the sol. To prevent cracks in the films the precursor sol was modified by adding polyvinyl pyrrolidone (PVP) binder with the mole ratio of 1:0.5 (BCZT:PVP). The PVP modified BCZT precursor sol was filtered through the 0.2 μm syringe filter. The Modified BCZT sol concentration was adjusted to 0.25 M. Then the sol was coated on the cleaned platinum coated silicon substrates using the spin coater with the 500 rpm for 10 sec followed by 3000 rpm for 30 sec (Fig. 2.4). Wet films were dried and decomposed for the removal of organic moieties. Finally the films were grown and annealed in ambient air and in oxygen-rich atmosphere. Decomposition and annealing of films were carried out in conventional tubular furnace.

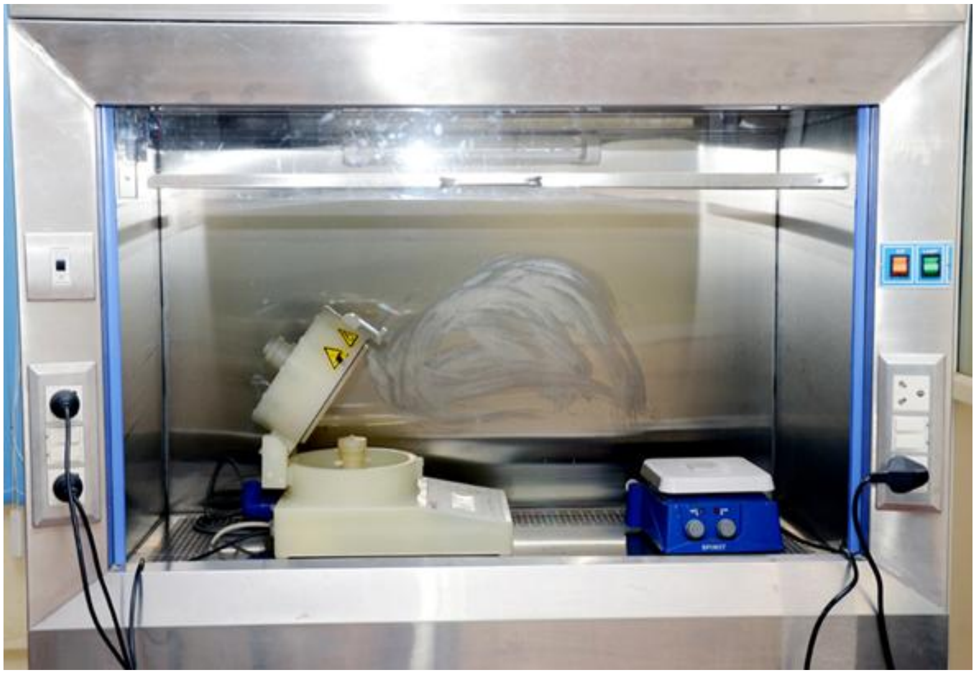

Fig. 2.4 Spin coating facility.

2.5.2 Crystallization of BCZT coatings

BCZT films were annealed for the crystallization in tubular furnace (Fig. 2.5). Conventional annealing is extensively used for the crystallization of films since the beginning of thin film technology. It is known that conventional annealing result larger size grains due to low heating rates and long process times. BCZT films were crystallized using tubular furnace at 700 and 800 ^{o}C temperatures with heating rate of 2 ^{o}C/min for an hour in ambient air as well as in oxygen-rich atmosphere.

Fig. 2.5 Tubular furnace with processing gas facility.

2.5.3 Electrode deposition

Electrodes with diameter of 250 μm were deposited over the BCZT films by sputtering technique for making electrical contact for the electrical property characterization (Fig. 2.6). For top electrode deposition a shadow mask is placed over the crystallized BCZT films. Then the BCZT films were loaded in to the sputtering system equipped with gold target and the electrode material was sputtered on the surface of the film.

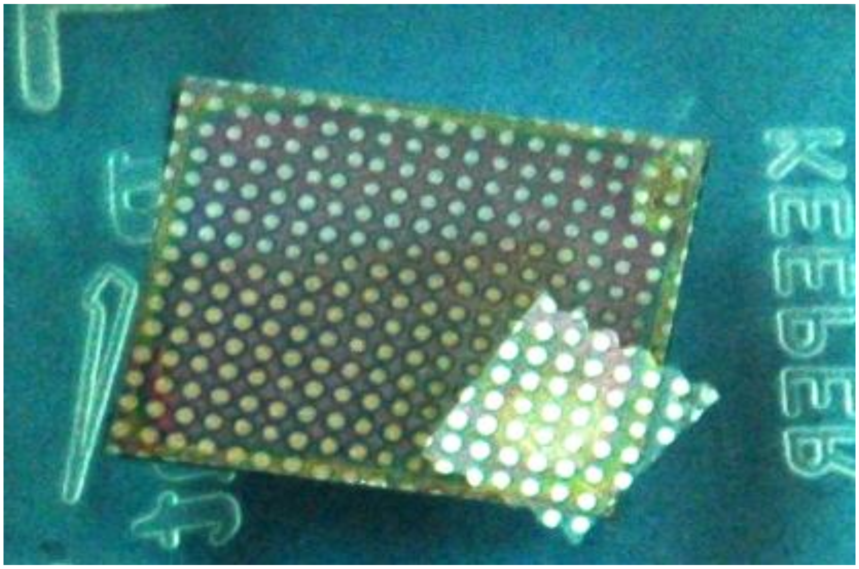

Fig. 2.6 Image of BCZT thin film.

2.6 Characterization techniques

It is very important to study the phase and microstructure of the synthesized BCZT nano-powders, bulk ceramic and thin film materials since the electrical properties are dependent on the nature of phase and microstructure of the material. Furthermore, it is necessary to evaluate the dielectric, ferroelectric and piezoelectric properties in order to assess the potential of the BCZT bulk ceramics and films.

2.6.1 Phase and microstructure analysis

Phase and crystal structure of the synthesized BCZT nano-powders, bulk ceramics and thin films were analyzed by X-ray diffraction technique whereas the microstructure was studied by the scanning electron microscope and transmission electron microscope.

2.6.1.1 X-ray diffraction (XRD)

X-ray diffraction is a versatile and non-destructive technique to characterize the materials properties such as phase, crystallite size, texture, residual stress, structure and defects of the variety of materials like powders, coatings, solids and liquid samples [24]. X-ray photons interact with the materials in several ways which lead to different absorption and scattering effects. Among these in an elastic scattering the energy of scattered radiation remains same and also it retains the phase relationship with the incident beam. As a result the X-rays that striking on the atoms of irradiated volume are scattered in all directions. However, constructive or destructive scattering of X-rays is seen due to the periodic arrangement of atoms in the crystals. This lead to characteristic diffraction phenomena and it is used to study the crystal structure of the materials. The principle of the XRD is dependent on the diffraction by the regular atomic planes and angle or energy-resolved detection of the diffracted signal. The geometrical elucidation for the XRD phenomenon (constructive interference) was given by W. L. Bragg which describes the condition for the diffraction as well as to derive the Bragg's law. The Bragg's equation is given as,

$$n\lambda = 2d_{hkl} \sin(\theta) \qquad (2.4)$$

Where n is the order of diffraction, λ is the wavelength of the incident X-rays, d_{hkl} is inter-planar spacing and θ is the angle of the diffracted beam. Therefore, the diffraction occurs for the lattice plane that satisfies the Bragg's equation in the case of the constructive interference. Phase is detected from the comparison of the XRD patterns of the unknown sample with the reference data base [25].

Phase of the BCZT nano-powder and BCZT bulk ceramics were characterized using the powder-XRD technique. For this purpose Philips X-ray diffractometer (Model: 'X' pert PW-3020, Japan) was used. The diffractogram is obtained by counting the detected intensity as a function of angle between the incidence and diffracted beams. However, the phase and crystal structure of the BCZT thin films were studied by grazing incidence X-ray diffraction (GIXRD) technique. For this purpose smart lab X- ray diffractometer (Rigaku, Japan) was used. In GIXRD configuration the primary beam reaches to the thin film at very small angles (usually in between 1 to 5^o). The small incidence angle reduces the penetration depth of the X-rays in order to avoid the reflection from the substrate, and hence the diffractogram is predominantly originated from the film material [26].

2.6.1.2 Scanning electron microscope (SEM)

Morphology of the BCZT bulk ceramics was analyzed using environmental scanning electron microscope (FEI, Quanta-400, USA). SEM is the important electron-optical instrument for the study of surface or near-surface microstructure of the specimens [27]. SEM consists of electron gun, condenser lenses, scan coils, objective lens and detector. The generated electron beam from the electron gun (thermionic tungsten filament) is accelerated to energy usually in between 1 to 30 keV. The beam diameter is reduced by the condenser lenses, as it strikes the specimen. The interaction of electron beam with specimen atoms generates different types of signals such as secondary electrons, transmitted electrons, backscattered electrons (BSE), characteristic X-rays, Auger electrons and cathodoluminescence. Secondary electrons are produced from the surface of the specimen. The signals detected from the secondary electrons are used to form the image of the specimen. Beam of electrons that are reflected due to the elastic scattering from the specimen is called as backscattered electrons. The BSE are emerged from the deeper areas of the specimen. Therefore, the resolution of BSE images is lower than the secondary electron images. These BSE are used to analyze the distribution of the different elements in the specimen. Characteristic X-rays are produced when the electron beam ejects the inner shell electrons, causing a high-energy electron to fill the shell and releases the energy. The energy of these X-rays is used to recognize the elements in the specimen.

Microstructure and thickness of the BCZT films is studied using the field emission scanning electron microscope (Zeiss, Supra-55, Germany). In FESEM the electron beam is produced from the field emission gun to achieve the better resolution [28].

2.6.1.3 Transmission electron microscope (TEM)

In TEM analysis a thin specimen was irradiated with the electron beam having the energy in the range of 60-150 keV. Specimen must be very thin usually in the range of 5 nm-0.5 µm depending on the nature of the sample and the resolution desired. Therefore, special preparation techniques are required to make the specimens for TEM study. TEM produces images with very high resolution due to the high localized elastic scattering to the region occupied by the screened coulomb potential of the atomic nucleus. The electron beam produced from the electron gun is passed through the condenser lenses in order to control the area of the specimen irradiated [27]. Transmitted electrons passed through the specimen are focused by the lenses behind the specimen to produce an image. The image is observed on a phosphor screen or a wide angle camera and these images are recorded by a device. Electron detection system in TEM usually is charged coupled device (CCD), which convert incoming electrons in to an electronic pulse per pixel. Various types of TEM imaging modes such as bright-field, electron diffraction and high-resolution imaging were developed to analyze the specimen effectively. Electron diffraction imaging mode is frequently used to study the crystal structure of the specimen. Electron diffraction of the specimen is formed due to the constructive and destructive interference of the elastically scattered electrons. From the electron diffractogram the phase, lattice parameters and crystal orientation is determined. Under high-resolution TEM imaging the patterns correspond to atomic positions is observed [25]. Morphology and phase of the BCZT nano-powders was studied using High-resolution TEM (FEI Tecnai G^2 30ST). Furthermore, the thickness and phase of the BCZT thin films was also analyzed by the HRTEM.

2.6.2 Dielectric property measurements on the BCZT bulk ceramics

Dielectric properties of BCZT bulk ceramics were studied in the frequency range of 1 kHz to 100 kHz using Agilent E4980A precision LCR meter. For the dielectric property measurement of the ceramics parallel circuit mode (C_p-D) was selected in the LCR meter. Temperature dependant dielectric properties of the BCZT ceramics were studied by the lab made dielectric set up. BCZT ceramics were kept in the furnace by placing in the high temperature sample holder which is connected to LCR meter. Furnace temperature was controlled with the aid of PID controller. Both the LCR meter and PID controller were linked with the computer and interfaced with a Labview program. The LCR meter determines the capacitance and dissipation factor with an accuracy of ±0.05 % and ±0.0005 respectively [29].

2.6.3 Ferroelectric property studies on the BCZT bulk ceramics

P-E and S-E hysteresis loops of BCZT bulk ceramics were recorded using the advanced ferroelectric evaluation system of M/s aixACCT systems, GmbH, Germany [Fig. 2.7]. The triangular waveform is used for the both measurements. BCZT sintered disks are placed in the piezo sample holder unit (PSHU) which allows testing of ceramics with variety of sample geometries. This PSHU is connected with an external high voltage Trek 610 HV 10 kV amplifier. For measurements, FE-module and TF 2000HS analyzer were used with hysteresis software version of v2.4.0.0. The FE-module is composed with three amplifiers with an optimum signal to noise ratio. Frequency for the measurements is controlled by the drive limits of the amplifier. The current for the measurements using TF 2000HS analyzer is selected by the current amplifier. To obtain best results the current range should be closer the current response of the specimen. The current response is dependent on the composition and geometry of the test material, and also it depends on the drive frequency and amplitude. Usually the current range selection is in between 10 pA to 1 A.

2.6.3.1 P-E loop measurements

For P-E loop measurements aixACCT system uses the virtual ground feedback method. In this method current is measured using operational amplifier with feedback resistor and it uses a current to voltage converter. P-E hysteresis loops were recorded by measuring the current or charge response due to the applied electric field. Magnitude of polarization depends on the composition, geometry of the capacitor and the applied electric field. The quantity of current (I) is calculated from the charge (Q) and the voltage variation with time (slew rate). The slew rate is given by dv/dt for the ferroelectric capacitor when P is the polarization, V is applied voltage, A is the area of the capacitor [30]. The quantity of current flow during the polarization switching is given by the equation (2.5).

$$Q = D.A \sim P.A$$

$$I = \frac{dQ}{dt} = A.\frac{dP}{dV}\frac{dV}{dt} \qquad (2.5)$$

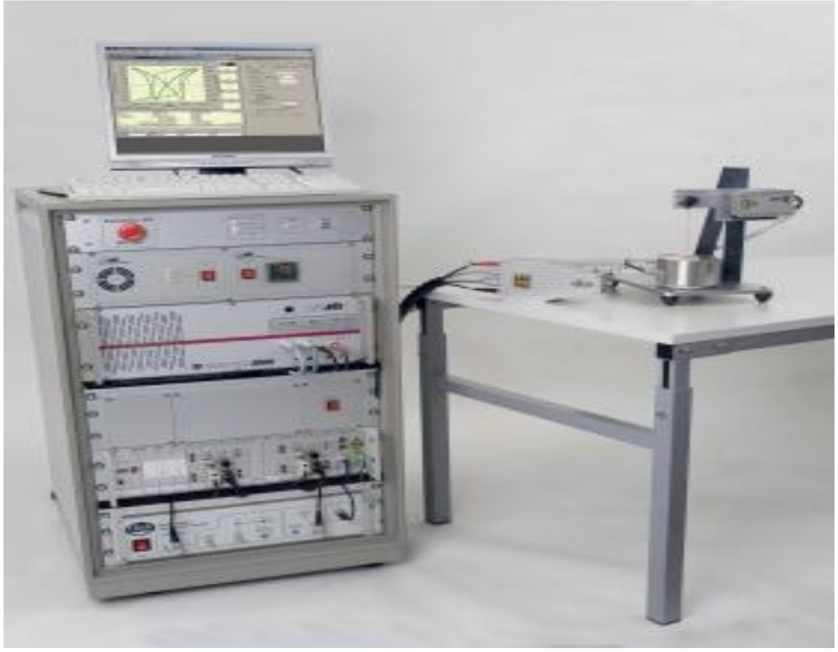

Fig. 2.7 Image of aixACCT ferroelectric evaluation setup.

2.6.3.2 S-E loop measurements

S-E loop measurements were done by the aixACCT ferroelectric system connected with the class 2M laser interferometer. S-E measurement setup includes sample holder, laser source and mirror. The laser beam position can be moved on to the sample with the help of the adjustment screws and consequently the reflected beam shifts as well. The electromechnical response of the BCZT bulk ceramics was studied by applying the electric field at 1 Hz frequency. For the S-E loop tracing the direction of the applied electric field and the measurement direction was kept same. In this study uni-polar S-E loops were recorded for the detection of converse d_{33}. The converse d_{33} of the BCZT ceramics was calculated from the slope of the unipolar S-E loop.

2.6.4 Dielectric and ferroelectric property measurements on the BCZT thin films

P-E hysteresis loops, capacitance-voltage (C-V) loops, frequency dependant dielectric constant and dielectric loss, leakage current and polarization fatigue of the BCZT thin films were analyzed using semiconductor characterization system (Keithly SCS-4200, USA) (Fig. 2.8). The SCS-4200 system provides the solution for the DC I-V, C-V and pulse characterization for the specimen. This SCS-4200 system gives high speed measurement with accuracy by an embedded Windows-based computer with Keithley interactive test environment (KITE). The SCS-4200 supports source measuring units (SMU), C-V measurement units, pulse generators and oscilloscopes. The configuration of SCS-4200 includes two power source-measure units (SMUs) and a ground unit. In C-V measurements the capacitance can be measured in the range of femto-farads (fF) to nano-farads (nF) at the frequencies of 1 kHz to 10 MHz. Moreover, the linear capacitance-frequency sweep can be configured and modified with this system [31]. Polarization of the BCZT film was measured at 1 kHz and 10 kHz frequencies. For this purpose SCS-4200 was configured with the hardware of KTEI 8.2, PMU and RPMs of SCS-4225 model. This configuration measures the current and voltage directly. The charge of the capacitor is detected from the current measurements. Polarization of the ferroelectric capacitor is calculated from the charge [32]. Polarization fatigue of the BCZT films was measured by applying the repetitive bipolar pulses with amplitude of 5 V at 1 MHz frequency.

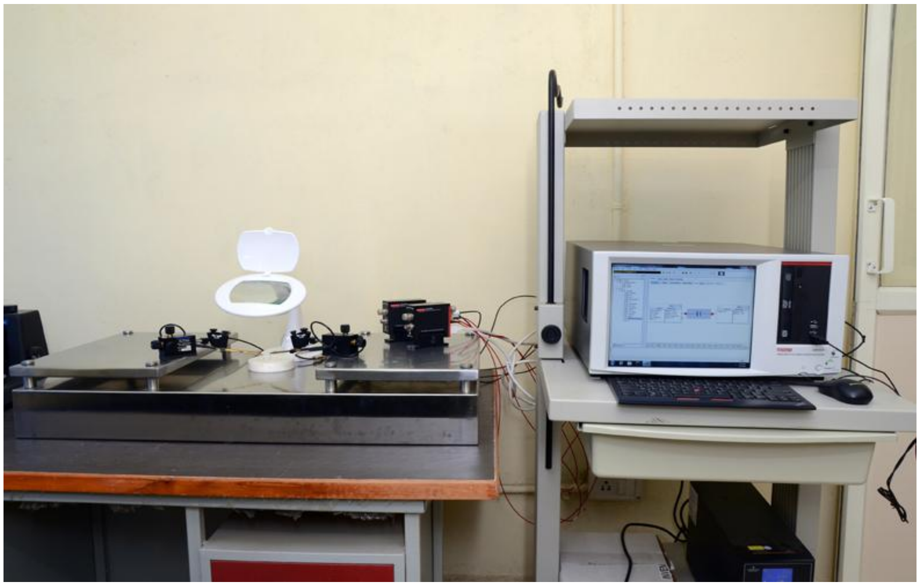

Fig. 2.8 Image of semiconductor characterization system.

2.6.5 Piezoelectric property studies on the BCZT thin films

Local piezoelectric response in the BCZT thin films was investigated by piezo-response force microscopy (PFM). PFM is the variant of atomic force microscopy (AFM). Topography, surface roughness and local piezoelectric deformation of the films were studied by using the PFM (Dimension icon AFM, Bruker AXS GmbH, Germany). PFM measurements are based on contact mode in AFM, for which the instrument is equipped with function generator and lock-in amplifier. PFM is also used for the study of domain configuration and switching mechanism. AFM mode is used for the topography imaging. For the piezoelectric measurements platinum coated silicon tip was employed by applying the DC bias of -12 to +12 V with AC driving voltage of 5 V_{rms} and driving frequency of 345 kHz at the single points on the BCZT film. The applied voltage causes deformation in the film (converse piezoelectric effect) which makes the deflection of the cantilever and it is detected by the lock-in amplifier. The local converse d_{33} of the film is calculated from slope of the displacement vs. voltage plots [33].

2.7 References

1. G. H. Haertling, J. Am. Ceram. Soc., **82[4]** (1999) 797-818.
2. M. M. lencka, R. E. Riman, Crystal growth technology, William Andrew applied science publishers., (2003) 271-297.
3. T. R. N. Kutty, R. Balachandran, Mat. Res. Bull., **19** (1984) 1479-88.
4. L. Wang, X. Zhang, Y. Ma, M. Yang, Y. Qi, Mater. Lett., **164** (2016) 623-26.
5. C. D. E. Lakeman, D. A. Payne, J. Am. Ceram. Soc., **75 [11]** (1992) 3091-96.
6. R. Roy, Science., **238** (1987) 1664-69. DOI: 10.1126/science.238.4834.1664.
7. R. J. Henderson, H. W. Chandler, A. R. Akisanya, H. Barber, B. Moriarty, J. Euro. Ceram. Soc., **20** (2000) 1121-28.
8. J. K. Mackenzie, R. Shuttleworth, Proc. Phys. Soc. B., **62** (1949) 833.
9. I. W. Chen, X. H. Wang, Nature., **404** (2000) 168-171.
10. M. Shukla, S. Ghosh, N. Dandapat, A. K. Mandal, V. K. Balla, J. Mater. Sci. Chem. Eng., **4** (2016) 71-78.
11. M. Oghbaei, O. Mirzaee, J. Alloys Comp., **494** (2010) 175-189.
12. P. Muralt, J. Micromech. Microeng., **10** (2000) 136-146.
13. Y. Zhang, Q. F. Zhou, H. L. W. Chan, C. L. Choy, Thin solid films., **375** (2000) 87-90.
14. X. D. Wu, P. Tiwari, Metal oxide films on metal, US patent., (1995) 5470668,.
15. C. M. Foster, Z. Li, M. Buckett, D. Miller, P. M. Baldo, L. E. Rehn, G. R. Bai, D. Guo, H. You, K. L. Merkle, J. Appl. Phys., **78[4]** (1995) 2607.
16. K. Seshan, Hand book of thin film deposition processes and technology, Noyes publication, New York (2002).
17. J. L. Vossen, W. Kern, Thin film process II, Academic press, INC., San Diego (1991).

18. H. Tateishi, H. Saito, S. Sasaki, M. Horiuchi, Sputtering process and an apparatus for carrying out the same, US patent., (1989) 4853102.
19. P. R. Willmott, J. R. Huber, Rev. Mod. Phys., **72[1]** (2000) 315.
20. R. Eason, Pulsed laser deposition of thin films: Applications-led growth of functional materials, John Wiley and sons, New Jersey (2007).
21. H. O. Pierson, Handbook of chemical vapor deposition: principles, technology and applications, Noyes publications, New York (1999).
22. J. H. Park, T. S. Sudarshan, Chemical vapor deposition, ASM international, Ohio (2001).
23. T. Schneller, R. Waser, M. Kosec, D. Payne, Chemical solution deposition of functional oxide thin films, Springer, London (2013).
24. M. Ermrich, D. Opper, XRD for the analyst, PANalytical, Kassel (2011).
25. G. Hubschen, I. Altpeter, R. Tschuncky, H. G. Herrmann, Materials characterization using non-destructive evaluation methods, Woodhead publishing (2016).
26. M. Birkholz, Thin film analysis by X-ray scattering, Wiley-VCH Verlag GmbH & Co. KGaA, Weinheim (2006).
27. L. Reimer, Transmission electron microscopy, Springer (1984).
28. P. J. Goodhew, J. Humphreys, R. Beanland, Electron microscopy and analysis, Taylor and Francis, London (2001).
29. Agilent E4980, A precision impedance analyzer data sheet, Agilent technologies.
30. Hysteresis software version 2.4.0.0 user manual, aixACCT GmbH, Germany.
31. SCS-4200 data sheet, Kiethley, USA.
32. SCS-4200 application note series (No. 3141), Kiethley, USA.

33. J. A. Christman, R. R. Woolcott, Jr., A. I. Kingon, R. J. Nemanich, Appl. Phys. Lett., **73 [26]** (1998) 3851.

Chapter 3

Synthesis, phase, microstructure and electrical properties of the BCZT bulk ceramics

In this chapter phase, microstructure and electrical property investigations on the BCZT bulk ceramics is presented.

3.1 Introduction

Sol–gel processing offers better homogeneity and a lower phase formation temperature of the desired oxide phase due to the molecular scale mixing in the precursor. Sol-gel processing technique is also economical and involves simple processing methodology [1]. There are very few reports on bulk BCZT materials synthesized by sol-gel technique where the piezoelectric properties of the BCZT ceramics sintered at 1550 ^{0}C were reported [2-5]. Sahoo et al. [2] and Tian et al. [3] in their published work reported only the synthesis and structural characterizations of BCZT nanoparticles obtained by citrate gel synthesis technique. Electrical properties were not reported in their published work. V. S. Puli et al. [4] reported sol-gel synthesis of BCZT ceramics; however, piezoelectric properties were not reported. Praveen et al. [5] first reported dielectric, ferroelectric and piezoelectric properties of sol-gel synthesized BCZT ceramics but the electrical properties were reported for the samples sintered at a very high temperature (1550 ^{0}C).

In the present work, the ferroelectric BCZT nano-powders were synthesized by sol-gel technique. The precursor sol is synthesized from inexpensive chemical precursors. The synthesized BCZT materials were sintered at considerably lower temperatures (1300-1400 ^{0}C). In this study, we have demonstrated that the sol-gel synthesized BCZT ceramic powders could be sintered at lower temperatures exploiting the advantage of having nanopowders with improved sinterability and considerably higher piezoelectric properties could still be obtained in the low temperature sintered samples. Low temperature sintered sample showed considerably large strain which is comparable to that of the high-end PZT. Moreover, a simple methodology, ease of fabrication, opportunity of using inexpensive precursors coupled with low densification temperature offer enormous flexibility for large scale fabrication of the ceramic material.

3.2 Experimental procedure

The $Ba_{0.85}Ca_{0.15}Ti_{0.9}Zr_{0.1}O_3$ nano-powders were made by the following the sol-gel method as discussed in the section 2.3.1. For the processing of BCZT bulk ceramics, the synthesized nano-crystalline powders were pressed by CIP into pellets at room temperature and subsequently sintered at 1300, 1350 and 1400 °C for 4 hours in air. The relative density of the sintered pellets was estimated by measuring the experimental density using Archimedes principle. Room temperature XRD studies on both the powder samples as well as the sintered ones were carried out using Cu-kα radiation. The powder samples for TEM observation were prepared by dispersing the powder in methanol and adding a few drops of the suspension on a carbon-coated TEM grid. The growth of the particle size of the polycrystalline samples in the pellet was studied by SEM. Quantitative elemental analysis of the sintered sample was done by electron probe microanalysis (EPMA) on the Bakelite- mounted, diamond-polished and gold-coated pellet. A high temperature automated horizontal dilatometer (Linseis L75HX1600) was used to record the thermal expansion curves for the green and sintered BCZT samples. Dielectric properties, polarization (P) vs. electric field (E) and strain (S) vs. (E) measurements were carried out at room temperature.

3.3 Results and discussion

3.3.1 Structural characterization of BCZT nanocrystalline powders

For the structural characterization of the BCZT powders, XRD was performed on the powders calcined at different temperatures in air. The powder-XRD results are shown in Fig. 3.1.

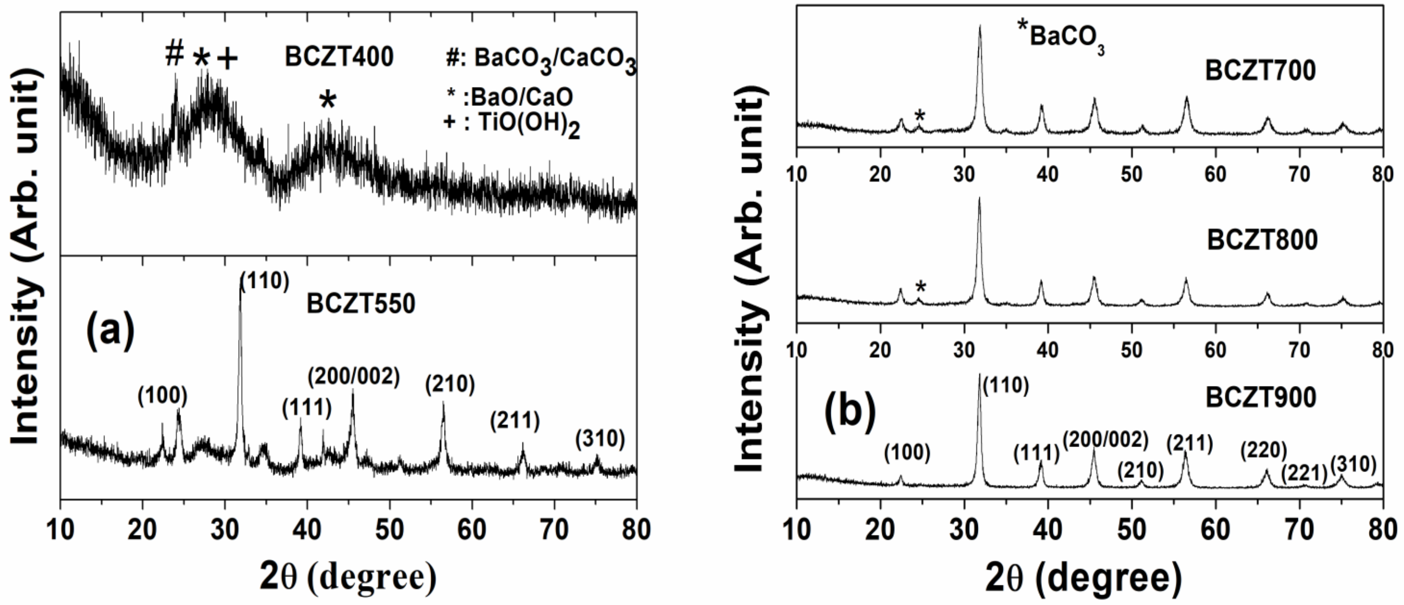

Fig. 3.1 (a) and (b) powder-XRD patterns of BCZT samples calcined at different temperatures showing the phase formation.

The powder-XRD patterns of BCZT powder calcined in the temperature range 400- 900 ^{o}C are shown in Fig. 3.1. XRD characterization reveals that at lower calcination temperatures (400-500 ^{o}C) dried BCZT gel powders form metal hydroxides and carbonates (Fig. 3.1 (a)) which then decompose to nanocrystalline metallic oxides at higher temperatures followed by their gradual conversion to nano-crystalline BCZT phase. This finding is in agreement with the results reported by Wang et al. [6]. However, in contrast to the XRD results reported by Wang et al. which showed 650 ^{o}C to be the initiation temperature for phase formation, in the present work, the phase formation starts at a very low temperature ~500 ^{o}C. The conversion from nanocrystalline mixed oxide phase to crystalline phase is almost completed at 700 ^{o}C except minute amounts of un-reacted components indicated by two tiny extra peaks in the powder-XRD patterns (Fig. 3.1 (b)). The reflection at 2θ of 24.5 degree in Fig. 3.1 (b) are aroused from the un-reacted barium carbonate [7]. However, a fully pure BCZT phase is obtained only at 900 ^{o}C. The earlier reports on the synthesis of BCZT from the respective oxides by solid state technique [8, 9] revealed the coexistence of tetragonal and rhombohedral phase which are usually indicated by splitting of the (200) and (211) peaks. However, in the present work, the nano-crystalline BCZT powder has been synthesized by chemical technique and the XRD peaks obtained from the scanning of the nanocrystalline powders are broad where the tetragonal splitting is submerged by the appearance of broad peaks. However, the coexistence of tetragonal and rhombohedral phases has been confirmed from the Raman spectra of the sintered BCZT disk which is discussed in the subsequent sections of this chapter.

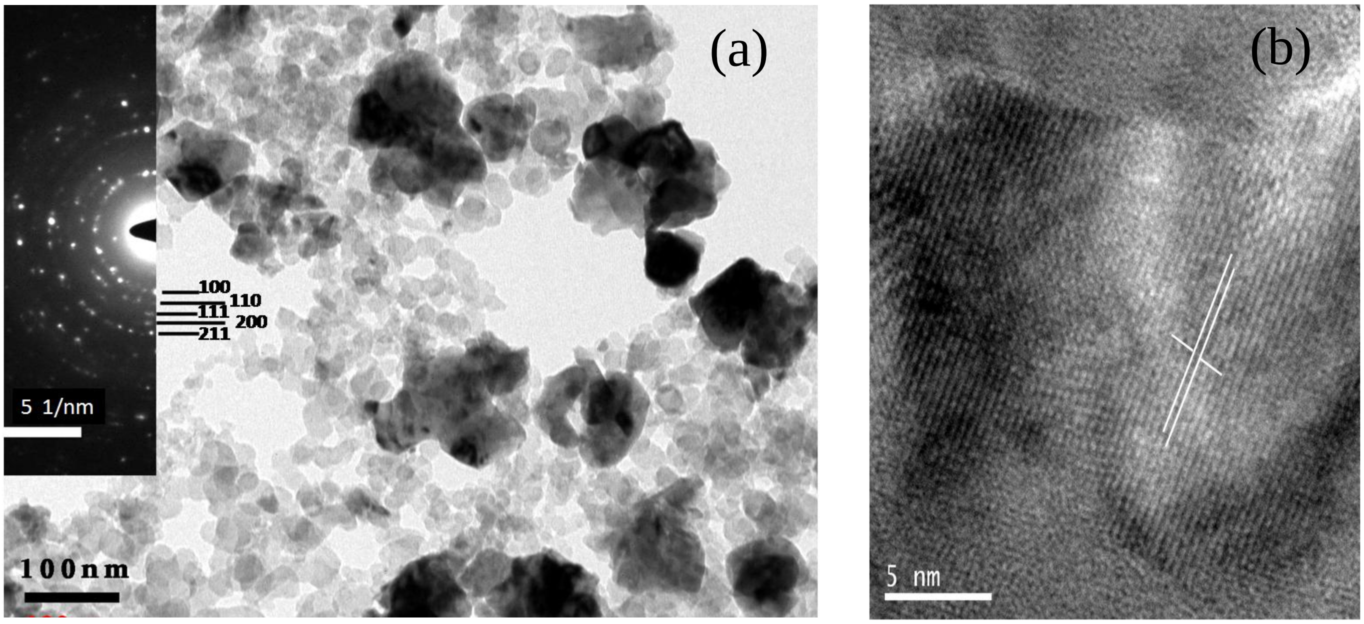

Fig. 3.2 (a) TEM image of the BCZT nano-powder calcined at 900 ^{o}C with the electron diffraction pattern (inset) and (b) HRTEM of a BCZT nano-particle.

Fig. 3.2 (a) shows the size distribution for most of the nanoparticles is 5-30 nm. However, few bigger nanoparticle-agglomerates are also present in the distribution. The d-values calculated from the diffraction pattern (Fig. 3.2 (a) inset) for the (100), (110), (111) and (211) planes are matching the same calculated from the powder-XRD patterns (Fig. 3.1 (b)). HRTEM (Fig. 3.2 (b)) of a BCZT particle shows lattice spacing of the (100) plane of a BCZT grain is 2.86 Å.

3.3.2 Studies on sinterability of the nano-crystalline BCZT powders

Sinterability of the synthesized nano-crystalline BCZT powders was studied by a dilatometer to identify the suitable sintering temperature for densification. High temperature automated horizontal dilatometer was used to record the thermal expansion curves for the green and sintered BCZT samples. The samples were heated in air in alumina sample holder assembly. The system is interfaced to computer and is designed to automatically measure the percent of linear change corresponding to time and temperature of the test sample under controlled heating and cooling rates. Fig. 3.3 shows the typical dilatometric plot of the BCZT green pellet. The sample was heated to 1350 ^{o}C with a heating rate of 5 ^{o}C/min. It is observed that significant shrinkage occurred at ~1050 ^{o}C, which is indicated by the initiation of sharp slope change at this temperature. Up to 1350 ^{o}C shrinkage of ~1.1 mm was observed, which is quite reasonable to achieve a good densification at this temperature.

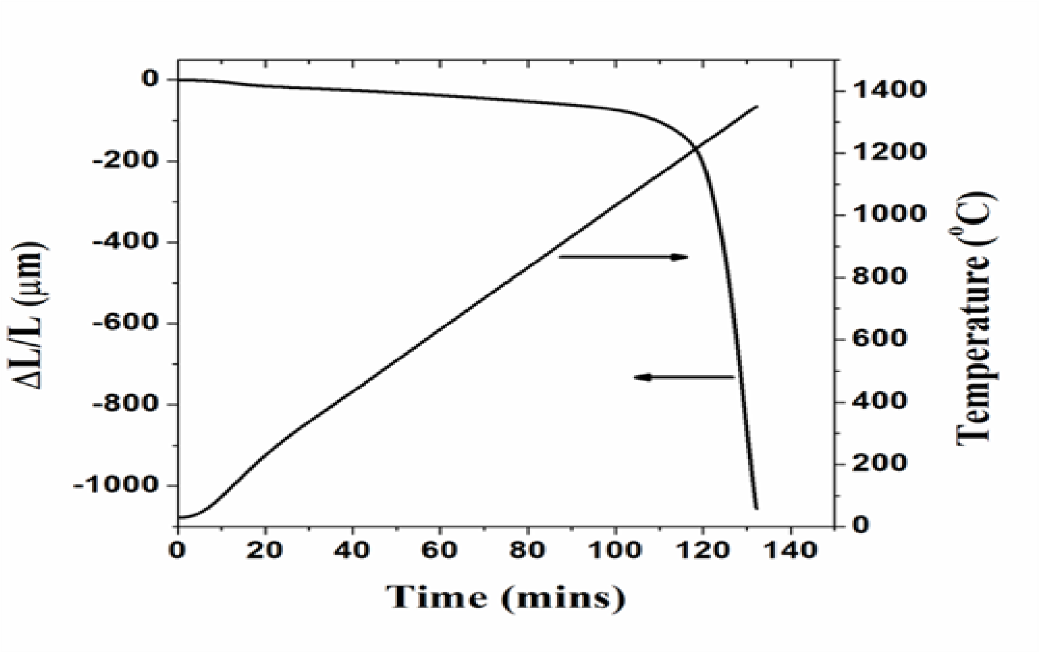

Fig. 3.3 Typical shrinkage behavior for the BCZT green compact.

3.3.3 Consolidation and structural characterization of dense BCZT materials

For densification, the green pellets made from the calcined BCZT powders through cold isostatic pressing (CIP) were sintered at different temperatures in air. Following the results of the dilatometric study the green pellets were sintered at 1300 ^{o}C, 1350 ^{o}C and 1400 °C (Here afterwards abbreviated as BCZT1300, BCZT1350 and BCZT1400 respectively) in air for 4 hours. The relative densities of the sintered samples were measured by Archimedes principle. The relative densities of the BCZT1300, BCZT1350 and BCZT1400 samples were found to be 94.2%, 94.5% and 93.6%, respectively. To observe the microstructure and the grain growth, SEM image of the fractured surface of the 1350 ^{o}C sintered sample were recorded and the results are shown in Fig. 3.4. The BCZT grains with sizes ranging from 5-25 µm are visible in the microstructure.

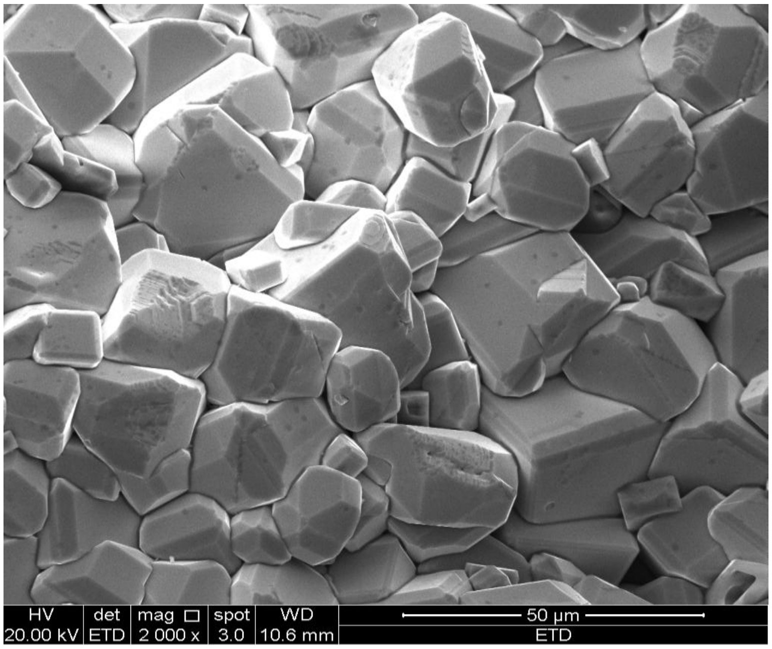

Fig. 3.4 SEM image of the fractured surface of the BCZT1350 sample.

Fig. 3.5 (a) shows the powder-XRD patterns of the BCZT1350 ceramic indicating the presence of single phase polycrystalline BCZT. From the powder-XRD pattern it can be concluded that stoichiometry in the sample remains almost unchanged even at high sintering temperature. The splitting of the (200) peak indicates the coexistence of rhombohedral (R3m) and tetragonal phase (P4mm) in the sintered sample. Similar observations have also been reported by other researchers [2, 8, 10, 11]. However, splitting of the peaks is not always observed in the sintered

BCZT samples due to relatively higher fraction of rhombohedral phase. For example, the splitting of the (200) peak was not apparent for the BCZT1300 and BCZT1400 samples. There are possibilities for relatively higher fraction of rhombohedral phase in BCZT ceramics since the same was evidenced for the BCZT films annealed at higher temperature (Subsequent studies of this thesis, page No. 98) [12]. Earlier studies also indicate that higher fraction of rhombohedral phase decreases the magnitude of splitting of (200) peak [13]. Moreover, the smaller size grains in BCZT ceramics also decrease the magnitude of peak splitting since these ceramics were synthesized from sol-gel technique.

Hence, XRD slow scans were performed in the 2θ range: 44.5-46^o for those two samples and the results are plotted in Fig. 3.5 (b). The broad asymmetric peaks were deconvoluted into (002) and (200) peaks using Gaussian fitting.

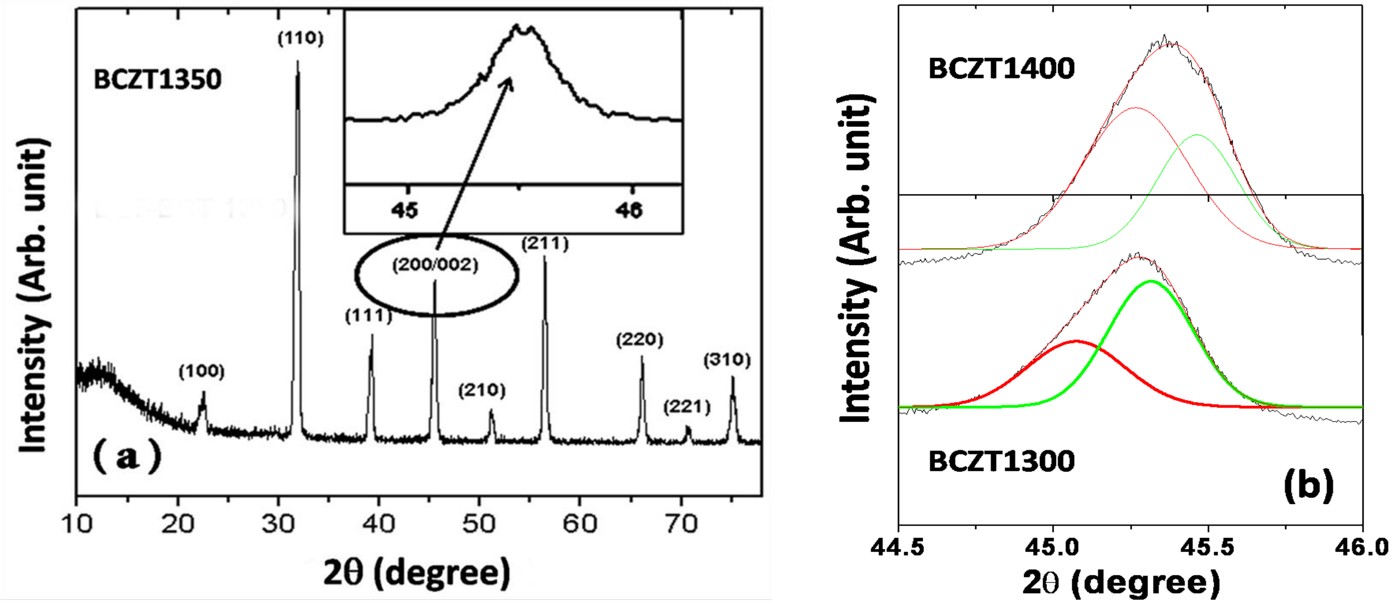

Fig. 3.5 (a) Powder-XRD patterns of BCZT1350 ceramics (the inset shows the peak splitting of (200) peak) and (b) slow scan XRD plot in the range: 44.5-46^o of 2θ with peak deconvolution.

3.3.4 Spectroscopic characterization

The existence of tetragonal phase is also confirmed by the Raman spectra recorded on the sintered BCZT samples. Raman spectra is an important spectroscopic tool effectively used by several group of researchers to characterize tetragonal phase in presence of cubic phase in different ceramics e.g. ZrO_2, $BaTiO_3$. The existing non-centro-symmetry in tetragonal phase is believed to be the reason for the occurrence of multiple Raman active nodes. The Raman spectra of the samples (Fig. 3.6) show three bands at 305, 520 and 726 cm^{-1} among which the band at 305 cm^{-1} is the signature of the tetragonal phase of BCZT [6]. The band at 726 cm^{-1} also signifies the presence of tetragonal phase of BCZT whereas the band at 520 cm^{-1} can be attributed to both cubic and tetragonal barium titanate ($BaTiO_3$) (pure and substituted $BaTiO_3$).

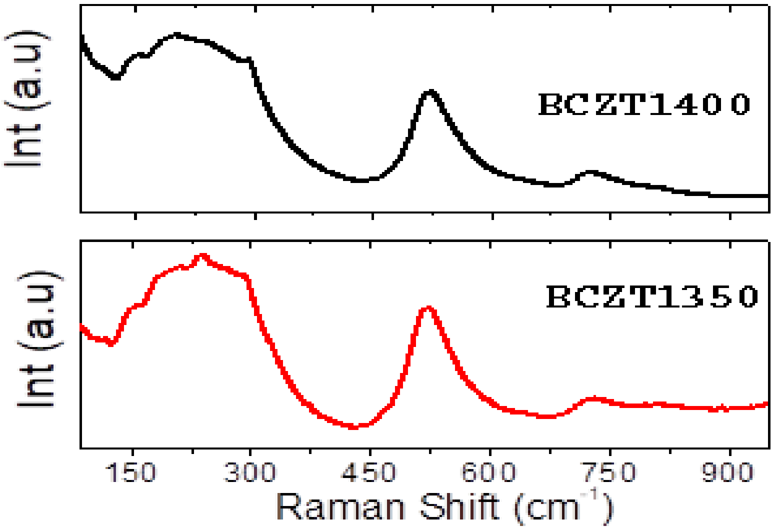

Fig. 3.6 Raman spectra of the BCZT samples sintered at 1350 and 1400 °C.

Diffuse reflectance (DRS) U.V-visible spectra (i.e., $F(R) = (1-R)^2 /2R$, where R is the reflectance) measured as a function of photon energy (eV) for BCZT1350 and BCZT1400 samples shown in Fig. 3.7. DRS spectrum depicts a linear absorption edge which indicates the absence of any crystal transitions, and it is attributed to highly stable Ti^{4+} and Zr^{4+} ions (i.e. d^0-ion) [14]. The band gap (E_g) for both BCZT samples was estimated by extrapolating the linear region of DRS spectra. As compared to the samples sintered at 1400 ^oC (E_g =3.15 eV) the samples sintered at 1350 ^oC depicts better insulating character because of its higher band gap value i.e. E_g =3.23 eV.

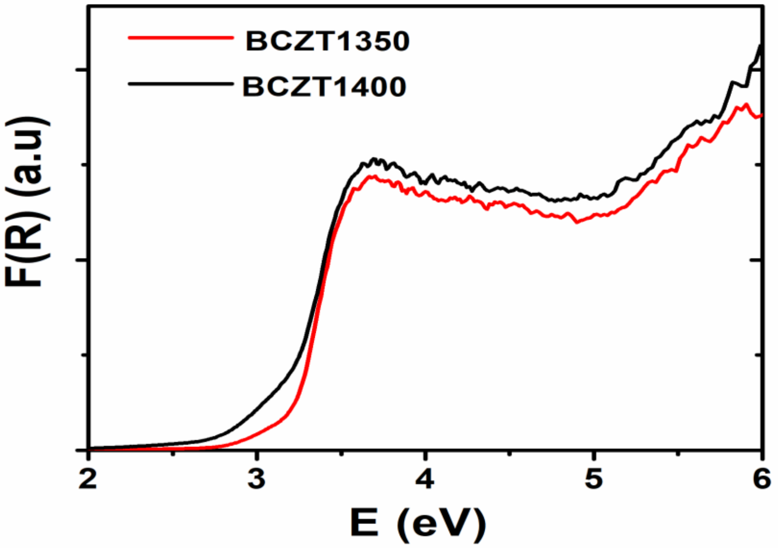

Fig. 3.7 UV-Vis spectra of the BCZT1350 and BCZT1400 samples.

3.3.5 Detection of elemental concentration in the sintered pellet by EPMA

The electron probe microanalysis (EPMA) was performed on the polished sintered pellets for quantitative estimation of the elements in the sintered samples. Microanalysis data were acquired on fifteen arbitrary points on the polished and gold coated sample. The results obtained from a 1350 ^0C sintered sample are plotted and shown in Fig. 3.8 (a). The results indicate the existence of a very good homogeneity in the sintered sample as expected, with respect to the elements present throughout the sample although the figure shows little variation in the line plots. Very small variation in concentration at different points is as expected and usually occurs in samples that are not polished perfectly to yield microscopic flat surfaces. These variations are well within the error limit of EPMA quantitative measurements. The EPMA line scans for the same sample show the variation of elemental concentration in counts with the scanning distance (Fig. 3.8 (b)). The line scans also show small variation in elemental concentration with scanning distance.

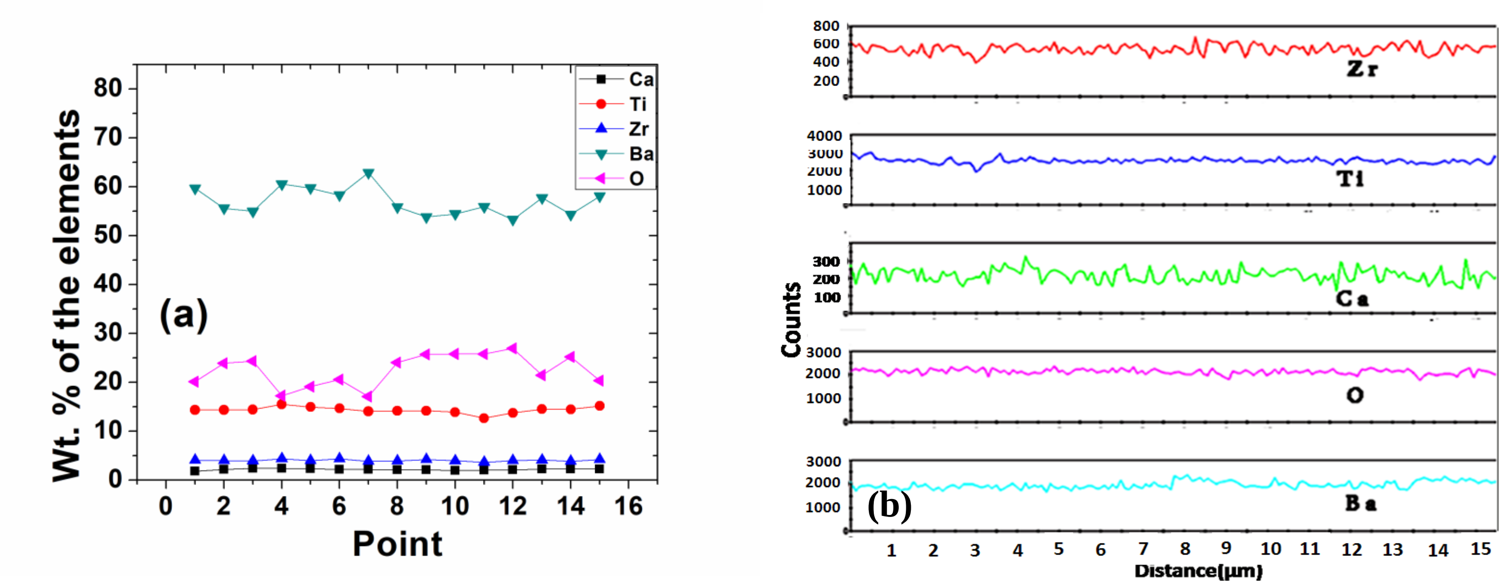

Fig. 3.8 (a) Variation of elemental concentration at different points of a sintered pellet and (b) EPMA line scan for the elements present in BCZT sintered sample.

3.3.6 Typical dilatometric behavior of sintered sample

The tetragonal to cubic transition was determined by heating the sintered BCZT sample in dilatometer and the corresponding curve is shown in Fig. 3.9. The plot clearly indicates the tetragonal to cubic phase transformation as we pass through the Curie point (~100 ^{o}C). Also, a broad transition was observed. The phase transition appears to be broad because the change in lattice parameters starts from low temperature and the same takes place within broad region of temperature. The values of T_C obtained from both dilatometric heating and the dielectric study (discussed in the subsequent section) of the sintered samples are observed to be in good agreement with each other.

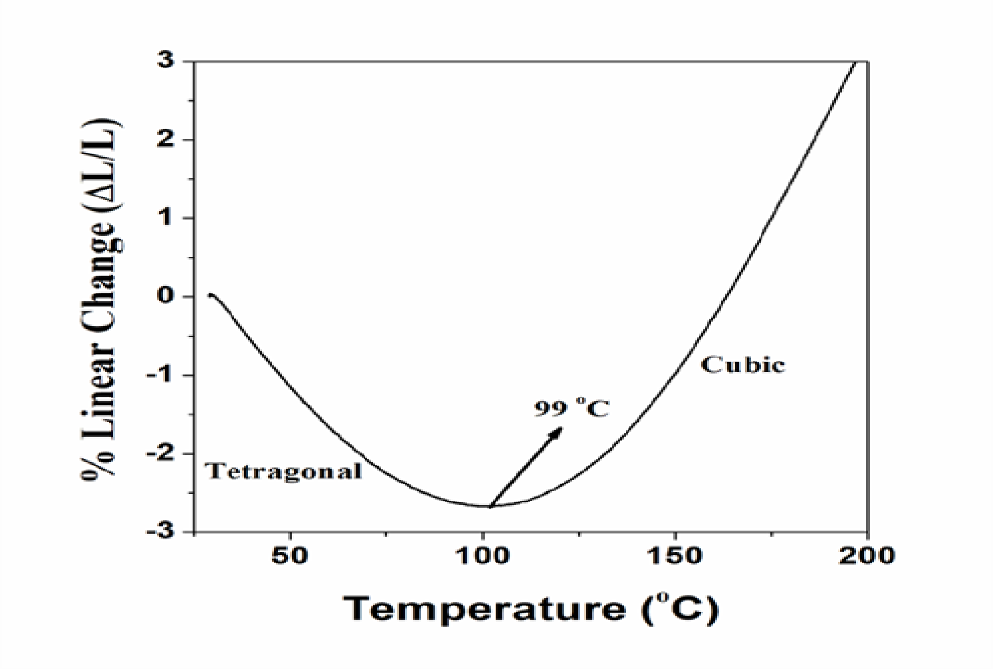

Fig. 3.9 Typical dilatometric plot of sintered BCZT sample showing the tetragonal-cubic phase transition.

3.3.7 Dielectric property characterization

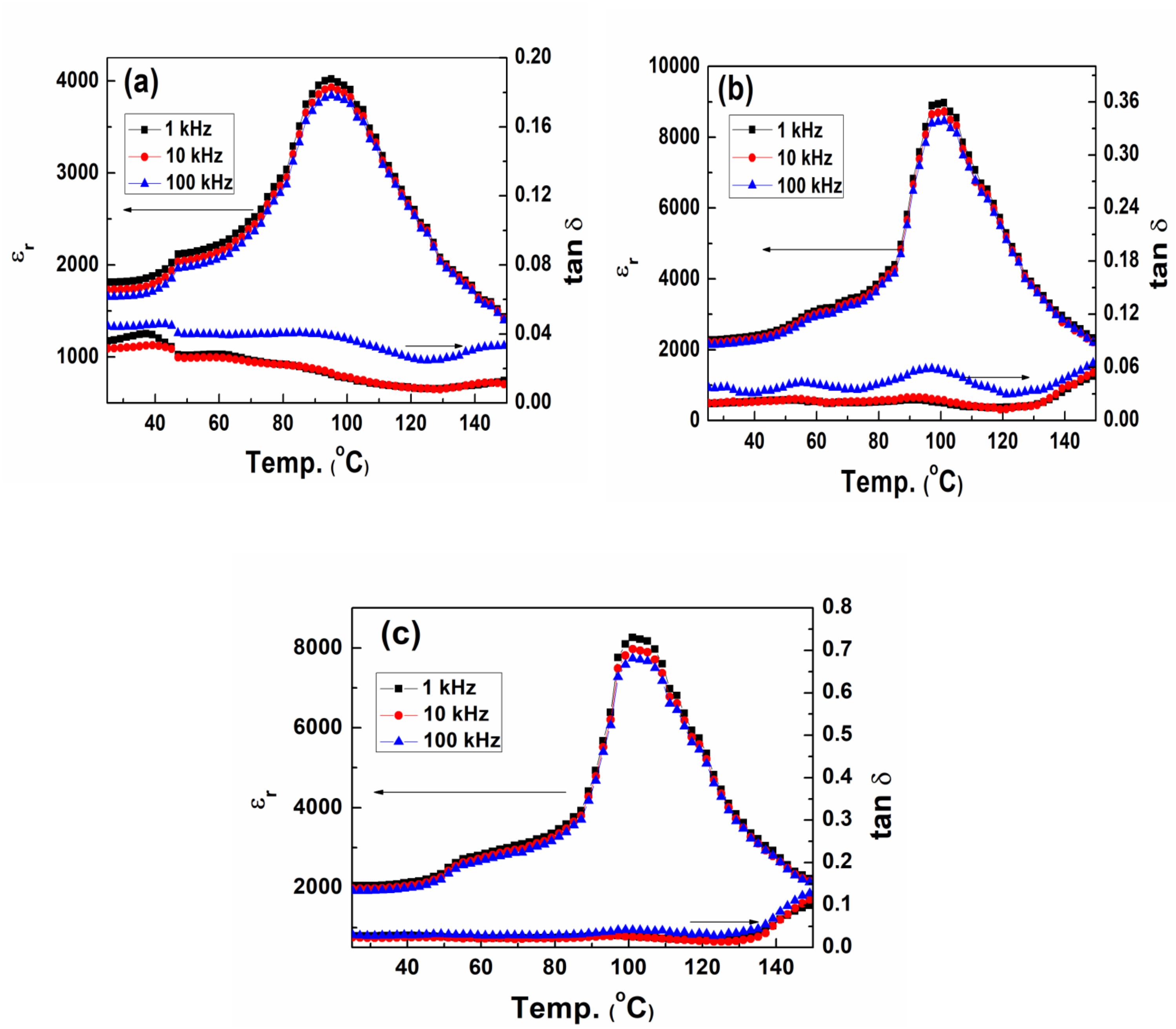

Fig. 3.10 Dielectric spectra of BCZT ceramics sintered at (a) 1300 °C (b) 1350 °C and (c) 1400 °C.

Fig. 3.10 shows the temperature dependence of dielectric constant (ε_r) and dielectric loss (tan δ) at different frequencies of the BCZT ceramic samples, sintered at (a) 1300 °C (b) 1350 °C and (c) 1400 °C, respectively. Values of ε_r and tan δ of the BCZT ceramic samples, sintered at different temperatures, are given in table 3.1. In all the BCZT ceramic samples, ε_r increases with the increase of temperature and reaches maximum ($\varepsilon_{r\ m}$) at Curie point (T_C). The ε_r-T spectra of the BCZT samples show two anomalies, one at T_s and another at T_C. These anomalies can be attributed to occurrence of different phase transitions in the BCZT system [15]. The first phase transition at ~50 ^oC corresponds to the rhombohedral–tetragonal ($T_{R–T}$) and the second phase transition at ~100 ^oC corresponds to tetragonal-cubic ($T_{T–C}$) transitions, respectively. Further these phase transitions can be related to the instability of temperature dependent low frequency optical soft mode. Near these phase transition temperatures, frequency of the soft mode tends to zero and the associated lattice displacement becomes unstable, which leads to phase transition [16, 17].

T_C of the BCZT ceramic samples increases with the increase of sintering temperature. With the increase of internal stress in a ferroelectric material, its free energy increases and Curie point decreases. Generally, internal stress in a ceramic can be relieved by porosity or grain-boundary sliding [18]. If internal stress is relieved by pores, the lower density ceramics should have a higher T_C than that of dense ceramics. Internal stress of the dense ceramics is mainly relieved by grain-boundary sliding. Thus, the dense ceramics with fine grains should have higher T_C than those of the coarse grains. This suggests that in the present study the effect of relieving of internal stress by grain-boundary sliding is dominant. Therefore, the increment of T_C with the increase of sintering temperature of the BCZT ceramic samples can be associated with the relieving of internal stress by grain-boundary sliding. Both at RT and at T_C, the BCZT ceramic samples sintered at 1350 °C showed highest ε_r and lowest dielectric loss, which suggest about the optimized sintering conditions.

Table 3.1 Dielectric properties of the sintered BCZT ceramic samples.

Sample	ε_r (25 °C) at 1 kHz	$\varepsilon_{r\,m}$ at 1 kHz	Loss (25 °C) at 1 kHz	T_s (°C)	T_C (°C)
BCZT1300	1813	4022	0.03	46	95
BCZT1350	2400	8917	0.015	58	100
BCZT1400	2097	8315	0.02	52	101

All samples show a relatively broad peak in the dielectric constant around the phase transition temperature (T_C) (Fig. 3.10) which is typical for relaxor-ferroelectric or ferroelectric materials with a diffuse phase transition [19, 20]. Diffuse phase transitions (DPT) take place in the ferroelectric materials where microscopic inhomogeneity leads to composition fluctuations. The microscopic regions with slightly different compositions have similar but slightly different Curie points resulting a diffused phase transition. Smolenskii and Rolov [21, 22] believed that Curie points of different microscopic regions have a Gaussian distribution around some average T_C. However, in the present case, for the BCZT samples, there is no frequency dispersion in transition temperature indicating a non-relaxor type composition.

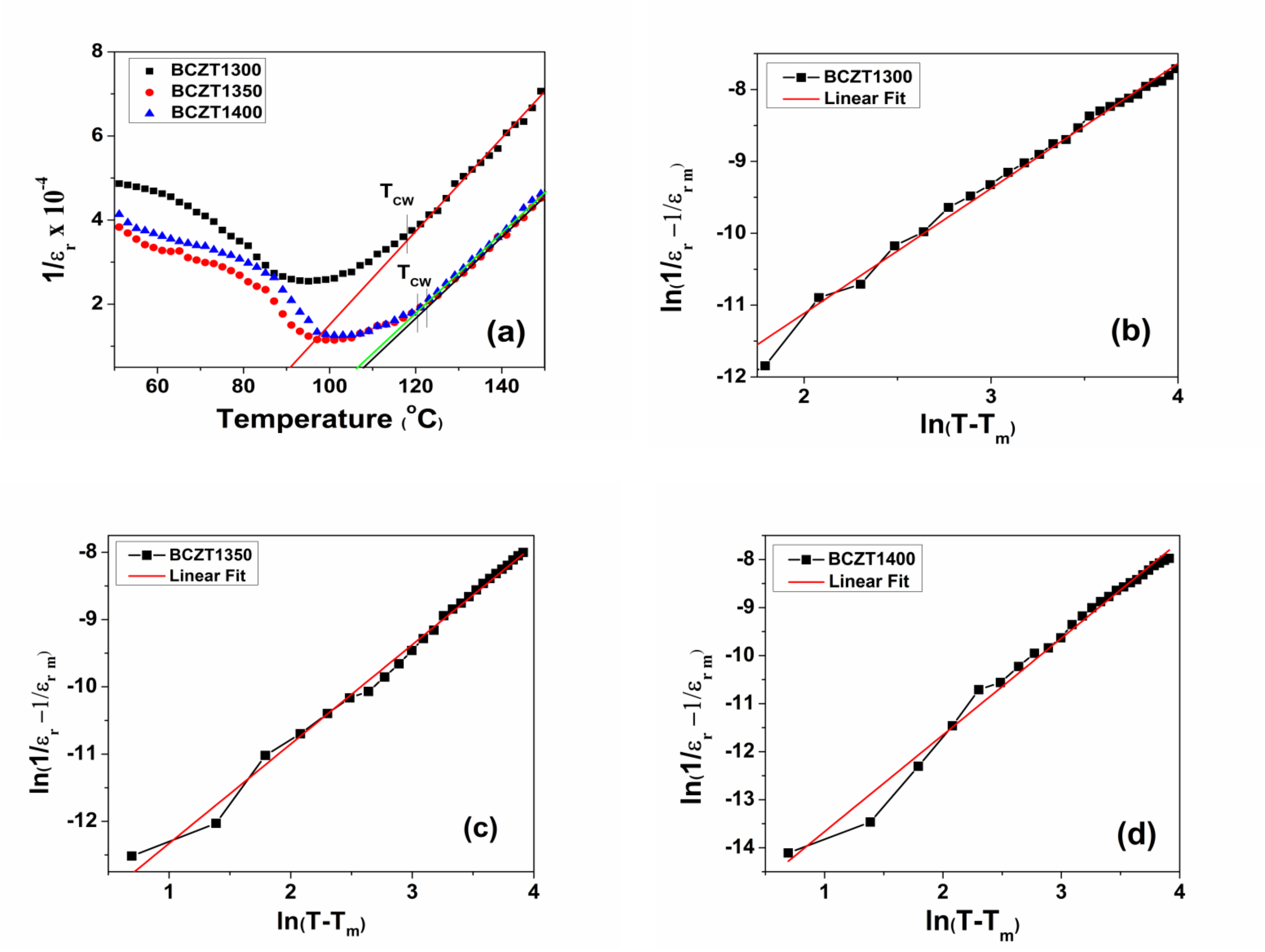

Fig. 3.11 (a) Variation of inverse dielectric constant as a function of temperature, plots of $\ln(1/\varepsilon_r - 1/\varepsilon_r\ m)$ vs. ln(T-Tm) derived from the dielectric spectra recorded at 1 kHz for (b) BCZT1300, (c) BCZT1350 and (d) BCZT1400 ceramics.

It is known that for normal ferroelectric materials, above the T_C, variation of dielectric constant with temperature follows Curie-Weiss law:

$$\frac{1}{\varepsilon_r} = \frac{(T-T_0)}{C} \tag{3.1}$$

Where, T_0 is the Curie-Weiss temperature and C be the Curie-Weiss constant. The plot of inverse dielectric constant vs. temperature at 10 kHz for BCZT1300 and BCZT1350 in the high temperature regions are shown in Fig. 3.11 (a). The extrapolation of the linear fittings in the high temperature regions shows that linearity of the plot is good except a narrow temperature range above T_C (region close to the phase transition) and hence it can be concluded that dielectric behavior doesn't completely follow Curie-Weiss law at temperatures above the T_C. The temperatures (T_{CW}) from which the dielectric behavior shows departure from Curie-Weiss law, for BCZT1300, BCZT1350 and BCZT1400 are given in table 3.2.

Uchino and Nomura [23] in their published work on diffused phase transition of $PbMgNbO_3$ and $PbZnNbO_3$, attempted to fit the experimental data for variation of dielectric constant with temperature above phase transition temperatures with different equations derived from modified form of Curie-Weiss law. They attempted to fit the experimental data to the following quadratic law (Equation (3.2)):

$\frac{1}{\varepsilon_r} - \frac{1}{\varepsilon_{r\,m}} = \frac{(T-T_m)^2}{2\,\varepsilon_{r\,m}\sigma^2}$ (3.2) (Assuming Curie points of different microscopic regions, have a Gaussian distribution around some average T_C in a diffused phase transition).

Where ε_r is dielectric constant, $\varepsilon_{r\,m}$ and T_m is the maximum dielectric constant and corresponding temperature (dielectric maxima temperature) at and σ be the standard deviation of the Gaussian function. They observed that plot of reciprocal permittivity as a function of $(T-T_m)^2$ deviated remarkably from straight line in the temperature range near the averaged Curie point ($T- T_m < 30^oC$) and it is not deviated in the higher temperature range. Similar phenomenon has also been observed in Fig. 3.11 (a) where reciprocal permittivity is plotted as a function of ($T-T_m$) for the BCZT samples. Based on their observation Uchino and Nomura [23] tried to establish some empirical equation which can explain the real phenomenon. They determined that the following equation:

$$\frac{1}{\varepsilon_r} - \frac{1}{\varepsilon_{r\,m}} = C^{-1}(T - T_m)^{\gamma} \qquad (3.3)$$

This may provide the best fit to the experimental results. Where C is Curie-Weiss constant and γ is the diffusivity coefficient. Uchino and Nomura concluded that this generalized equation would work not only for relaxor-ferroelectric material but also for ferroelectric materials with sharp or diffused phase transitions. $\gamma = 1$ for a classical Curie-Weiss ferroelectric material and $\gamma = 2$ for a system with a completely diffused transition.

Therefore, the diffuseness in phase transition for the BCZT samples was measured following the equation (3.3) developed by Uchino and Nomura. The deviation from Curie-Weiss law is measured by fitting the ε_r - T curve at the temperature range of $T > T_m$ with the equation (3.3). In Fig. 3.11 (b), $\ln(1/\varepsilon_r - 1/\varepsilon_{r\,m})$ is plotted as a function of $\ln(T-T_m)$ and the slope of the straight line fitted to the logarithmic plot gives the value of γ. For the present samples the values of γ at three different frequencies are given in table 3.2. For BCZT1300 and BCZT1350 the values of γ are ~1.75 and ~1.5 respectively indicating partial diffused phase transition. However, for BCZT1400 the value of γ is ~2.0 which indicates completely diffused phase transition. The higher value of γ for BCZT1400 could be attributed to the inhomogeneity developed due to higher sintering temperature and this finding is concurrent to the conclusion made by L.E. Cross et al. [19, 20] who believed that microscopic inhomogeneity leads to diffuseness in phase transition.

Table 3.2 The temperatures (T_{CW}) from which the dielectric behavior shows departure from Curie-Weiss law and diffusivity coefficients (γ) for the sintered BCZT samples.

Sample	**T_{CW} (^{0}C) at 1 kHz**	**T_{CW} (^{0}C) at 10 kHz**	**T_{CW} (^{0}C) at 100 kHz**	**γ at 1 kHz**	**γ at 10 kHz**	**γ at 100 kHz**
BCZT1300	117	119	118	1.75	1.77	1.77
BCZT1350	123	123	122	1.51	1.53	1.54
BCZT1400	119	120	119	2.02	2.11	2.05

3.3.8 Ferroelectric and piezoelectric property characterization

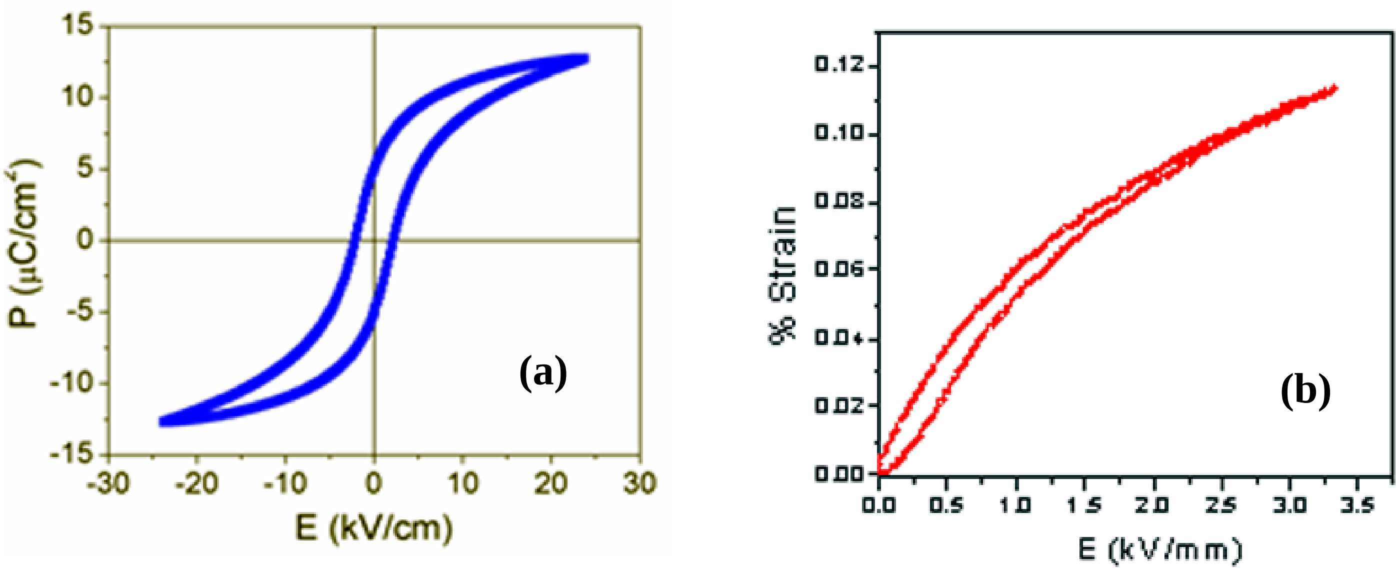

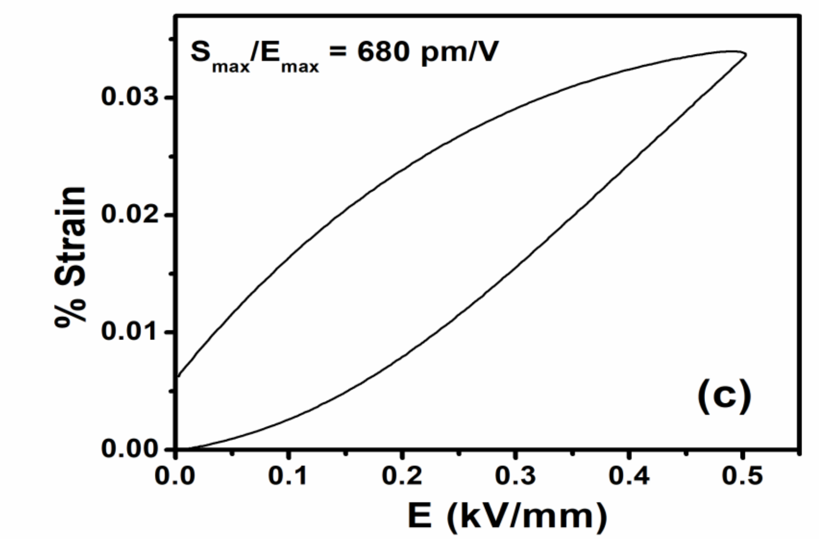

Fig. 3.12 (a) P vs. E hysteresis loop, (b) S vs. E plot for BCZT up to 3.5 kV/mm and (c) Plot of S vs. E for BCZT up to 0.5 kV/mm.

Fig. 3.12 (a) shows the typical P vs. E hysteresis loop for BCZT1350 sample. Since the sample sintered at 1350 °C showed better dielectric properties, measurements of ferroelectric and piezoelectric properties were performed on the same one. The P_{max} and P_r values observed for the sample are 13 and 6 μC/cm^2, respectively. This level of polarization can be compared to the polarization data reported by V. S. Puli et al. [4] who obtained P_r of 3-6 μC/cm^2 for the BCZT ceramic samples synthesized by sol-gel technique. Ferroelectric materials exhibit strain besides polarization under the applied electric field due to converse piezoelectric effect. In this study the strain measurements were performed at high electric field of 3.5 kV/mm in order to know maximum available strain in BCZT ceramics. In Fig. 3.12 (b) unipolar strain vs electrical field up to 3.5 kV/mm was plotted at a frequency of 1 Hz for a poled BCZT sample. The sample exhibits electrostrain of ~0.12% and the level of strain are higher than that observed in ultrasoft PZT-5H, undoped PZT and PZT-4 [7]. Strain of the piezoelectric material is increased with increase of electric field due to domain alignment. However, at very high fields the increment in strain is decreased due to saturation in domains alignment [24]. Therefore, the converse piezoelectric coefficient (d_{33}) was calculated from the strain measured at low electric field of 0.5 kV/mm in order to show maximum converse d_{33} for BCZT ceramics. Fig. 3.12 (c) shows the unipolar strain loop for the poled BCZT ceramics measured up to 0.5 kV/mm and at a frequency of 1 Hz. A maximum strain of 0.0375% is obtained under a relatively low electrical field of 0.5 kV/mm. The converse piezoelectric coefficient (d_{33}) is measured from the ratio of the maximum strain to peak electric field S_{max}/E_{max}, which was found to be 680 pm/V. The large strain and high converse piezoelectric coefficient measured at such low electric field clearly shows the soft elastic nature of the BCZT crystal lattice [2].

3.4 Conclusions

BCZT bulk ceramics were prepared following sol-gel technique. Phase formation of BCZT commenced at ~500 ^{o}C and a fully single phase structure was obtained at 900 ^{o}C. Characterization by XRD and Raman spectroscopy of the sintered pellet showed a mixture of rhombohedral and tetragonal phases. BCZT ceramic samples sintered at 1350 °C showed highest ε_r (8917) and lowest dielectric loss (0.015). Phase transition temperature of the BCZT ceramic samples increases with the increase of sintering temperatures. The P_{max} and P_r observed for a sintered BCZT ceramic is 13 and 6 μC/cm^2 respectively. The sintered BCZT ceramic exhibits electrostrain of ~0.12% and the level of strain were found to be higher than that observed in ultrasoft PZT-5H, undoped PZT and PZT-4.

3.5 References

1. G. H. Haertling, J. Am. Ceram. Soc., **82[4]** (1999) 797-818.

2. G. K. Sahoo, R. Majumder, J. Mater. Sci.: Mater, Electron., **25** (2014) 3515-3519.
3. Y. Tian, Y, Gong, D. Meng, Y. Li, B. Kuang, J. Electron. Mater., **49 [8]** (2015) 2890.
4. V. S. Puli, A. Kumar, D. B Chrisey, M. Tomozawa, J. F. Scott, R. S. Katiyar, J. Phys. D: Appl. Phys., **44 [39]** (2011) 495002.
5. J. P. Praveen, K. Kumar, A. R. James, T. Karthik, S. Asthana, D. Das, Cur. Appl. Phys., **14** (2014) 396-402.
6. Z. Wang, K. Zhao, X. Guo, W. Sun, H. Jiang, X. Han, X. Tao, Z. Cheng, H. Zhao, H. Kimura, G. Yuan, J. Yin, Z. Liu, J. Mater. Chem. C., **1** (2013) 522-530.
7. M. C. B. Lopez, G. Fourlaris, B. Rand, F. L. Riley, J. Am. Ceram. Soc., **82 [7]** (1999) 1777–86.
8. W. F. Liu, X. Ren, Phys. Rev. Lett., **103** (2009) 257602.
9. H. Bao, C. Zhou, D. Xue, J. Gao, X. Ren, J. Phys. D: Appl. Phys., **43** (2010) 465401.
10. B. Li, J. E. Blendell, K. J. Bowman, J. Am. Ceram. Soc., **94** (2011) 3192.
11. M. C. Ehmke, S. N. Ehrlich, J. E. Blendell, K. J. Bowman, J. Appl. Phys., **111** (2012) 124110.
12. S. Rangaswamy Reddy, V. V. Bhanu Prasad, Sandip Bysakh, Vishnu Shanker, Joydip Joardar, Subir Roy, J. Am. Ceram. Soc., **102** (2019)1277-86.
13. S. M. Gupta, J. F. Li, D. Viehland, J. Am. Ceram. Soc., **81 [3]** (1998) 557–64.
14. T. Karthik., R. Ranjith, S. Asthana, AIP Adv., **4** (2014) 017111.
15. N. Chaiyo, D. P. Cann, N. Vittayakorn, J. Mater. Sci., **50** (2015) 6171–6179.
16. E. Tasarkuyu, A. Coskun, A. E. Irmark, S. Akturk, G. Unlu, Y. Samancioglu, A. Yucel, C. Sarikurkcu, S. Aksoy, M. Acet, J. Alloys Compd., **509** (2011) 3717–3722.
17. K. V. R. Prasad, A. R. Raju, K. B. R. Varma, J. Mater. Sci., **29** (1994) 2691–2696.

18. X. Chen, H. Y. Ma, W. Ding, Y. Zhang, X. Zhao, X. Liang, P. Liu, J. Am. Ceram. Soc., **94 [10]** (2011) 3364–3372.

19. L. E. Cross, Ferroelectrics., **151 [1]** (1994) 305-320.

20. L. E. Cross, Ferroelectrics., **76 [1]** (1987) 241-267.

21. G. A. Smolensky, Jpn. J. Phys. Soc., **28 [Suppl.]** (1970) 26–37.

22. B. N. Rolov, Sov.Phys, Solid-state (Engl. Transl.)., **6 [7]** (1965) 1676-78.

23. K. Uchino, S. Nomura, Ferroelectr. Lett., **44** (1982) 55-61.

24. Ajeet Kumar, V. V. Bhanu Prasad, K. C. James Raju, A. R. James, J. Mater. Sci: Mater. Electron., **26** (2015) 3757-65.

Chapter 4

Phase, microstructure and electrical properties of microwave sintered BCZT bulk ceramics

In this chapter the effect of microwave sintering on the microstructure and electrical properties of BCZT ceramics is discussed.

4.1 Introduction

Microwave sintering is emerged as a new technique for the sintering of the variety of materials due to the advantages such as reduced sintering temperature and time, uniform grain size distribution, higher density, improved mechanical and electrical properties. Microwave energy is a form of electromagnetic radiation with frequency range of 300 MHz – 300 GHz. In microwave heating the material couples with the microwave radiation, absorbs the electromagnetic radiation volumetrically and transforms it in to the heat. This interaction of microwave energy with molecules of the material result the benefits like enhanced diffusion, reduced energy consumption, rapid heating rates, low sintering temperatures, and selective heating [1].

In the present work lead free ferroelectric $Ba_{0.85}Ca_{0.15}Ti_{0.90}Zr_{0.10}O_3$ ($0.5Ba(Zr_{0.2}Ti_{0.8})O_3$-$0.5(Ba_{0.7}Ca_{0.3})TiO_3$) ceramics with 95.2 % of theoretical density and finer grains were obtained from chemically synthesized powders by microwave sintering. Microwave sintered BCZT ceramics showed higher density, higher T_C, higher dielectric constant, and low dielectric loss. In addition to that, density and electrical properties of the microwave sintered samples are compared to that of the conventional sintered samples. Moreover, higher phase transition temperature of polycrystalline ($0.5Ba(Zr_{0.2}Ti_{0.8})O_3$-$0.5(Ba_{0.7}Ca_{0.3})TiO_3$) composition, which falls on the cubic–tetragonal–rhombohedral tricritical point (TCP) and offers best piezoelectric properties among all BCZT compositions, was not investigated earlier. H. Bao et al. [2] demonstrated higher T_C for the BCZT sample with the composition: $Ba(Zr_{0.15}Ti_{0.85})O_3$–$53(Ba_{0.8}Ca_{0.2})TiO_3$. However, such higher T_C was accompanied with lower piezoelectric properties as the composition was little away from TCP.

4.2 Experimental methods

BCZT green compacts were made as discussed in the section 3.2. The green compacts were sintered at 1300 ^oC and 1350 ^oC in air for 20 minutes in a furnace with microwave heating facility (Sample code names: BCZT1300-20min and BCZT1350-20min). For comparison of microstructure and electrical properties, some of green compacts were sintered conventionally at 1300 ^oC for 4 hours in a box-type furnace (Sample code name: BCZT1300-4h). The relative density of the BCZT ceramics was calculated by measuring the experimental density using Archimedes principle. Room temperature XRD studies on both the BCZT nano-crystalline powder samples as well as the sintered ceramics were carried out using Copper-kα radiation. Microstructure and grain growth in the BCZT ceramics were analyzed by SEM. Dielectric and ferroelectric properties of the BCZT ceramics were recorded at room temperature.

4.3 Results and discussion

4.3.1 Phase and microstructure characterization

Phase analysis was carried out by XRD for the BCZT nano-powders calcined at 900 ^oC temperature for 1 hour in air and the results are shown in Fig. 4.1. Powder-XRD patterns of the BCZT nano-powders indicate the presence of polycrystalline perovskite structure.

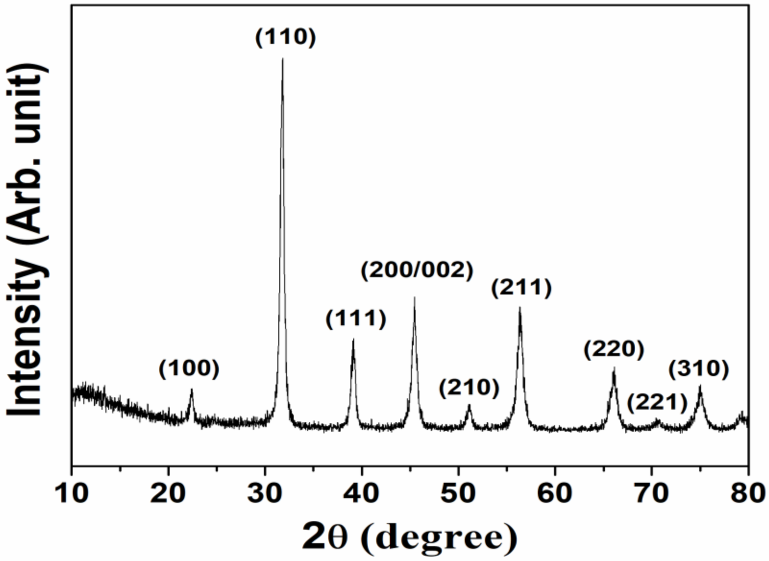

Fig. 4.1 XRD patterns of BCZT nano-powder sample.

The powder-XRD patterns of the BCZT pellets sintered by both the methods at 1300 ^{o}C showed the presence of single phase polycrystalline BCZT (Fig. 4.2). From the powder-XRD pattern it can be concluded that the elemental stoichiometry in the sample remains almost unchanged after sintering at high temperature. Average crystallite size (P) of the BCZT ceramics was calculated using the equation (4.1) (Debye-Scherrer formula)

$$P = \frac{K\lambda}{\beta \cos\theta} \qquad (4.1)$$

where K= 0.89 (constant), λ = 1.5406 Å for Cu-kα radiation, θ = Bragg's angle and β = Full Width at Half Maxima for the single (110) peak which accounts for the broadness of the peak [3]. The calculated crystallite size of the BCZT1300-20min and BCZT1300-4h samples are 16 nm and 32.6 nm, respectively. The densities of the sintered pellets: BCZT1300-20min and BCZT1350-20min reached 5.48 and 5.38 g/cm^3 i.e. 95.2% and 93.4 % of the BCZT theoretical density. The theoretical density of BCZT is considered to be 5.76 g/cm^3 [4]. It is to be mentioned that many researchers reported maximum 90-95% density could be achieved for similar BCZT composition by sintering in conventional furnace in the temperature range of 1400 -1500 ^{o}C for 2-4 hours in air. For example, H. Bao et al. [2] reported density of 5.185 i.e. 90% of the theoretical density for the BCZT with a composition: $Ba(Zr_{0.15}Ti_{0.85})O_3$–$0.53(Ba_{0.8}Ca_{0.2})TiO_3$ by sintering the same at 1450 ^{o}C for 3 hours.

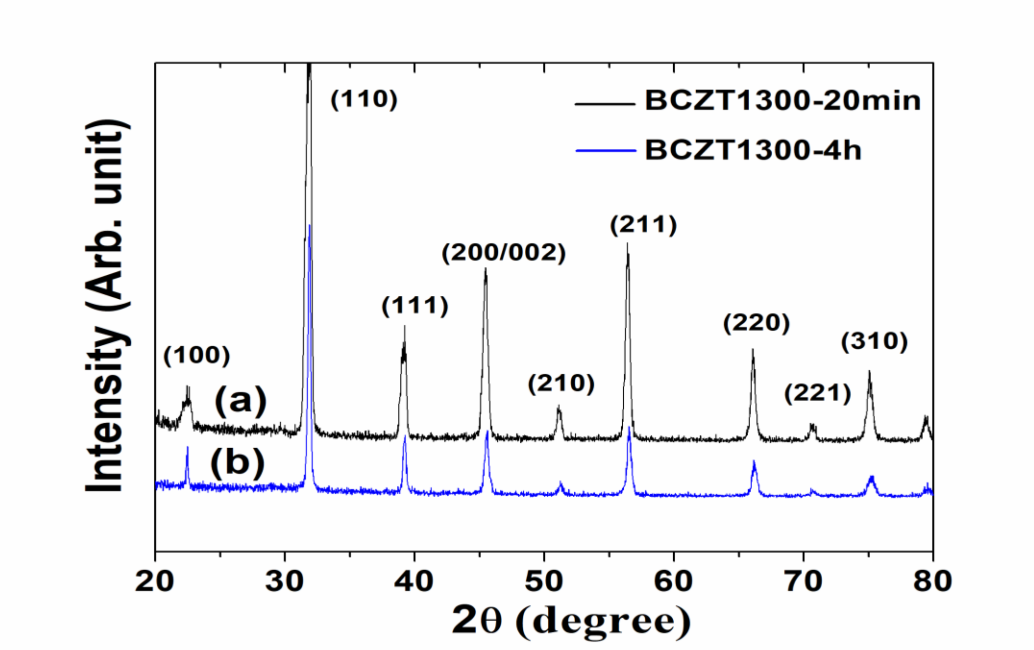

Fig. 4.2 Powder-XRD patterns of the sintered ceramics (a) BCZT1300-20min and (b) BCZT1300-4h.

SEM images of the fractured surface of BCZT1300-20min and BCZT1300-4h were recorded and the results have been shown in Fig. 4.3. From the images it is observed that grain size of the microwave sintered sample (1 to 2.5 micron) is much smaller than the conventional furnace sintered sample (5 to 20 micron). Lower grain size in the microwave sintered sample is also evident from the broader powder-XRD peaks of the same. Moreover, the size distribution of the later is broader than that of the former. This is understandable considering the substantial difference in sintering time duration of the two sintering methods. The SEM image of the sample BCZT1300-4h reveals the presence of both the 90^{o} and 180^{o} domains (Fig. 4.3 (b)). S marked domains consists of stripes indicate the formation of 90^{o} domains [5, 6]. The formation of 90^{o} domains is considered to be associated with the release of stress in the $BaTiO_3$ based ceramics when cooled from a high temperature to below T_C. The image also shows W marked 180^{o} domains which usually exist in coarse grain $BaTiO_3$ based ceramics [7, 8]. It is to be noted from the image that width of the S marked domains increases with the increase of BCZT grain size. The similar phenomena were also observed by Y. Tan et al. [8] in the sintered $BaTiO_3$ ceramics. However, these types of domain patterns are not observed in the SEM image of the microwave sintered sample (Fig.4.3 (a)).

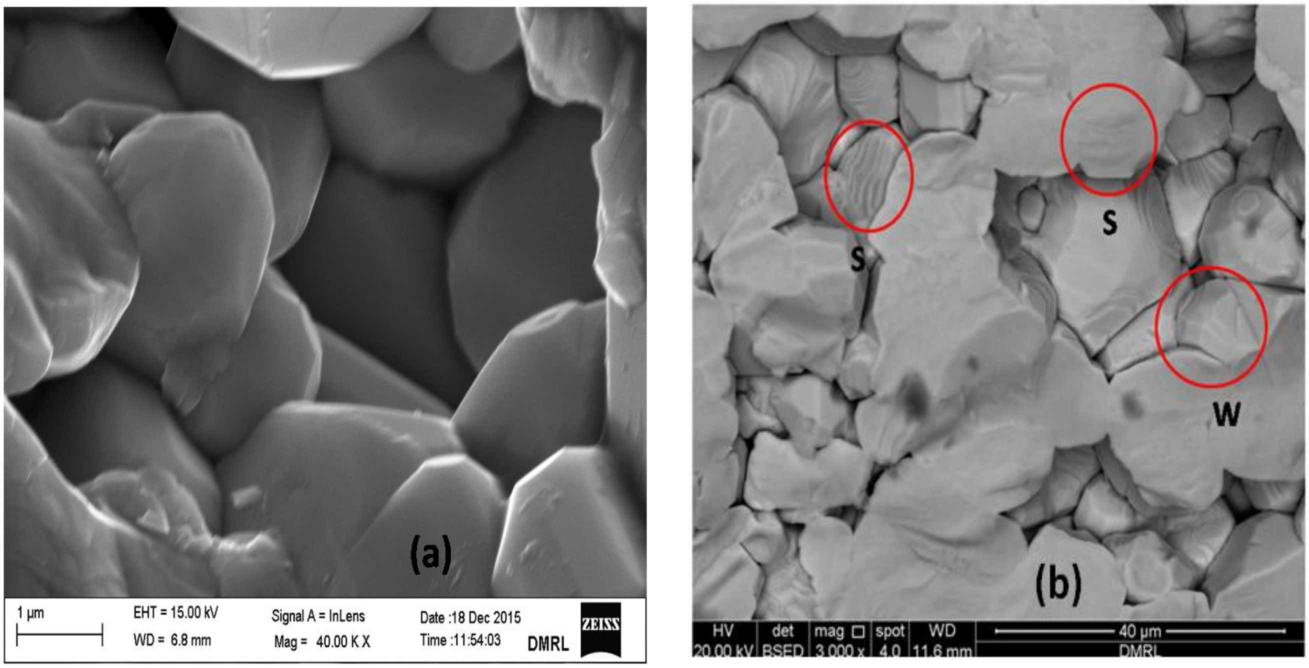

Fig. 4.3 SEM image of the fractured surface of (a) BCZT1300-20min and (b) BCZT1300-4h ceramics.

4.3.2 Dielectric property characterization

Fig. 4.4 shows the variation of dielectric constant (ε_r) and dielectric loss (tan δ) with temperature. In both the BCZT ceramic samples, ε_r increases with the increase of temperature and reaches maximum ($\varepsilon_{r\ m}$) at a particular temperature, known as Curie point. The ε_r-temperature curves of the BCZT ceramic samples display two transitions, one for the rhombohedral–tetragonal phase transition (T_s) and another at T_C corresponding to the tetragonal-cubic ($T_{C–T}$) transition. It is observed from the ε_r-temperature curves that T_C for the conventional furnace sintered sample is ~95 °C and the same for the microwave sintered sample is 115 °C i.e. 20 °C higher than the former. The occurrence of T_C at higher temperature for microwave sintered sample could be attributed to the presence of finer grains in that sample (Fig.4.3 (a)). The dense ceramics with finer grains are more likely to release internal stress by grain-boundary sliding than that having coarse grains. T_C increases with the decrease in internal stress in ferroelectric materials as its free energy decreases [9]. Thus, the dense ceramics with fine grains should have higher T_C than those of the coarse grains. This suggests that microwave sintering is an effective way to increase the T_C of BCZT ceramics. It is well known that BCZT at its optimized composition ($0.5Ba(Zr_{0.2}Ti_{0.8})O_3$-$0.5(Ba_{0.7}Ca_{0.3})TiO_3$) shows low T_C which restricts many of its applications [2]. Moreover, microwave sintered sample shows higher dielectric constant (2920), and lower dielectric loss (0.02) compared to the conventionally sintered sample for which the measured dielectric constant and dielectric loss at room temperature are 1813 and 0.035 respectively. Hence it can be concluded that microwave sintering is a useful technique to increase the density of the BCZT ceramics and to obtain finer grains in the sintered ceramics which in turn results higher T_C, enhanced dielectric constant and minimized dielectric loss.

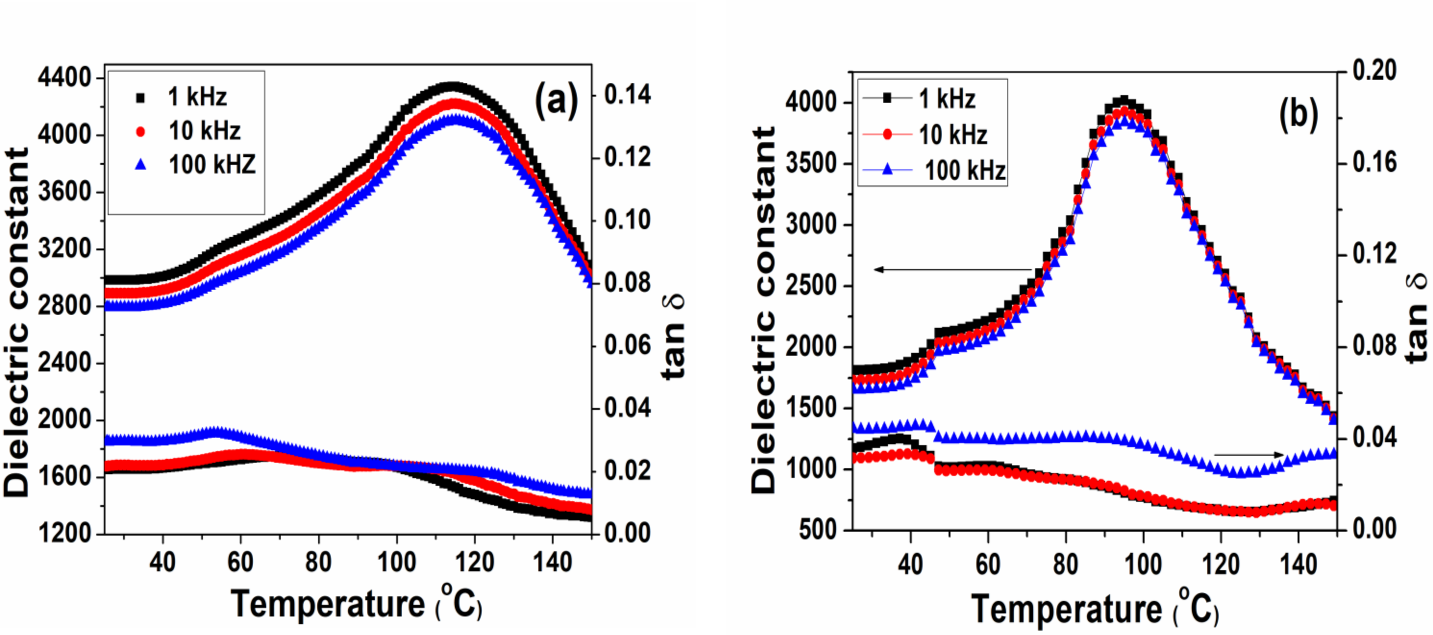

Fig. 4.4 Temperature dependant dielectric constant and dielectric loss curves for (a) BCZT1300-20min and (b) BCZT1300-4h.

The diffuseness in phase transition for both the BCZT sintered samples was measured following the method developed by Uchino and Nomura [10]. The values of γ (Diffusivity coefficient) for the microwave sintered sample are 2.06, 1.93 and 2.01 at 1 kHz, 10 kHz and 100 kHz frequencies, respectively indicating completely diffused phase transition. The same for the conventionally furnace sintered sample are 1.75, 1.77 and 1.77 respectively. The value of γ between 1 and 2 indicates the partial diffused phase transition [11]. Diffusivity coefficient of ~2 indicates diffused phase transition for microwave sintered ceramics [10]. In classical ferroelectric materials ferroelectric phase is changed to paraelectric phase at higher temperatures. The phase transition temperature is called as Curie point (T_C). Phase transition in classical ferroelectric material is characterized by a sharp change of structure and properties at the T_C. However, ferroelectric materials with diffused phase transition and relaxor ferroelectric materials were known for a broad dielectric constant maxima temperature (T_m) with frequency dispersion on the lower side of T_m and the merger of frequency dispersion above T_m. Therefore, the term dielectric maxima temperature (T_m) is more suitable rather than Curie point (T_C) to describe diffused phase transition in microwave sintered BCZT ceramics [12, 13]. Dielectric properties of sintered BCZT ceramics are given in table 4.1.

Table 4.1 Dielectric properties of the BCZT ceramics.

Sample	**ε_r (25 °C) at 1 kHz**	**$\varepsilon_{r\,m}$ at 1 kHz**	**Loss (25 °C) at 1 kHz**	**T_m (°C)**	**γ at 1 kHz**
BCZT1300-20min	2920	4340	0.02	115	2.06
BCZT1300-4h	1813	4022	0.035	95	1.75

4.3.3 Ferroelectric property characterization

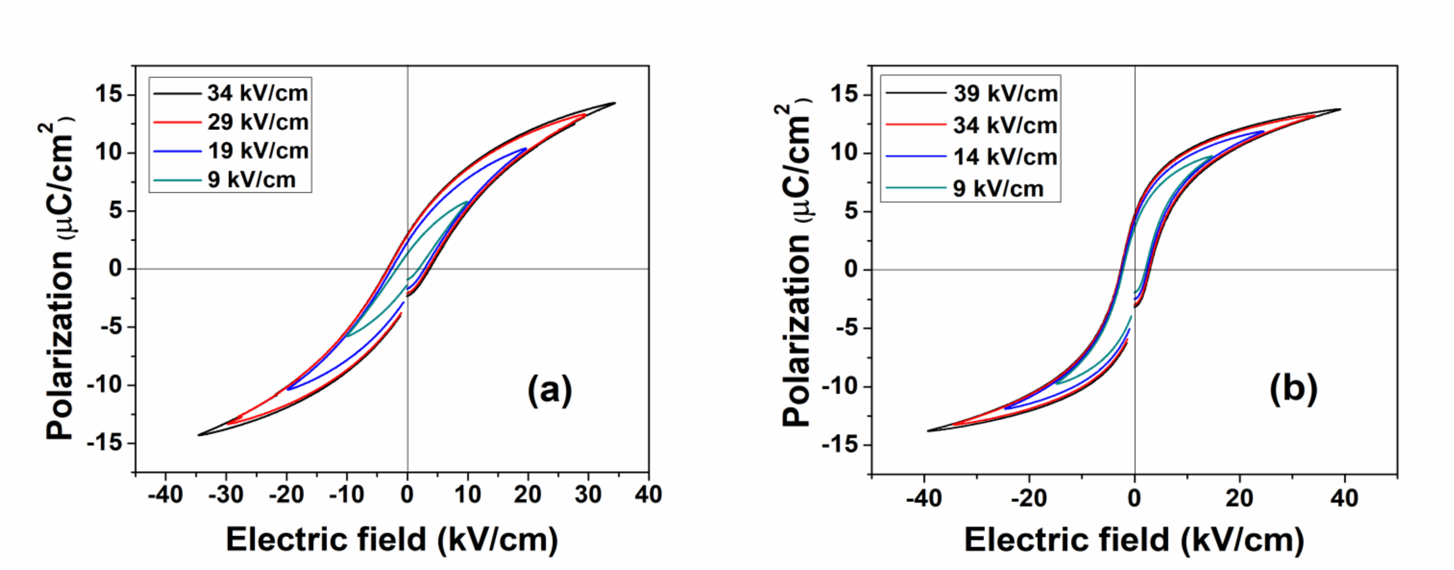

Fig. 4.5 P vs. E hysteresis loops for (a) BCZT1300-20min and (b) BCZT1300-4h ceramics.

P-E hysteresis loops for both the sintered samples are shown in Fig. 4.5. Both the loops resemble the typical P-E ferroelectric hysteresis loops. The P_{max} and P_r values for the conventional furnace sintered BCZT sample are 13.7 and 4.7 µC/cm^2 respectively, and the same for microwave sintered sample are 14.3 and 2.9 µC/cm^2 respectively. The P_r of the microwave sintered sample is lower because of the presence of fine grains. Coercive fields (E_c) for microwave and conventional furnace sintered BCZT ceramics are 3.6 kV/cm and 2.9 kV/cm respectively. Coercive field of microwave sintered BCZT is higher due to the lower grain size than that of conventional furnace sintered ceramics.

Table 4.2 Ferroelectric and energy storage properties of the BCZT ceramics.

Sample	P_{max} (µC/cm^2)	P_r (µC/cm^2)	E_c (kV/cm)	ESD (J/cm^3)	ESF (%)
BCZT1300-20min	14.3	2.9	3.6	0.13	61
BCZT1300-4h	13.7	4.7	2.9	0.09	52

Ferroelectric ceramics can be used for energy storage applications. High ESD and ESF having ceramics are desired for energy storage. The ESD and ESF of a ferroelectric material were derived from the polarization-electric field (P-E) loops as discussed in the section 1.7. The calculated ESD for BCZT1300-20min is 0.13 J/cm^3 at 34 kV/cm electric field and the same for BCZT1300-4h is 0.09 J/cm^3 at 39 kV/cm electric field. BCZT1300-20min showed the ESF of 61% whereas the BCZT1300-4h showed the ESF of 52%. Higher ESD and ESF for the microwave sintered BCZT ceramics are due to the low remanent polarization. ESF of microwave and conventional furnace sintered BCZT ceramics are comparable with the ESF of BCT ceramics [14]. Ferroelectric and energy storage properties of the BCZT ceramics are shown in table 4.2.

4.4 Conclusions

Single Phase polycrystalline BCZT ceramics were obtained at 900 ^{o}C from chemically synthesized powders. 95.2% of the BCZT theoretical density in the sintered pellets was achieved by microwave sintering at 1300 ^{o}C for 20 minutes in air. The obtained density is comparable to the maximum reported density of 95% which could be achieved by conventional furnace sintering at ~1500 ^{o}C for 2 hours in air. Microwave sintered BCZT ceramics showed higher energy storage density (0.13 J/cm^3) than that of conventional sintered ceramics. Microwave sintering has been proven to be a useful technique to obtain highly dense BCZT ceramics with finer grains which ensured higher T_m, enhanced dielectric constant, and minimized dielectric loss.

4.5 References

1. M. Oghbaei, O. Mirzaee, J. Alloys Compd., **494** (2010) 175-189.
2. H. Bao, C. Zhou, D. Xue, J. Gao, X. Ren, J. Phys. D: Appl. Phys., **43** (2010) 465401.
3. Ajeet Kumar, K. C. James Raju, A. R. James, Joint IEEE International ISAF/ECAPD/PFM (2016) doi: 10.1109/ISAF.2016.7578073.
4. K. Castkova, K. Maca, J. Cihlar, H. Hughes, A. Matousek, P. Tofel, Y. Bai, T. W. Button, J. Am. Ceram. Soc., **98 [8]** (2015) 2373-2380.
5. G. Arlt, P. Sasko, J. Appl. Phys., **51** (1980) 4956–4960.
6. G. Arlt, J. Mater. Sci., **25** (1990) 2655–2666.
7. P. Zheng, J. L. Zhang, Y. Q. Tan, C. L. Wang, Acta Mater., **60** (2012) 5022–5030.

8. Y. Tan, J. Zhang, Y. Wu, C. Wang, V. Koval, B. Shi, H. Ye, R. McKinnon, G. Viola, H. Yan, Sci. Reports., **5** (2015) 9953.
9. T. Hiroshima, K. Tanaka, T. Kimura, J. Am. Ceram. Soc., **79 [12]** (1996) 3235-42.
10. K. Uchino, S. Nomura, Ferroelectrics., **44** (1982) 55-61.
11. S. Roy, R. Maharana, S. Rangaswamy Reddy, S. Singh, P. Kumar, T. Karthik, S. Asthana, V. V. Bhanu Prasad, S. V. Kamat, Mater. Res. Express., **3 [3]** (2016) 035702.
12. A. A. Bokov, Ferroelectrics., **131** (1992) 49-55,
13. I. Rivera, A. Kumar, N. Ortega, R. S. Katiyar, S. Lushnikov, Solid State Commun., **149** (2009) 172-176
14. P. V. Sreenivas, D. K. Pradhan, B. C. Riggs, D. B. Chrisey, R. S. Katiyar, J. Alloys Compd., **584** (2014) 369-373.

Chapter 5

Synthesis, crystal structure, microstructure and electrical properties of BCZT films grown in air, in 200 nm thickness range

This chapter presents the crystal structure, microstructure, ferroelectric and piezoelectric property investigations on the air-processed BCZT thin films.

5.1 Introduction

MEMs based on ferroelectric thin films have been commercially extremely attractive due to their availability in wide ranges, high energy density, accuracy and low power requirements. Lead based piezoelectric thin films were exploited extensively for MEMS applications due to their high piezoelectric and electromechanical coupling coefficients, and were widely used in sensing and actuating applications [1, 2]. However, the restriction on the usage of lead based ferroelectric materials led to the invention of high piezoelectric lead free $Ba_{0.85}Ca_{0.15}Ti_{0.9}Zr_{0.1}O_3$ (BCZT) system as in the form of bulk ceramics and thin films [3]. Although there are some reports on BCZT thin films up to now [4-6], reports revealing the excellent dielectric, ferroelectric and piezoelectric properties of BCZT films is scarce. Moreover, from the literature it is observed that except W. L. Li et al. [4], almost all the communications made so far on BCZT thin films having thickness range $\geq$ 400 nm.

Integration of piezoelectric films of higher thickness ($\geq$ 500 nm) in the low voltage MEMS induces issues that may be shorted out by scaling down the thickness of the films. Usually physical deposition methods such as sputtering, PLD had been used to develop ferroelectric films. However, these methods are extremely expensive and become practically ineffective when larger areas are required to be deposited. Sol-gel spin coating technique offers the fine control on stoichiometry, composition and homogeneity. Lowering of crystallization temperature, larger surface covering and cost-effectiveness are the additional advantages over the physical deposition methods [2].

Lead free ferroelectric BCZT films were developed by simple sol-gel methodology without any seed layer. The 200 nm BCZT film developed by sol-gel technique is able to show excellent ferroelectric and piezoelectric properties. Moreover, the dielectric constant and dielectric tunability of these films are comparable to the best reports available so far in the literature.

5.2 Experimental methods

BCZT thin films were fabricated on Si/SiO_2/TiO_2/Pt (100) substrates using sol-gel spin coating technique. Thickness of platinum, TiO_2 and SiO_2 layers is 200 nm, 40 nm and 500 nm respectively. BCZT precursor sol making and coating on the platinum coated silicon substrates were performed as discussed in section 2.5.1. However, the possible chemical reactions in the PVP modified BCZT sol is given below.

BCZT sol-gel chemical reactions

Stage-I

Chemical reactions in Ti and Zr alkoxides precursor sol stabilized by acetyl acetone

The reactions of Ti and Zr alkoxides ($M(OR)_4$), (M=Ti/Zr) with acetyl acetonate (Acac=$C_5H_7O_2^-$) ligands are already reported in the literature [7-10]. It was revealed that Acac, being a strong ligand form chelate complex with the transition metals in which OR groups are partially or fully substituted by Acac. The extent of substitution depends on the amounts of acetylacetone (AcacH) (alkoxide-AcacH molar ratio) in the solution.

$$M(OR)_4 + AcacH \rightarrow (M(OR)_{4-x}(Acac)_x) + xROH$$

Stage -II Mixed precursor solution of acetyl acetone - stabilized Ti and Zr alkoxide is added to the mixed solution of Ba and Ca in acetic acid.

The mixed colloidal BCZT sol contains of Ba^{2+}, Ca^{2+}, $Ti\ (O\ {}^{i}Pr)_{4-x}(Acac)_x$ and $Zr(O\ {}^{n}Pr)_{4-x}(Acac)_x$ species in organic solvent (Ti-precursor is Ti iso-propoxide and Zr-precursor is Zr n-propoxide dissolved in n- propanol).

Stage -III

Drying of the spin coated BCZT sol on the substrate results solvent removal from the sol leading to BCZT gel. It is well known that chemical reactions in metal alkoxide sol-gel process involve hydrolysis and condensation reaction of the Ti and Zr- chelate complexes in presence of alcohol and water resulting 3-dimensional polymeric -M-O-M- network (M= Ti/Zr) in the final mixed metal alkoxide gel (Fig 5.1) [10].

The role of PVP in chemical sol

PVP being a strong ligand interacts intimately with the Zr and Ti complex species using its electron donating sites [11]. Moreover, steric hindrance of the polymer chains of PVP provides protective envelope over the Zr and Ti complex species which prevents their agglomeration (Fig. 5.1) and thus addition of PVP and insufficient quantity of hydrolyzing reactant (water) ensures controlled hydrolysis avoiding the formation of viscous gel or precipitate. It is to be mentioned that addition of small amount of water and PVP to the sol before spin coating also helps in obtaining thin films with minimized defects e.g. cracks, micro pores and macro pores etc.

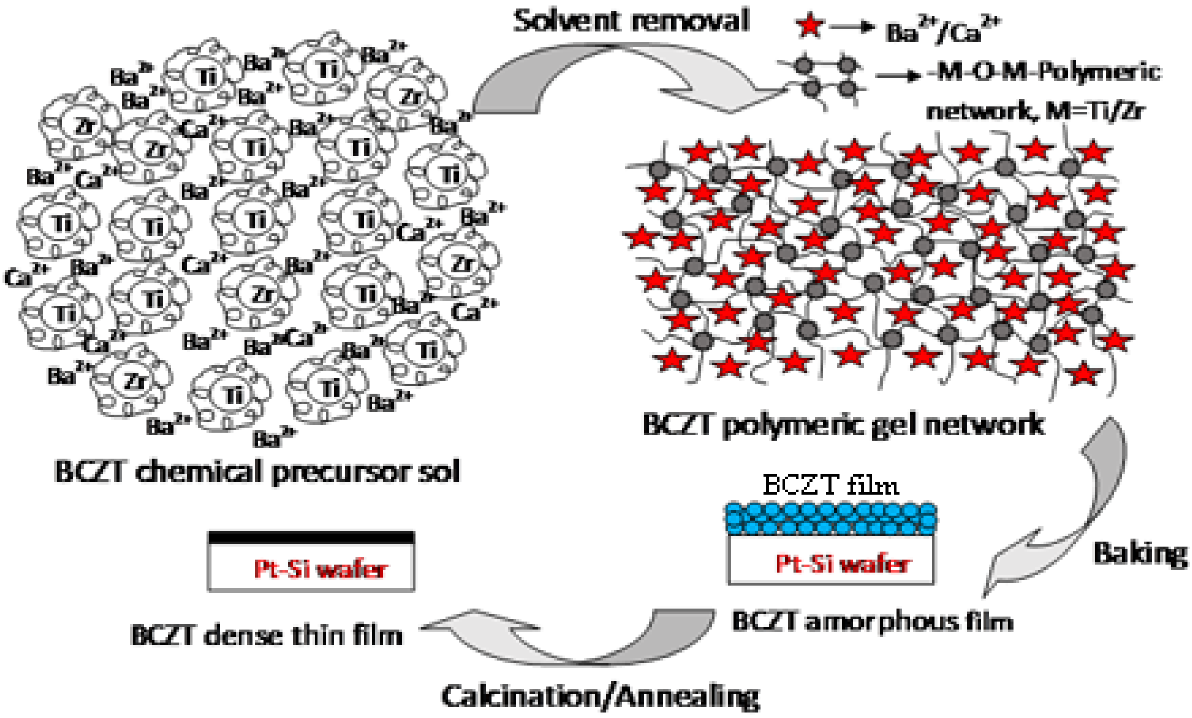

Fig. 5.1 Schematic diagram for the chemical processing of BCZT thin film from the chemical precursor sol.

The coated BCZT films were dried on hot plate at ~150 ^{o}C for solvent evaporation followed by calcination at 500 ^{o}C in a tubular furnace for decomposition of organic moieties present in the films. The spin coating, drying and calcination cycles were performed three times to obtain the desired thickness of around 200 nm. Then the films were annealed using conventional tubular furnace at 700 and 800 ^{o}C temperatures for an hour with heating rate of 2 ^{o} C/min in air. Finally the films were heat treated in rapid thermal annealing (RTA) furnace in oxygen atmosphere at those temperatures with the heating rate of 50 ^{o}C/sec for 4 minutes with the aim to reduce oxygen vacancies and leakage current density. It was reported earlier that RTA for even a very short duration (30 sec) in presence of oxygen gas decreased the leakage current density in metal oxide thin film [12]. Phase and crystal structure of the annealed BCZT films were analyzed by GIXRD technique. A grazing angle of 0.5^{o} and chromium kα radiation was used in order to avoid Pt and Si peaks from the underlying substrate and to obtain appropriate separation of the phase peaks. XRD peak decomposition was performed by XRFIT software (as incorporated in Full proof Rietveld Suite) using Marquardt type least square fitting technique. HRTEM was used to study the microstructure of the BCZT films. Capacitance-electric field butterfly loops, dielectric loss, and ferroelectric hysteresis loops of the films were measured with the application of DC voltage sweep using SCS-4200 system. Leakage current behavior of the films was also studied using the same system. Surface topography, local polarization switching and piezoelectric response of the BCZT films was analyzed by PFM. Crystal structure, microstructure and electrical properties of the annealed films were analyzed at room temperature. For measurements of electrical properties gold dots (diameter: 250 µm) were sputtered on the annealed films as top electrodes and on ~2 cm x 2 cm film coated on Si/Pt (100) substrate there were hundreds of sputtered gold dots. Each gold dot along with Pt bottom electrode and BCZT thin film in-between, worked as a ferroelectric capacitor during dielectric and ferroelectric property measurements. We observed some variations, when the properties were measured on different capacitors. The graphs in the figures, included in ‘results and discussion’ portion, represent the results obtained from the best ferroelectric capacitors; however, errors bar applied on each quoted data reflect the variations in properties measured on different capacitors.

5.3 Results and discussion

5.3.1 Structure and microstructure characterization

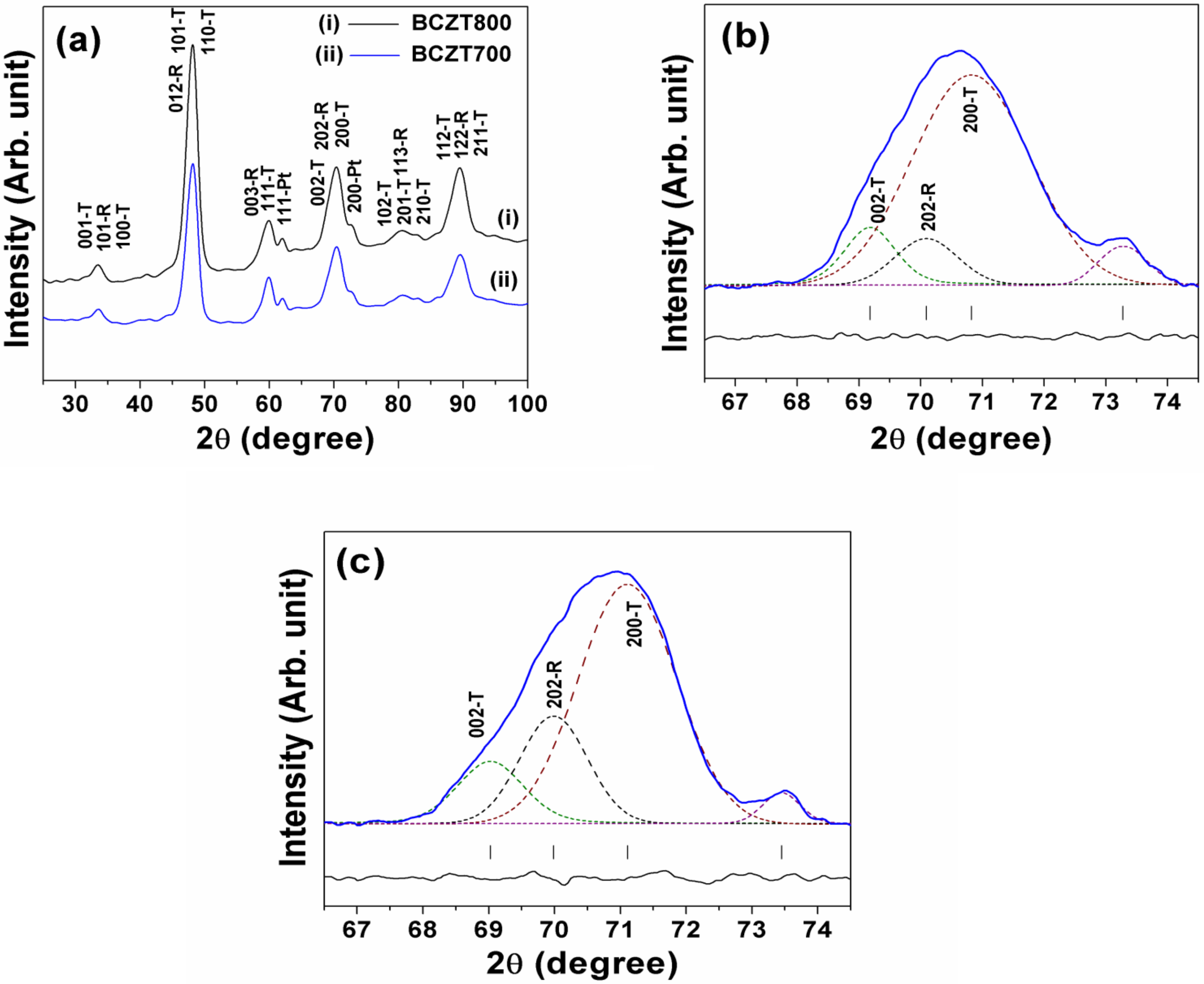

Fig. 5.2 (a) GIXRD patterns of BCZT films annealed at 700 and 800 ^{o}C temperatures, (b) decomposed tetragonal and rhombohedral BCZT peaks in the films annealed at 700 ^{o}C and (c) 800 ^{o}C temperatures.

GIXRD patterns of BCZT films annealed at 700 and 800 ^{o}C temperatures (abbreviated as BCZT700 and BCZT800) are presented in Fig. 5.2 (a). Since chromium kα radiation wavelength is higher when compared to that of copper kα radiation, peak spacing increases slightly, making it possible to separate the tetragonal and rhombohedral peaks. X-ray diffraction patterns of the films demonstrate that the occurrence of pure polycrystalline BCZT with tetragonal (*P4mm*) structure as the major fraction while rhombohedral (*R3m*) BCZT is also present in minor fraction. On relative terms higher fraction of rhombohedral phase is evident in the high temperature annealed film (Fig. 5.2(b)-(c)). Intensity ratio of $I_{002\text{-}T}/I_{202\text{-}R}$ is 1.16 and 0.74 for BCZT700 and BCZT800 respectively. Since the BCZT film thickness was only about few tens of nm, underlying Pt peaks are also evident in Fig. 5.2 (a)-(c). These results indicate that Ca^{+2} and Zr^{+4} ions diffused into the $BaTiO_3$ lattices to form a homogeneous solid solution. W. Liu et al. [3] have earlier reported that the rhombohedral and tetragonal phases coexist in the BCZT composition at room temperature as their bulk counterparts and it is usually indicated by the splitting of (200) peak.

TEM image of the film cross section shows the thickness of film is ~200 nm (Fig. 5.3 (a)). The d-values calculated from the electron diffraction pattern (Fig. 5.3 (b)) for the (100), (110), (111), (200) and (211) planes are matching the same calculated from the GIXRD patterns. HRTEM image (Fig. 5.3 (c)) of three neighboring grains shows lattice spacing of the (110) (111) and (200) planes. A common problem which is usually encountered in the development of ferroelectric films is the diffusion of the constituent elements through the interface during annealing of the film at high temperatures [13]. The Fig. 5.3 (d) represents the TEM-EDS mapping images for the elements Ca and Zr of the cross-sectioned BCZT 800 film. The film area shows the presence of Ca and Zr. TEM-EDS mapping analyses showed (although only Ca and

Zr are shown in the figure) that neither Pt nor Si could be found within the BCZT film thickness and none of the BCZT elements were found within the Pt electrode or SiO_2 layer. Thus, none of the constituent elements of BCZT or, Pt from bottom electrode showed any sign of diffusion across the film-electrode interface.

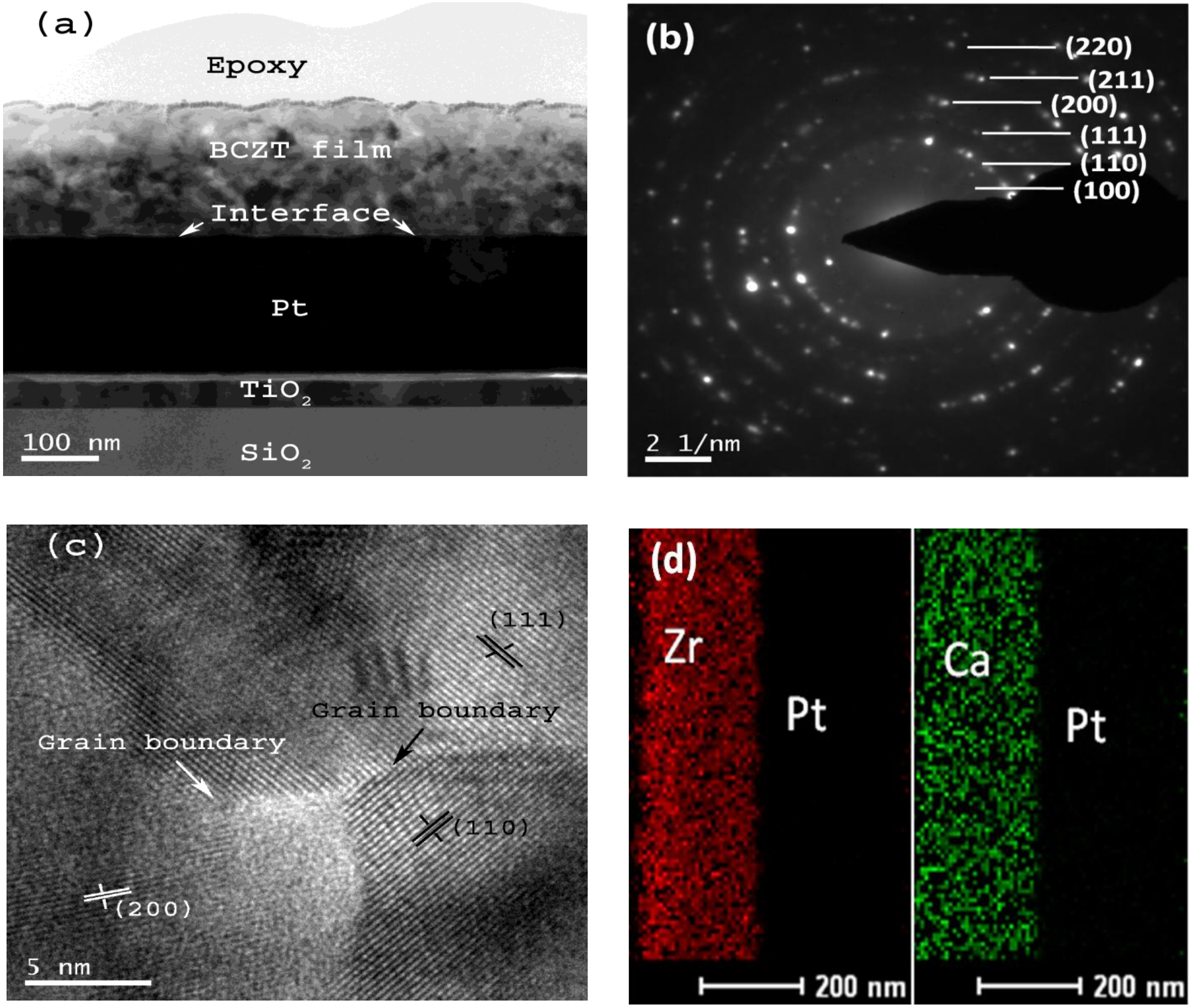

Fig. 5.3 (a) TEM image of the film cross section, (b) Electron diffraction pattern image, (c) HRTEM image showing the (110), (111) and (200) planes of three neighboring BCZT grains and (d) TEM-EDS elements mapping for Zr, Ca and Pt at BCZT film-substrate interface.

5.3.2 Dielectric property characterization

Fig. 5.4 (a)-(b) represents the variation of capacitance and dielectric loss with DC electric field at 10 kHz and 100 kHz frequencies. Capacitance decreased and dielectric loss increased with increasing the frequency. The maximum capacitance values at 10 kHz frequency for BCZT700 and BCZT800 films are 2.1±0.15 nF and 2.9±0.15 nF respectively and the same at 100 kHz frequency for BCZT700 and BCZT800 films are 1.8±0.15 nF and 2.4 ±0.15 nF respectively (Fig. 5.4 (a) and (b)). The error bars indicate standard deviations from measurements on different capacitors. Dielectric loss of the BCZT700 film at 10 kHz frequency varied from 0.055 to 0.061 and the same for BCZT700 film at 100 kHz frequency varied from 0.067 to 0.077 (Fig. 5.4 (a)). Magnitude and variation of dielectric loss with electric field at 10 kHz and 100 kHz frequency for BCZT800 film were similar to that of the BCZT700 film (Fig. 5.4 (b)). The measured dielectric loss on BCZT700 and BCZT800 films are comparable with the dielectric loss reported for the sol-gel derived BCZT films [14]. The higher capacitance of the BCZT films annealed at 800 ^{o}C temperatures is due to the dense microstructure of the films. Butterfly-shaped capacitance-electric field (C-E) loops of the BCZT films are caused by switching of the ferroelectric domains and indicate that the films are ferroelectric in nature. The nonlinearity of capacitance or dielectric constant with DC electric field results from the anharmonic interaction of Ti ions in the perovskite cubic structure. The anharmonic interaction can be visualized as an inelastic feature of the bonding between Ti^{+4} and O^{-2} ions. Nonlinearity of dielectric constant and loss with respect to DC electric field was explained by Johnson's theory which is represented as follows (Equations 5.1 and 5.2),

$$\frac{\varepsilon_r(V_{App})}{\varepsilon_r(0)} = \frac{1}{(1+\alpha\varepsilon_r^3(0)\, E^2)^{1/3}} \tag{5.1}$$

$$\frac{tan\,\delta(V_{App})}{\tan\delta_0} = \frac{1}{(1+\alpha\tan\delta_0^{j}E^2)^{1/3}} \tag{5.2}$$

where $\varepsilon_r(0)$ and $\varepsilon_r(V_{App})$ are the dielectric constant at zero electric field and at applied electric field E, respectively, α is the anharmonic coefficient, and tan δ_0 and tan $\delta(V_{App})$ are the dielectric loss at zero electric field and at applied electric field E. Johnson's model clearly shows that dielectric constant and loss of the thin film decreases with increasing electric field [15]. Therefore, the decrease in capacitance and dielectric loss with applied electric field for BCZT films is due to anharmonic interaction of titanium ions in perovskite structure. However, butterfly curves for BCZT700 film are minutely shifted from the zero bias. This could be attributed to the generation of oxygen non-stoichiometry in the film during annealing which led to the shift of C-E loop on the electric field axis [16]. BCZT800 film is expected to have lower oxygen vacancy than BCZT700 film. It was reported earlier that in metal oxide thin film oxygen vacancy decreased with increasing annealing temperature [17]. However, some researchers attributed the same to the presence of internal space charge field due to charge trapping at the electrode-film interface which can be enhanced by oxygen vacancy associated defect dipole [18]. The values of dielectric constant were calculated from the corresponding capacitance values. Dielectric constants (ε_r) of 1120±50 and 1550±50 were obtained at 10 kHz frequency for the BCZT700 and BCZT800 films. The error bars in Fig. 5.4 indicate standard deviations from capacitance measurements on different capacitors and associated inaccuracy in thickness measurements by cross section TEM.

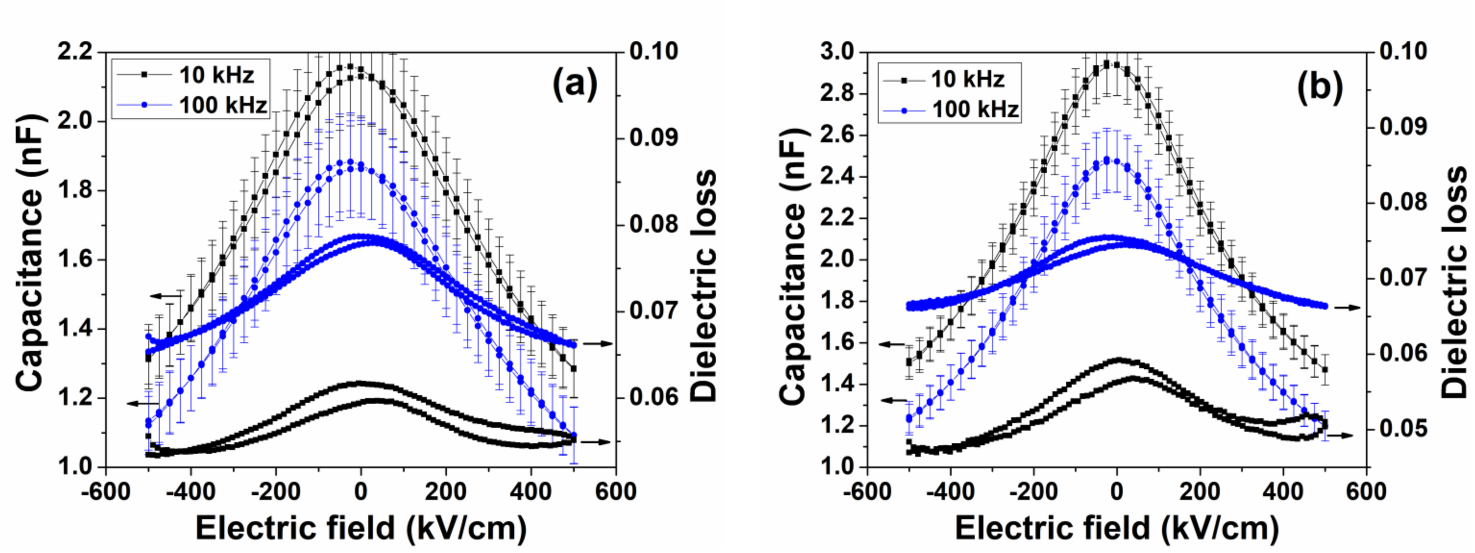

Fig. 5.4 Capacitance and dielectric loss as a function of electric field for (a) BCZT700 and (b) BCZT800 films.

The reports on the dielectric tunability of BCZT thin films are limited. In the present work, the dielectric tunability percentage is derived from the equation (5.3), where $\varepsilon_{(E0)}$ and $\varepsilon_{(E)}$ represent the dielectric constant at zero electric field and at maximum electric field, respectively [19].

$$Tunability\ (\%) = \frac{\varepsilon_{(Eo)} - \varepsilon_{(E)}}{\varepsilon_{(E0)}} \times 100 \tag{5.3}$$

The dielectric tunability of the BCZT films annealed at 700 and 800 °C temperatures are 40% and 50% respectively. These values are comparable to the reported high-end dielectric tunability values of BCZT films [6, 20] and multilayered BST films known for their high dielectric tunability [21].

5.3.3 Ferroelectric property characterization

The ferroelectric nature of the BCZT thin films annealed at 700 and 800 ^oC temperatures is confirmed by the hysteresis loops of polarization (P) as a function of applied electric field (E) (Fig. 5.5 (a) and (b)). P vs. E measurements was carried out at 10 kHz frequency. The hysteresis loops reveal that both the P_{max} and P_r increased as the electric field is increased. P_{max} and P_r for BCZT800 film measured at 1000 kV/cm electric field are 82 and 25 μC/cm^2 respectively, and for the BCZT700 film P_{max} and P_r measured at 1000 kV/cm electric field are 70 and 22 μC/cm^2 respectively. The error bar for P_{max} is ±2 and the same for P_r is ±1. The error bars indicate standard deviations from measurements on different capacitors. The BCZT800 films showed higher P_{max} and higher P_r than that of the BCZT700 films. The measured P_r of BCZT films is comparable with the reported high-end values of P_r for BCZT film with similar composition [5]. The higher polarization of BCZT800 films is attributed to the dense microstructure of the films. Porosity present in the low temperature annealed films can change the bottom electrode-film interface properties including alignment of the domains at the film bottom electrode interface. Thin films with higher porosity having slower polarization reversal and thus shows comparatively lower polarization than the dense film [22]. Coercive field of a ferroelectric thin film largely depends on the thickness of the film and grain size. Coercive field (E_c) of 186 kV/cm is obtained for BCZT800 film from the P-E loop measured at 1000 kV/cm electric filed, while for the BCZT700 film 222 kV/cm E_c is obtained from the P-E loop measured at 1000 kV/cm electric field. The error bar for the measurements of coercive field is ±5. The E_c of the BCZT films are much higher than that of the bulk BCZT ceramics (1.68 kV/cm) with similar composition [3] because of clamping effect of the substrate, which is very pronounced on the thin film with very low thickness (~200 nm). BCZT thin film of lower E_c (68.06 kV/cm) was also reported; however, the BCZT film thickness involved in that measurement was 800 nm and was expected to experience much lower clamping effect [5]. The E_c decreases with increasing grain size [5, 23] and the lower E_c of BCZT800 film can be attributed to its higher grain size. The average grain size in BCZT800 thin film material is relatively higher than that in BCZT700 as the annealing temperature of the former is higher.

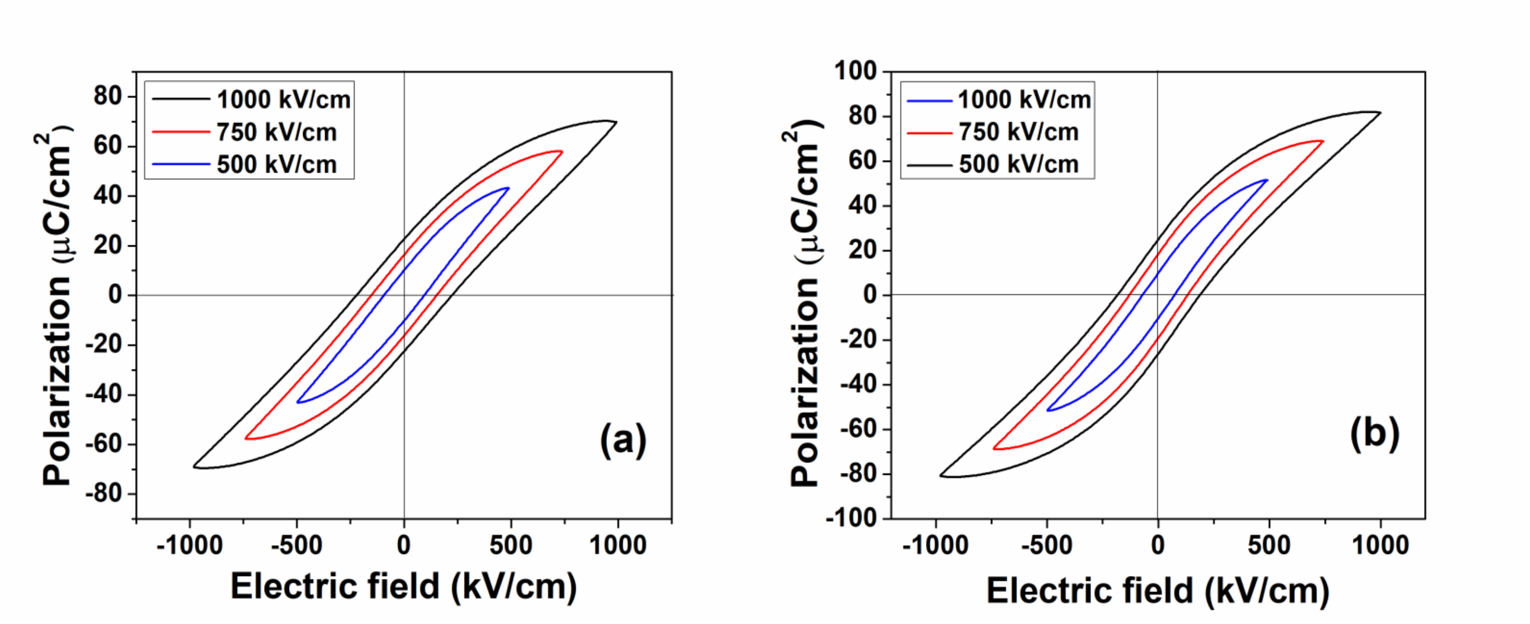

Fig. 5.5 P vs. E hysteresis loops of (a) BCZT700 and (b) BCZT800 films.

Potential of a dielectric material is usually characterized by its energy storage properties. Recoverable ESD of dielectrics can be calculated as described in the section 1.7. Earlier reports suggest that recoverable ESD of antiferroelectric [24, 25] ceramics (≤ 2.75 J/cm^3) and ferroelectric [26] ceramics (0.59 J/cm^3) are very low. However, with the advent of modern thin film technology it was confirmed that very high ESD could be achieved from ferroelectric thin films. For example, high ESD of ~18 J/cm^3 was reported for doped $PbZrO_3$ thin films [27, 28].

Integration of the discharge portions of the P-E hysteresis loops following the equation (1.7) yielded ESD of the BCZT700 and BCZT800 films. The calculated ESD value from the P-E loop measured at 1000 kV/cm electric field for BCZT700 is 15 J/cm^3 and the same calculated from the P-E loop measured at 1000 kV/cm electric field for BCZT800 is 17 J/cm^3. These values are comparable to the ESD of doped $PbZrO_3$ thin films which are known for offering high ESD [27-28]. It is to be mentioned that the obtained values of ESD for BCZT thin films are much higher than that of the BCZT bulk ceramics (0.59 J/cm^3) [26].

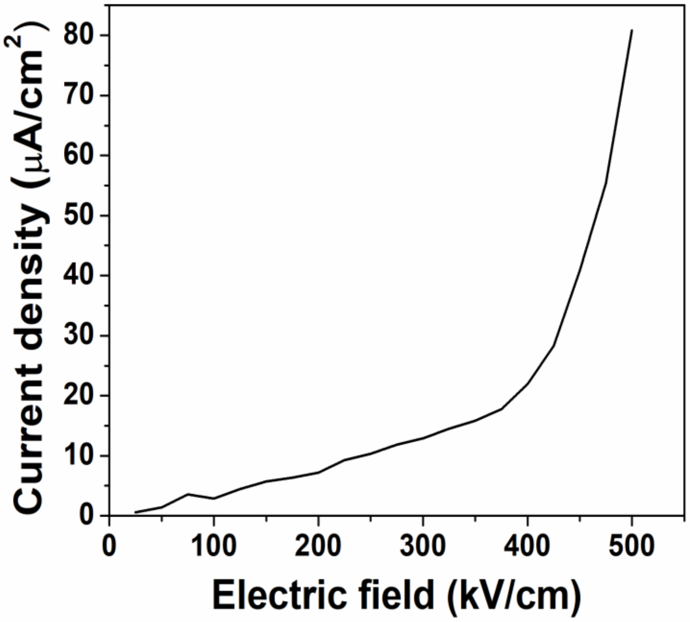

Fig. 5.6 Leakage current density variation with electric field for BCZT800 film.

It has been observed that the measured P-E hysteresis loops for the BCZT thin samples are not saturated and hence it is essential to understand the behavior of the leakage current with the electric field since leakage current of a ferroelectric thin film is a major concern for most of the thin film device applications. The leakage current can be correlated to the various defects including oxygen vacancies, trap states (acceptors and donors) present in the thin film [29]. Leakage current and leakage current density of the BCZT800 film were found to be 2.5 x 10^{-10} A and 0.6 μA/cm^2 respectively (Fig. 5.6). This level of leakage current density is comparable to the reported leakage current density of the BCZT thin film with similar composition grown on $SrTiO_3$ substrate and on Pt-Si substrate with $(Pb_{0.8}Ca_{0.2})TiO_3$ seed layer [30, 31].

5.3.4 Characterizations by piezo-response force microscopy

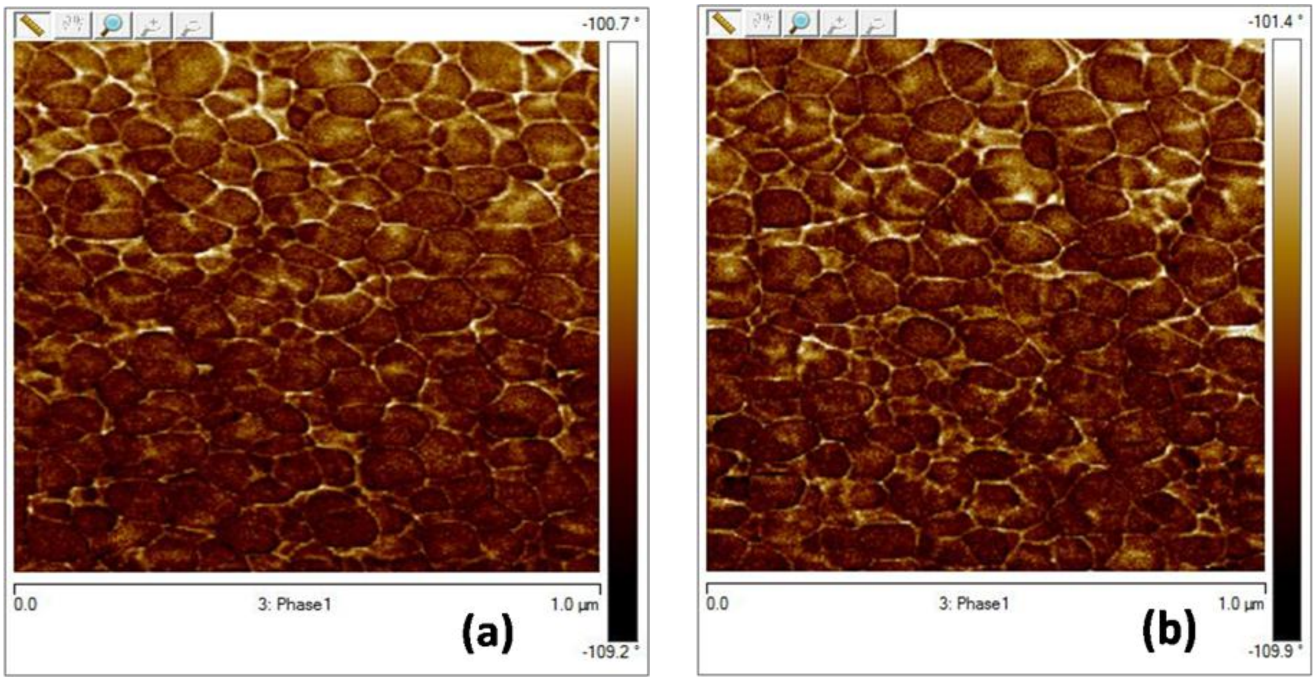

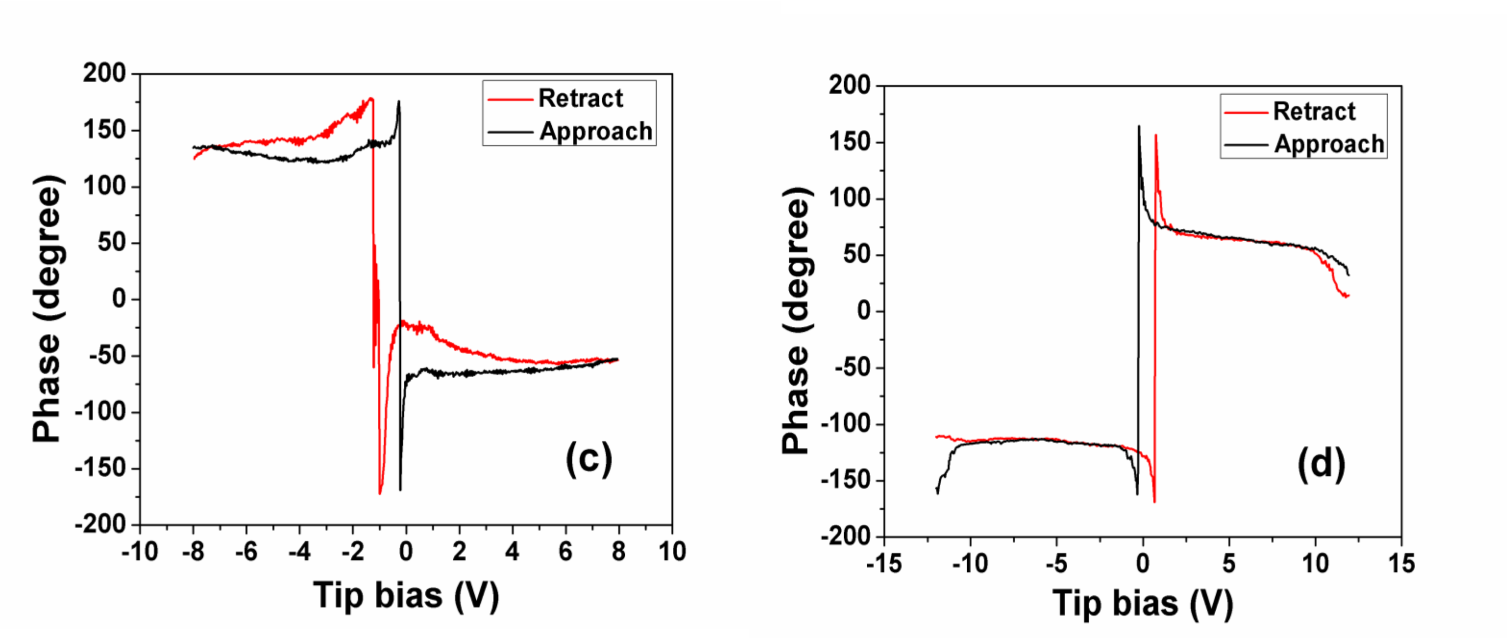

Fig. 5.7 (a) PFM phase image of BCZT700, (b) PFM phase image of BCZT800, phase vs. bias voltage hysteresis loop of (c) BCZT700 and (d) BCZT800 films.

PFM phase images of the BCZT films are shown in Fig. 5.7 (a) and (b). The phase images revealed that the size range of BCZT700 and BCZT800 thin films surface grains are: 20-100 nm and 30-130 nm respectively. PFM was employed to study the local piezoelectric response of the BCZT films. The experiments were performed with the application of DC bias voltage +12 V to -12 V on the BCZT grains of different size, located at different portion of the thin film. A conductive tip (tip diameter ~20 nm) was applied for this purpose. The grains having different grain size and neighborhood (Packing environment: closely packed or surrounded by fewer neighbors) were selected randomly on the BCZT films for PFM measurements. It can be assumed that during the application of DC bias voltage by the PFM tip to the film, the tip is taping only one grain on the surface at a time since the diameter of the tip is only 20 nm. The applied voltage stimulates the deformation in the grain due the converse piezoelectric effect. Deformation of the grain was measured as vertical deflection of the cantilever in terms of amplitude and phase as a function of bias voltage using standard lock-in amplifier technique [32]. Phase versus DC bias voltage hysteresis loops demonstrate the local domains switching behavior (Fig 5.7 (c) and (d)) [33]. The amplitude versus bias voltage (V) exhibited butterfly loops corresponding to displacement which contains information about piezoelectric deformation under applied bias voltage. It was observed that the PFM response varied widely with varying grain size. The deformation increased with increasing the grain size with the application of same electrical input. The PFM responses of the similar sized grains also varied with the packing density of the neighborhood grains associating the BCZT grain of interest. Moreover, the amplitude versus DC bias voltage butterfly curves obtained from the results of PFM measurements on both BCZT700 and BCZT800 thin films were unsymmetrical and slightly shifted from zero bias voltage. From the amplitude versus bias voltage butterfly curves, the converse piezoelectric coefficient (d_{33})-voltage loops (Fig. 5.8 and Fig. 5.9) can be determined through the following equation (5.4) (converse piezoelectric effect) [34].

$$d_{33} = \frac{D - D_I}{V - V_I} \tag{5.4}$$

In equation (5.4), D is the measured value of piezoelectric deformation, V is the applied voltage at each point on the D–V curve, D_I is the piezoelectric deformation and V_I is the applied voltage of the intersection.

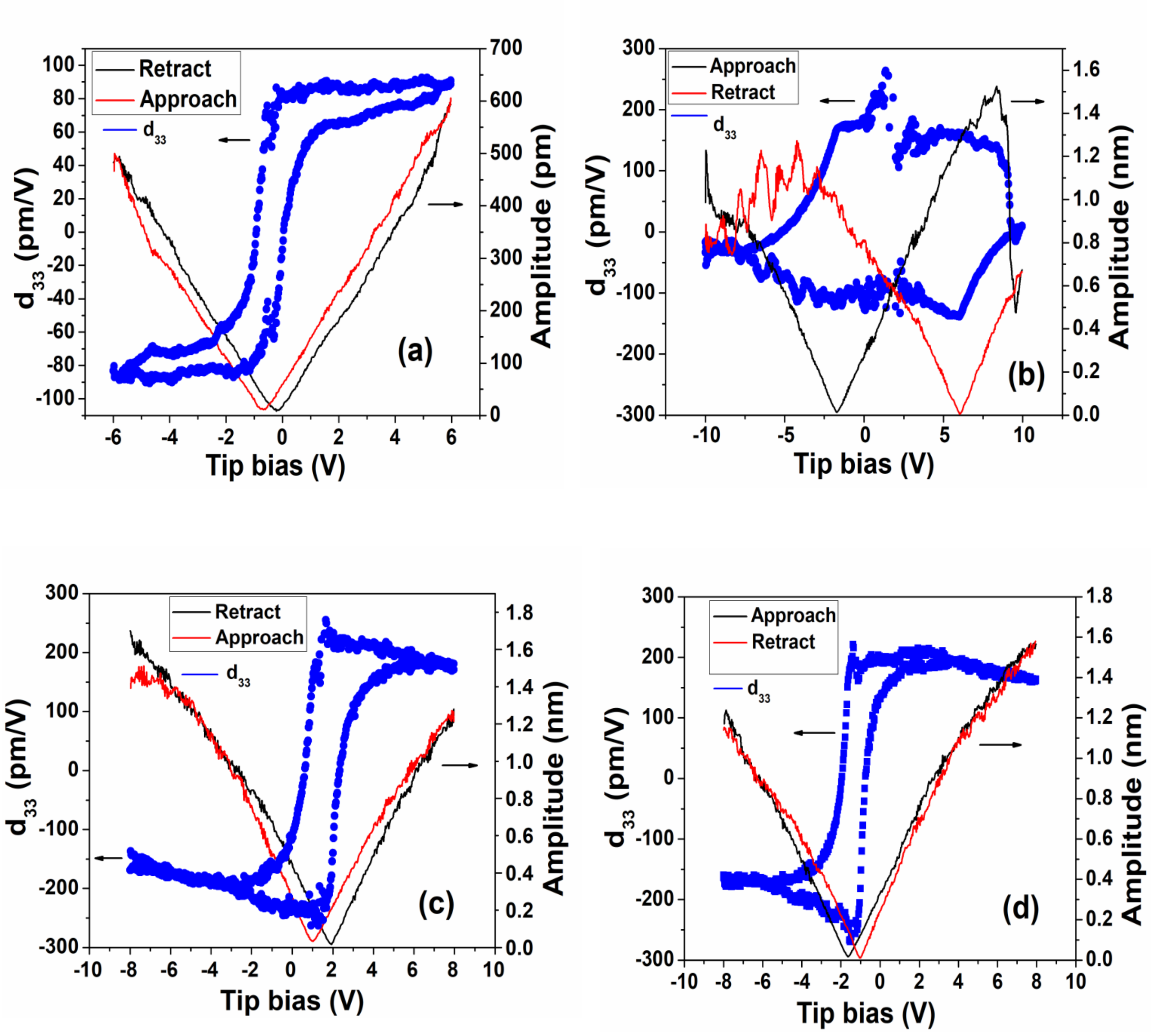

Fig. 5.8 (a)-(d) Amplitude and d_{33} vs. bias voltage loops of the BCZT grains with different size on the BCZT700 film.

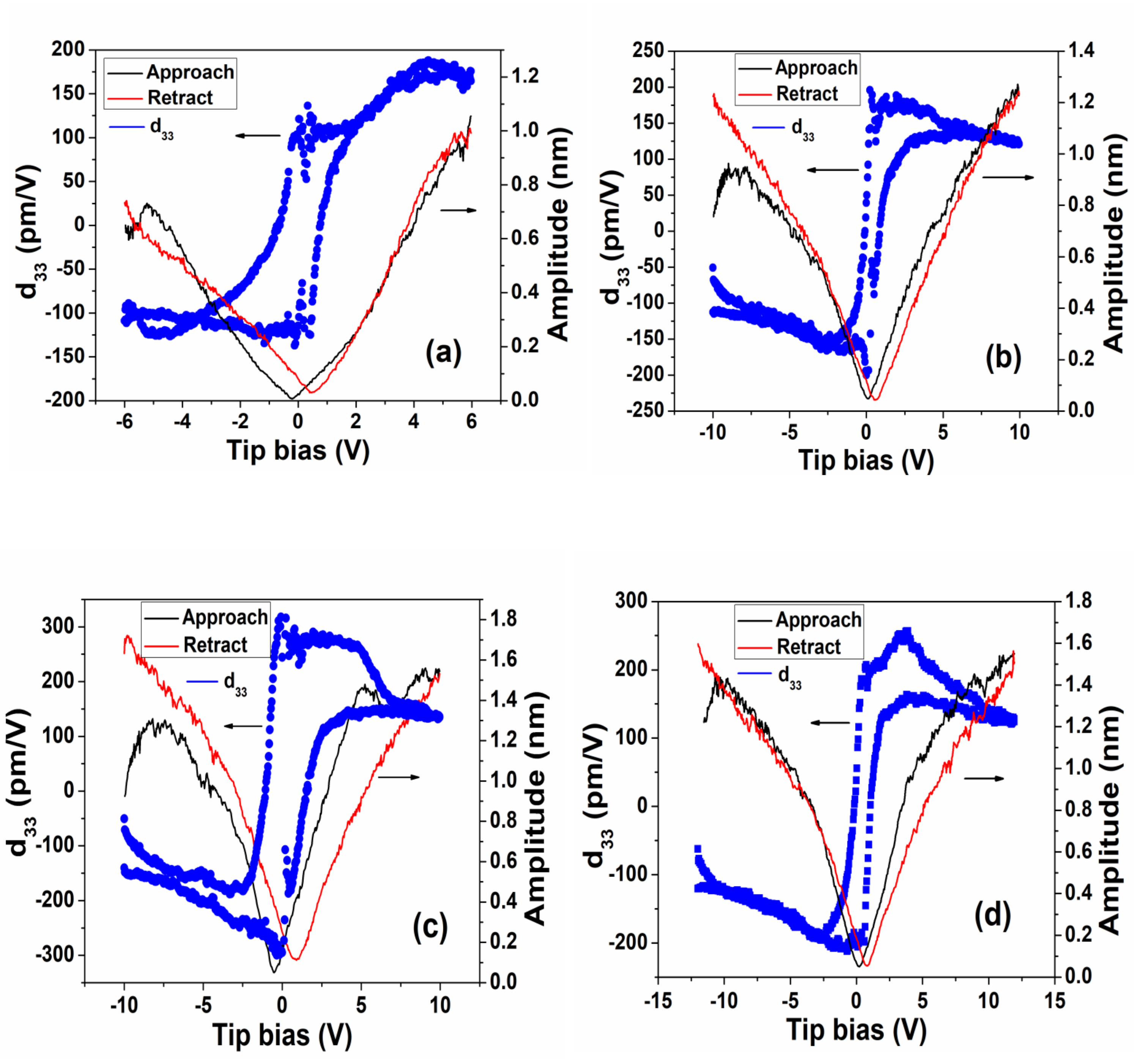

Fig. 5.9 (a)-(d) Amplitude and d_{33} vs. bias voltage loops of the BCZT grains with different size on the BCZT800 film.

The d_{33} values calculated from the results of the PFM measurements when measured randomly on different BCZT grains of different size (20 nm -100 nm) distributed on the BCZT700 film varied widely from 90 pm/V to 230 pm/V. The d_{33} values obtained for BCZT800 of different grain size (30 nm -130 nm) varied from 120 pm/V to 295 pm/V. The value of d_{33} increased with increasing grain size. The wide variation of d_{33} of the films is shown in the Fig. 5.8 and Fig. 5.9. It should be noted that different localized piezoelectric responses from piezoelectric grains having different grain size were also reported earlier [35]. Since the D-V butterfly curves were unsymmetrical, obtaining a constant d_{33} on either side of the voltage axis (+ve or –ve) was not possible, although the PFM experiments were performed using a properly calibrated PFM measurement set up. The most symmetric amplitude versus DC bias curves derived from PFM responses of larger sized BCZT grains (100-130 nm) distributed on BCZT700 and BCZT800 films showed that the converse d_{33} of 210 pm/V and 250 pm/V as indicated by the maxima of the d_{33}-voltage loops (Fig. 5.8 (d) and Fig. 5.9 (d)). Deformation of a clamped piezoelectric thin film under applied electric field is confined by the substrate and hence the resultant piezoelectric response is smaller than that of the corresponding bulk ceramics (~1140 pm/V) [3]. It is observed that the polarization, dielectric constant and converse d_{33} are increased as the annealing temperature is raised from 700 to 800 ^{o}C. The electrical properties of the BCZT films were compared with the reported literature (Table 5.1).

Table 5.1 Comparison of electrical properties of the synthesized BCZT films with reported data in literature.

	Annealing Temp.	**Thickness (nm)**	**Dielectric constant (ε_r)**	**Dielectric tunability percentage**	**Remanent polarization ($\mu C/cm^2$)**	**Converse piezoelectric coefficient (pm/V)**	**ESD (J/cm^3)**	**Ref.**
BCZT (Sol-gel technique, Manuscript data)	700 °C	200	1120±50	40	22±1	210	15	-
BCZT (Sol-gel technique, Manuscript data)	800 °C	200	1550±50	50	25±1	250	17	-
BCZT (dual magnetron sputtering)	750 °C	200	-	-	-	258	-	[4]
BCZT (Sol-gel technique)	850 °C	800	-	-	22.15	-	-	[5]
BCZT (Sol-gel technique)	700 °C	450	-	-	6.1	104	-	[31]
BCZT (PLD)	750 °C	600	1010	-	-	80	-	[16]
$Pb(Zr,Ti)O_3$	-	900	800	-	-	100	-	[36]

5.4 Conclusions

In summary, BCZT thin films of thickness ~200 nm were grown on $Si/SiO_2/TiO_2/Pt$ (100) substrates using sol-gel spin coating technique. BCZT films exhibited pure polycrystalline perovskite structure with dense microstructure. GIXRD analyses of the thin films concluded pure polycrystalline BCZT phase with tetragonal (*P4mm*) structure as the major fraction and rhombohedral (*R3m*) as the minor fraction. The polarization versus electric field loops indicated the ferroelectric nature of the films. The BCZT films annealed at 800 °C showed the higher P_r of 25±1 μC/cm^2, higher dielectric constant of 1550±50 and dielectric tunability of 50%, while the BCZT films annealed at 700 °C showed P_r of 22±1 μC/cm^2, dielectric constant of 1120±50 and dielectric tunability of 40%. Moreover, the energy storage densities estimated from the P-E loops of the BCZT films are comparable with that of the $PbZrO_3$ thin films which are known for offering high ESD. The large converse d_{33} of ~250 pm/V were obtained from the larger sized BCZT grains of grain size ~130 nm distributed over the annealed BCZT thin films. These results indicate that the BCZT films might be used as alternative to lead based thin films for ferroelectric and piezoelectric MEMS applications.

5.5 References

1. S. Trolier-McKinstry, P. Muralt, J. Electroceram., **12** (2004) 7–17.
2. G. H. Haertling, J. Am. Ceram. Soc., **82 [4]** (1999) 797–818.
3. W. Liu, X. Ren, PRL., **103** (2009) 257602.
4. W. L. Li, T. D. Zhang,Y. F. Hou, Y. Zhao, D. Xu, W. P. Cao, W. D. Fei, RSC Adv., **4** (2014) 56933-37.
5. Z. M. Wang, K. Zhao, X.-L. Guo, W. Sun, H. L. Jiang, X. Q. Han, X. T. Tao, Z. X. Cheng, H. Y. Zhao, H. Kimura, G. L. Yuan, J. Yin, Z. G. Liu, J. Mater. Chem. C., **1** (2013) 522-30.
6. W. Li, J. Hao, H. Zeng, J. Zhai, Cur. Appl. Phys., **13** (2013) 1205-08.
7. C. Sanchez, F Babonnean, S.Docuff, A.Leausin, J.D.Mackenzie, D.R Ulrich EDS, whiley, Newyork, (1988) p77.

8. A. Wu, I. M. Miranda Salvado, P. M. Vilarinho, J. L. Baptista, J. Sol-Gel Sci. Tech., **19** (2000) 671–676.
9. M. W. Jung, H. J. Oh, J. C. Yang, Y.G Shul, Bull. Korean Chem. Soc., **20** (1999) 12.
10. T. Schneller, R. Waser, M. Kosec, D. Payne, Springer, New York (2013) Doi:10.1007/978-3-211-99311-8
11. G. I. Spijksma, Henny J. M. Bouwmeester, Dave H. A. Blank, V. G. Kessler, Chem. Commun., (2004) 1874.
12. S. Ezhilvalavan, T. Y. Tseng, J. Am. Ceram. Soc., **82 [3]** 1999, 600-6.
13. L. Sagalowicz, P. Muralt, S. Hiboux, T. Maeder, K. Brooks, Z. Kighelman, Mater. Res. Soc. Symp. Proc., **596** (2000) 265-70.
14. G. Kang, K. Yao, J. Wang, J. Am. Ceram. Soc., **95 [3]** (2012) 986–91.
15. H. B. Sharma, Ferroelectrics., **453** (2013) 113–21.
16. A. Piorra, A. Petraru, H. Kholstedt, M. Wuttig, E. Quandt, J. Appl. Phys., **109** (2011) 104101-5.
17. C. Tsakonas, W. Cranton, F. Li, K. Abusabee, A. Flewitt, D. Koutsogeorgis, J. Phys. D: Appl. Phys., **46** (2013) 095305-14.
18. W. Ma, D. Hesse. Appl. Phys. Lett., **84 [15]** (2004) 2871-3.
19. C. Fu, W. Cai, H. Chen, S. Feng, F. Pan, C. Yang, Thin solid films., **516** (2008) 5258-61.
20. Y. Lin, G. Wu, N. Qin, D. Bao, Thin Solid Films., **520** (2012) 2800-4.
21. M. Cole, C. V. Weiss, E. Ngo, S. Hirsch, L. A. Coryell, S. P. Alpay, Appl. Phys. Lett., **92** (2008) 182906-9.

22. V. Stancu, M. Lisca, I. Boerasu, L. Pintilie, M. Kosec, Thin Solid Films., **515** (2007) 6557-61.

23. V. S. Puli, D. K. Pradhan, S. Adireddy, R. Martinez, P. Silwal, J. F. Scott, C. V. Ramana, D. B. Chrisey, R. S . Katiyar, J. Phys. D: Appl. Phys., **48** (2015) 355502-13.

24. L. Zhang, S. Jiang, Y. Zeng, M. Fu, K. Han, Q. Li, Q. Wang, G. Zhang, Ceram. Inter., **40** (2014) 5455-60.

25. B. A. Tuttle, D. A. Payne, Ferroelectrics., **37** (1981) 603-6.

26. D. Zhan, Q. Xu, D. P. Huang, H. X. Liu, W. Chen, F. Zhang, J. Alloys Compd., **682** **(**2016) 594-600.

27. T. Sa, N. Qin, G. Yang, D. Bao, Mater. Chem. Phys., **139** (2013) 511-14.

28. J. Parui, S. B. Krupanidhi, Appl. Phys. Lett., **92** (2008) 192901-5.

29. Y. P. Wang, T. Y. Tseng, J. Appl. Phys., **81** (1997) 6762-6.

30. Q. Lin, D. Wang, S. Li, J. Am. Ceram. Soc., **98 [7]** (2015) 2094–8.

31. Q. G. Chi, H. F. Zhu, J. C. Xu, X. Wang, J. Q. Lin, Z. Sun, Y. Chen, Q. Q. Lei, Ceram. Inter., **39** (2013) 8195–8.

32. A. Gruverman, A. Kholkin. Rep. Prog. Phys., **69** (2006) 2443-74.

33. A. L. Kholkin, S. V. Kalinin, A. Roelofs, A. Gruverman, Alexei Gruverman Publications., (2007) p. 46.

34. Z. Chen, J. Huang, Y. Yang, Y. Wang, Y. Wu, H. He, X. Wei, Z. Ye, H. Zeng, H. Cong, Z. Jaing, RSC Adv., **2** (2012) 7380-3.

35. P. Bharathi, P. Thomas, K. B. R. Varma, J. Mater. Chem. C., **3** (2015) 4762.

36. D. V. Taylor, D. Damjanovic, Appl. Phys. Lett., **76 [12]** (2000) 1615-7.

Chapter 6

Phase, microstructure and electrical properties of BCZT films grown in oxygen-rich atmosphere, in 200 nm thickness range

In this chapter the effect of oxygen processing on the microstructure and electrical properties of the BCZT thin films is presented.

6.1 Introduction

Rapid developments of miniature power electronics and pulsed power systems in the recent years triggered the necessities for the development of low cost high ESD and high ESF dielectric capacitors [1-5]. Recent advancements in this area have been highlighted with the reports on polyvinylidene fluoride (PVDF)-based relaxor-ferroelectric (RFE) polymer and Pb-based antiferroelectric (AFE) films. ESD as high as 25 J/cm^3 at an electric field > 8 MV/cm and 61 J/cm^3 at an electric field of 4.3 MV/cm respectively were reported for these films [6, 7]. However, high ESD in these systems was achieved at very high electric field where the energy ESF was compromised to a higher extent. Recently, worldwide campaigning for environment friendly functional materials forced the researcher for the development of the Pb free systems leading to the innovation of some potential Pb free films with very high ESD. BFSTO ($0.60SrTiO_3 -0.40BiFeO_3$) thin films processed by PLD on Nb-doped single crystal $SrTiO_3$ substrate with ESD 70.3 J/cm^3 at an electric field of 3.85 MV/cm [4], antiferroelectric $Hf_xZr_{1-x}O_2$(HZO) thin films developed by combined DC sputtering and thermal atomic layer deposition (ALD) on Si/TiN substrate with ESD 46 J/cm^3 at electric field of 4.5 MV/cm [8], multilayered thin film containing barium zirconate titanate (BZT) and barium calcium titanate (BCT) layers processed by magnetron sputtering on Nb-doped single crystal $SrTiO_3$ substrate with ESD 52.4

J/cm^3 at electric field of 4.5 MV/cm [5], PLD processed epitaxial BNLBTZ thin film on single crystal $SrTiO_3$ substrate with ESD as high as 154 J/cm^3 at electric field of 3.5 MV/cm [9], were already reported in the literature. However, implementation of energy storage at very high electric field poses critical disadvantages towards practical applications of energy storage device. Special insulations are essential to shield the device components from electric discharge at high electric field and for safe charge-discharge cycles of the electrical capacitor. Moreover, risk of electric breakdown is higher at high electric field [10, 11]. Hence, current research is focused on the achievement of high ESD and ESF at lower electric field [10, 12]. Very recently S. Cho et al. [13] reported PLD processed $BaTiO_3$-$BiFeO_3$ (BTO-BFO) thin film on single crystal $SrRuO_3/SrTiO_3$ substrate with ESD of 52 J/cm^3 at an electric field of 2.05 MV/cm. Do-Kyun Kown et al. [14] reported $BaTiO_3$–$Bi(MgTi)O_3$ (BT-BMT) thin films processed by chemical solution deposition (CSD) on Pt-coated Si wafer with ESD of 37 J/cm^3 at a low electric field of 1.9 MV/cm. However, there were no reports on energy storage efficiency and fatigue properties of the films in these two communications, without which true potential of those systems could not be estimated. CSD processed ferroelectric films received considerable attention towards practical application in MEMs industries since films with reproducible properties and larger area can be processed by CSD. Recently Liu et al. [15] reported giant piezoelectric properties (d_{33} = 620 pC/N) for a lead free composition: $0.5Ba(Zr_{0.2}Ti_{0.8})O_3$-$0.5(Ba_{0.7}Ca_{0.3})TiO_3$ however, energy storage and fatigue properties of this composition in the form of thin film remained largely unexplored.

In the present work exceptionally high ESD of 64.8 J/cm^3 was achieved at a low electric field of 2.0 MV/cm (2000 kV/cm) for a CSD processed lead free $Ba_{0.85}Ca_{0.15}Ti_{0.90}Zr_{0.10}O_3$ (BCZT) ferroelectric thin film on Pt coated Si substrate with superior polarization fatigue resistance (up to 10^{10} cycles) and considerable ESF (73%). Reports on such high ESD at that low electric field range along with superior fatigue properties for a lead free ferroelectric system are extremely limited in the literature. We have observed that the thin films grown and annealed in oxygen rich atmosphere displayed slim hysteresis loop characteristics with high P_{max} (106 μC/cm^2) which were suitable for obtaining high ESD. Effects of oxygen atmosphere during crystallization of the film and annealing on the concentration of the oxygen vacancies present in the film were also discussed.

6.2 Experimental methods

BCZT thin films were deposited on Si/SiO_2/TiO_2/Pt (100) substrates following sol-gel spin coating technique as discussed in the section 2.5.1. However, the BCZT wet films were dried on hot plate at ~150 ^oC. The dried BCZT thin films were processed in two different types of atmosphere. The first set of films were grown in ambient air atmosphere and the other set of films were grown and annealed in oxygen rich atmosphere (oxygen pressure of 3 bars at the entree port of the tubular furnace) at 700 and 800 ^oC temperature using conventional tubular furnace. Higher oxygen pressure was avoided because the reported literature indicated that processing of ferroelectric films in the atmosphere with very high oxygen partial pressure decreased the crystallinity of the films [16]. Phase and crystal structure of the BCZT thin films were analyzed by GIXRD using cobalt kα radiation. Thickness of the BCZT films was studied with HRTEM. Electrical properties of the films were measured using SCS-4200 machine. Surface morphology and roughness were studied by AFM. Concentration of lattice oxygen, oxygen vacancy and chemisorbed oxygen in the BCZT films were characterized using X-ray photo electron spectroscopy (XPS, Omicron Nanotechnology, U.K). Phase, surface morphology and electrical properties of the BCZT films were analyzed at room temperature.

6.3 Results and discussion

6.3.1 Phase and topography

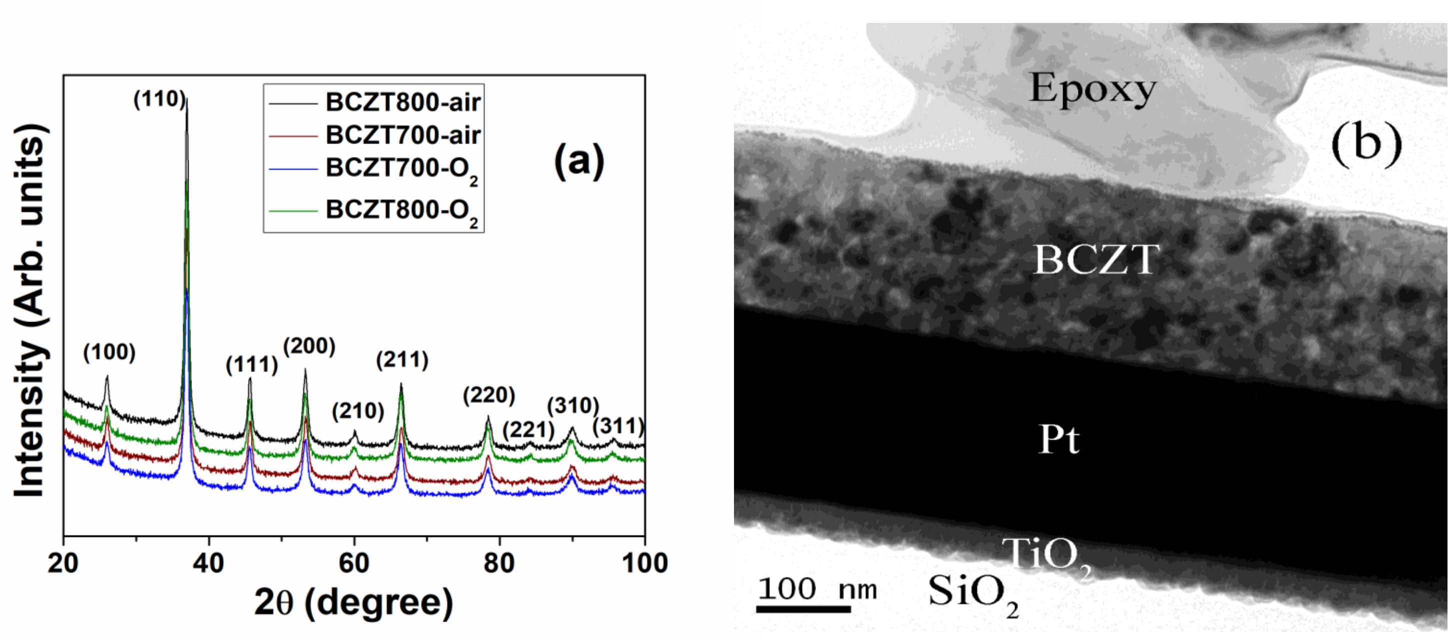

Fig. 6.1 (a) GIXRD patterns of the air and oxygen processed BCZT films and (b) cross section TEM image of the BCZT film.

GIXRD patterns of BCZT films processed in air and oxygen-rich atmosphere at 700 and 800 ^{o}C temperatures (BCZT700-air, BCZT800-air, BCZT700-O_2 and BCZT800-O_2) are presented in Fig. 6.1 (a). A grazing angle of 0.5^{o} and cobalt kα radiation was used in order to avoid substrate-Pt and Si peaks. X-ray diffraction patterns of the films demonstrated the occurrence of pure polycrystalline BCZT with perovskite structure. Film thickness was measured by TEM and was found to be ~200 nm as shown in Fig. 6.1 (b).

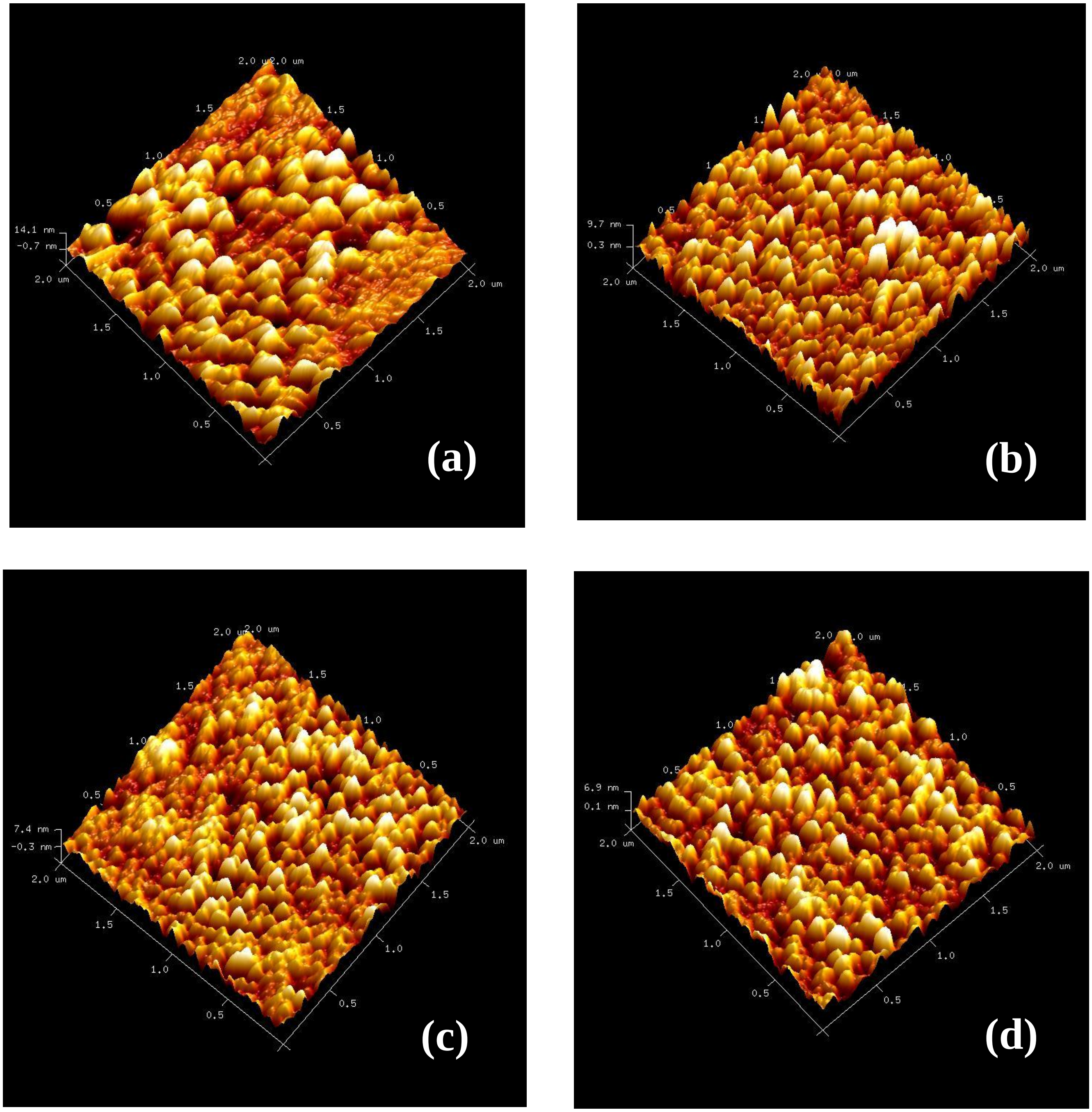

Fig. 6.2 AFM images of (a) BCZT700-air, (b) BCZT800-air, (c) BCZT700-O_2 and (d) BCZT800-O_2 films.

Surface morphology and surface roughness was investigated by AFM. It was observed from the AFM images shown in the Fig. 6.2 that the roughness of the films decreased with oxygen processing. The measured roughness for BCZT700-air, BCZT800-air, BCZT700-O_2 and BCZT800-O_2 were 3.15 nm, 2.16 nm, 1.66 nm and 1.64 nm respectively. Moreover, it was observed from the AFM images that oxygen processing increased grain size uniformity by suppressing uneven grain growth.

6.3.2 Characterization by X-ray photo electron spectroscopy

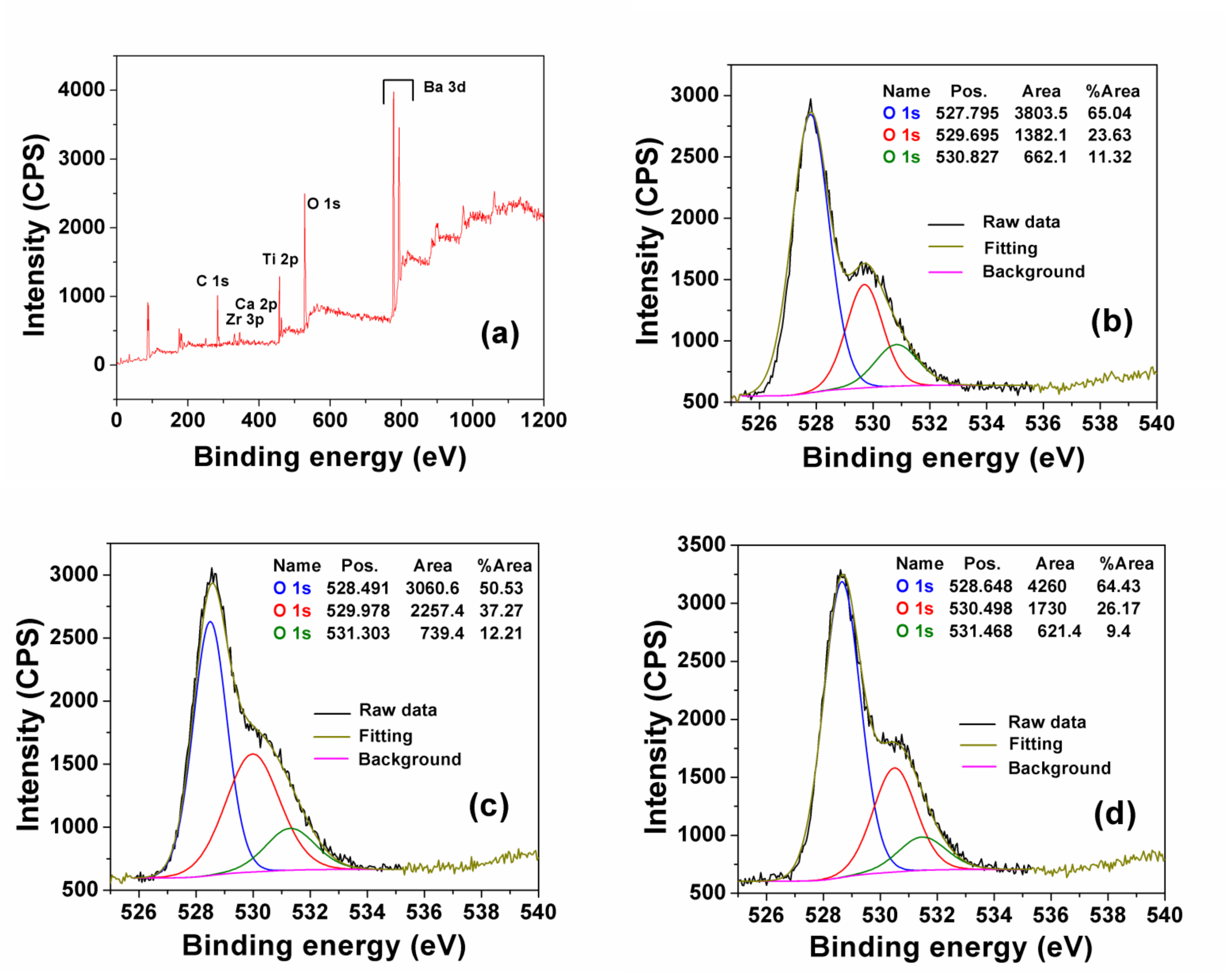

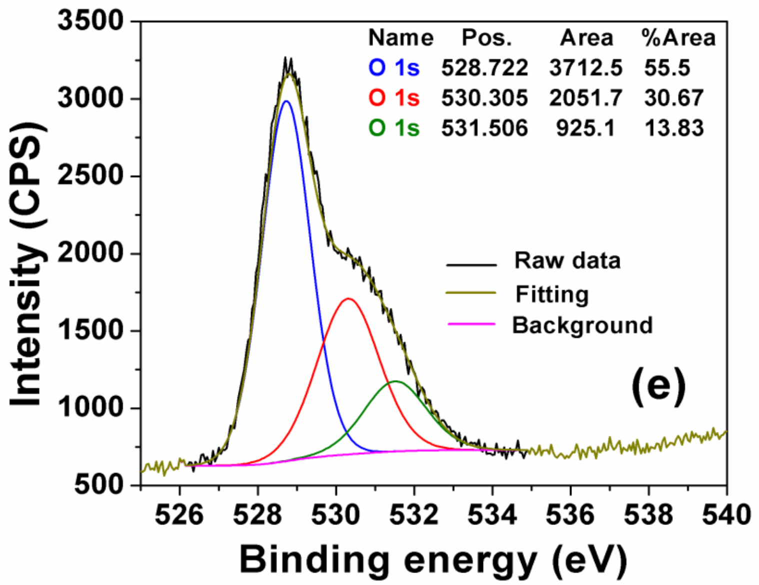

Fig. 6.3 (a) XPS survey spectrum obtained from the surface of the BCZT700-O_2 film, high resolution O 1s spectrum of (b) BCZT700-O_2, (c) BCZT700-air, (d) BCZT800-O_2 and (e) BCZT800-air films.

Since, the BCZT thin film samples were processed in two different atmosphere (ambient air and oxygen-rich atmosphere) it was assumed that some of the oxygen vacancies which usually result from ambient air processing of the ceramic oxide thin films, would be compensated by processing the same in oxygen rich atmosphere. To investigate the effect of oxygen processing on the concentration of oxygen vacancies in the BCZT films, XPS measurements were performed. The XPS survey spectrum obtained from the surface of the BCZT700-O_2 film is presented in Fig. 6.3 (a). As expected the survey spectrum shows the occurrence of Ba, Ca, Zr, Ti and O peaks. However, the spectrum also indicates the existence of carbon due to atmosphere contamination. C. Miot et al. [17] reported XPS spectrum with high concentration of carbon that obtained from the surface of $BaTiO_3$ ceramics. Moreover, in that XPS analyses, the amount of carbon reflected in the spectrum increased with the time of exposure of the samples in air as well as in ultrahigh vacuum conditions. In the present analyses on the XPS spectra of BCZT thin films, carbon 1s peak centered at 284 eV is considered as the reference for calibrating binding energies of the elements present in BCZT composition. Fig. 6.3 (b) to 6.3 (e) shows the O 1s spectra of the BCZT-air and BCZT-O_2 films. The unsymmetrical O1s peak in each spectrum was deconvoluted into three different component peaks. The peaks are centered at 528.49, 529.97 and 531.3 eV for the BCZT700-air film. The peak centered at 528.49 eV corresponds to lattice oxygen ions (O^{2-}) in the perovskite structure, whereas, the peak centered at 529.97 eV is attributed to the O_2^-/O^- ions caused by oxygen vacancies. And the peak centered at 531.3 eV originates due to chemisorbed oxygen on the thin film surface as reported earlier by Y. Tu et al. [18] and I. Usman et al. [19] for the ZnO nano-rods and ZnO thin films respectively. However, the little shift in binding energy for O 1s spectral components in BCZT thin films is due to different chemical environment and as well as due to charging during XPS experiments [20]. Analyses on the XPS spectra of the air and oxygen processed BCZT thin films revealed that oxygen processing considerably reduced the area of the peak corresponding to the oxygen vacancy and increased the area of the peak corresponding to the lattice oxygen in the BCZT-O_2 films. From these observations it can be concluded that oxygen processing effectively compensated the oxygen vacancies that present in the air-processed BCZT films.

6.3.3 Dielectric and ferroelectric property measurements

Fig. 6.4 (a) and 6.4 (b) present the variation of dielectric constant and loss with DC electric field at 10 kHz frequency for BCZT films. BCZT-air films exhibited higher dielectric constant and higher dielectric loss than that of the BCZT-O_2 films. XPS measurements indicated that higher concentration of oxygen vacancy exists in the thin films processed in air compared to the films that were processed in oxygen-rich atmosphere. Oxygen vacancies in a ferroelectric film are believed to create conducting electrons as per the equation (6.1).

$$O_o(Oxygen\ ion\ at\ its\ normal\ site) \longrightarrow Vo^{+2}(Oxygen\ vacancy) + 2e^- + \frac{1}{2}O_2 \qquad (6.1)$$

The interactions of these electrons with the dipoles result high dielectric constant [21, 22]. The equation (6.1) pertaining to creation of the oxygen vacancy shifts to reverse direction in oxygen-rich atmosphere leading to compensation of the oxygen vacancies. The extent of vacancy compensation will depend on the oxygen partial pressure and processing temperature. The reduced oxygen vacancies in the oxygen-processed films reduce the formation of conduction electrons and defect dipoles and thus the dielectric constant is lowered in the BCZT-O_2 films. However, the higher dielectric constant of the BCZT films annealed at 800 ^oC temperature compared to the low temperature annealed films is attributed to the dense microstructure of the films. Dielectric loss of BCZT-O_2 films varied between 0.015 and 0.028 in the measured range of electric field and is comparable to its bulk ceramic counterpart [23]. Whereas, the same varied between 0.048 and 0.056 for the BCZT-air films, i.e. the recorded dielectric loss is 2-3 times higher than that of the BCZT-O_2 films. It is known that oxygen annealing reduces both the dielectric loss and leakage current in ferroelectric thin films [24]. Fig. 6.4 (c) represents the frequency dependant dielectric constant and loss for BCZT-O_2 films measured at room temperature with the application of 100 mV AC amplitude and 5 V DC amplitude. The figure indicates that dielectric constant varies minutely with frequency and the dielectric loss increases slightly as the frequency is increased.

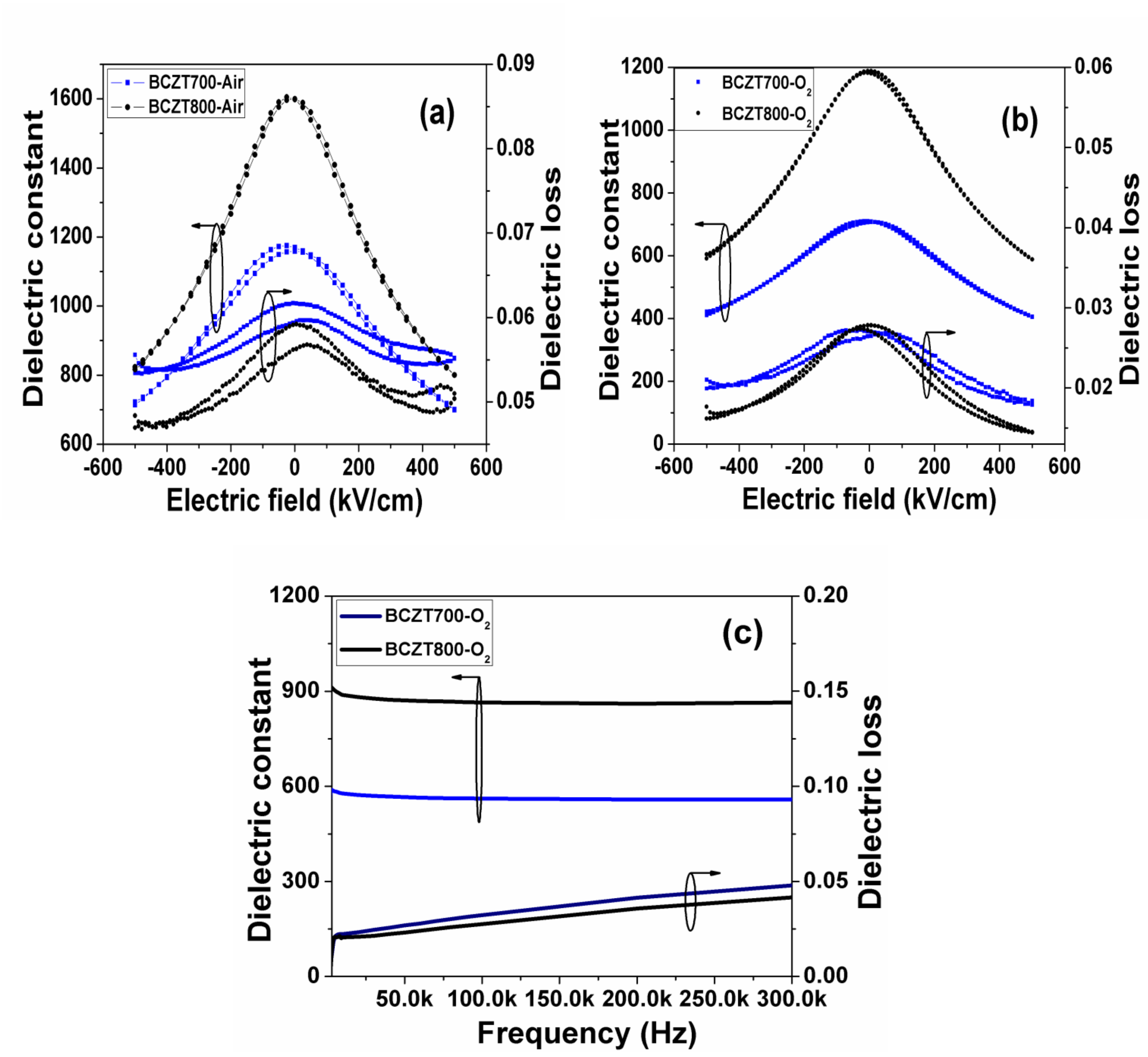

Fig. 6.4 (a) DC electric field dependant dielectric constant and loss for BCZT-air films, (b) DC electric field dependant dielectric constant and loss for BCZT-O_2 films and (c) Frequency dependant dielectric constant and loss for the BCZT-O_2 films.

Fig. 6.5 (a) shows the P vs. E hysteresis loop of the BCZT-air and BCZT-O_2 films measured at 1000 kV/cm electric field and 10 kHz frequency. Previous studies by different research groups revealed that oxygen vacancies are the major sources of point defects in ferroelectric oxides. These defects usually increase leakage current which in-turn changes P-E hysteresis behavior as an immediate effect [25, 26]. Air-processed BCZT800 films exhibited fat hysteresis loops with the P_{max} of 82 $\mu C/cm^2$ and P_r of 25 $\mu C/cm^2$. Whereas the BCZT800 films processed in oxygen-rich atmosphere showed very slim hysteresis loops with the P_{max} of 73 $\mu C/cm^2$ and P_r of 5 $\mu C/cm^2$ at an electric field of 1000 kV/cm. Moreover, coercivity (E_c) decreased by 4-5 times due to processing the films in oxygen-rich atmosphere (Fig. 6.5 (a)). Similar significant changes in polarization and coercivity have also been observed for the BCZT700-O_2 films (Table 6.1). This decrease in E_c can be attributed to the lowering of oxygen vacancies in the oxygen-processed thin films. Oxygen vacancies are the dominant point defect in oxide ferroelectric materials and have been regarded as the cause of pinning of domain walls, screening the electric field near the space charge region. These two factors are strongly considered to increase the E_c in the ferroelectric oxide materials particularly in the form of thin films [27]. Oxygen vacancy also significantly influenced the dielectric breakdown strength of the BCZT films. It was observed from the electrical property measurements that the average breakdown strength of the oxygen-processed BCZT thin films is two times higher than that of the air-processed BCZT films.

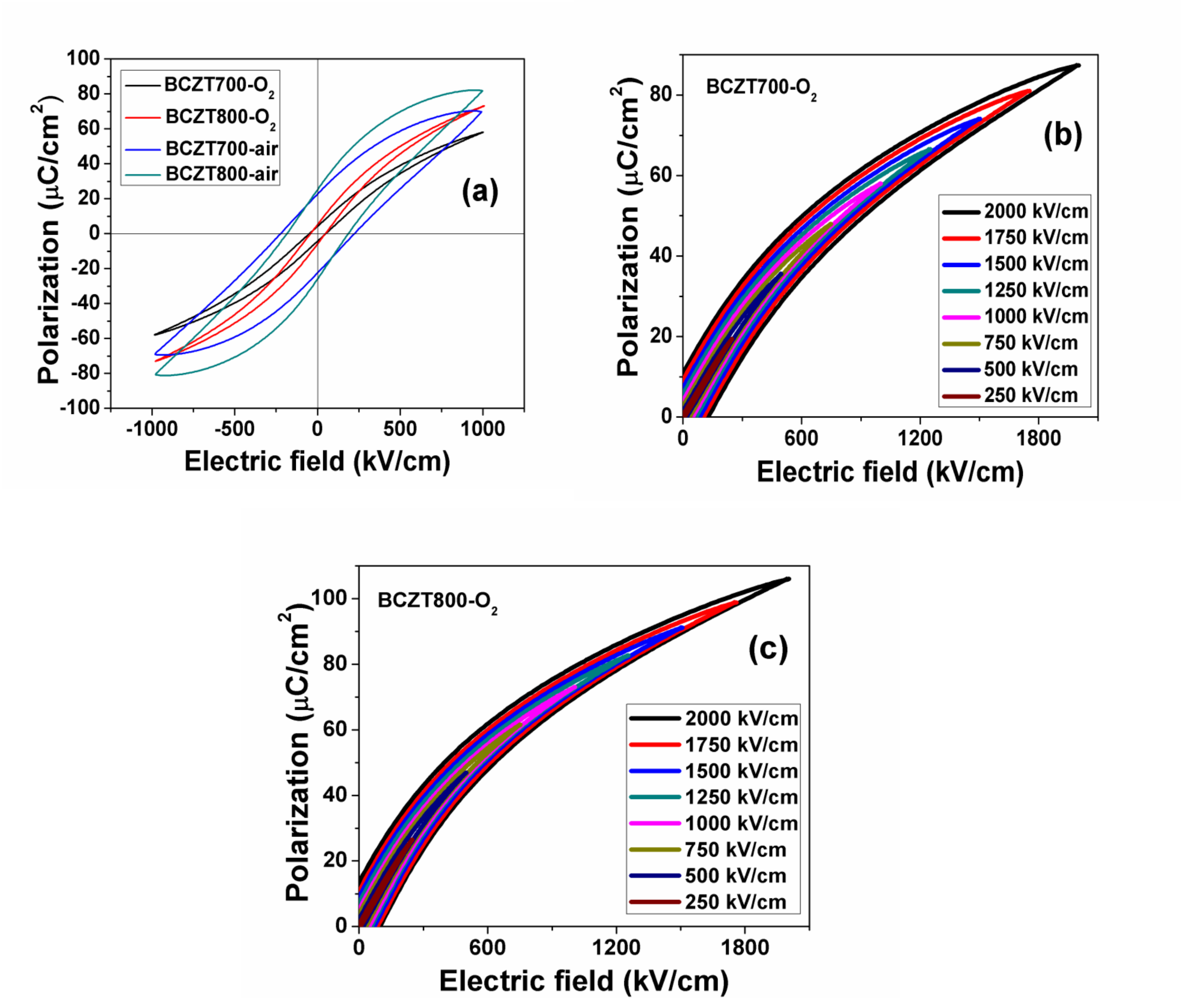

Fig. 6.5 (a) P vs. E hysteresis loops measured at 1000 kV/cm electric field for the BCZT-air and BCZT-O_2 films, P vs. E unipolar loops of (b) BCZT700-O_2 and (c) BCZT800-O_2 films measured with different electric fields.

Fig. 6.5 (b) and 6.5 (c) shows the P versus E unipolar loops for BCZT-O_2 films recorded at 10 kHz frequency with different electric fields. P_{max}, P_r and E_c increased with increasing electric field. BCZT700-O_2 film showed P_{max} of 87 μC/cm^2 and P_r of 11 μC/cm^2, while the BCZT800-O_2 film showed P_{max} of 106 μC/cm^2 and P_r of 12.9 μC/cm^2 at an applied electric field of 2000 kV/cm. However, P_{max}-P_r values for BCZT-O_2 films were significantly increased with the applied electric field. A higher value of P_{max}-P_r for the oxygen-processed BCZT films enabled to obtain high ESD and ESF.

Table 6.1 Ferroelectric properties of the air and oxygen processed BCZT films.

BCZT film	P_{max} (μC/cm^2) at 1000 kV/cm	P_r (μC/cm^2) at 1000 kV/cm	E_c (kV/cm)	P_{max} (μC/cm^2) at 2000 kV/cm	P_r (μC/cm^2) at 2000 kV/cm
BCZT700-air	70	22	222	-	-
BCZT800-air	82	25	185	-	-
BCZT700-O_2	58	4	49	87	11
BCZT800-O_2	73	5	45	106	12.9

6.3.4 Energy storage properties

The ESD and ESF of the BCZT films were calculated from the P vs. E loops using the equations (1.7) and (1.8). The maximum ESD values obtained from BCZT700-O_2 and BCZT800-O_2 at an electric field of 2000 kV/cm are 54.5 and 64.8 J/cm^3 respectively. Reports of such high values of ESD in Pb based or Pb free materials of any kind: dielectric/ferroelectric /antiferroelectric at E (electric field) ≤ 2000 kV/cm are very limited in the literature. For practical energy storage device applications, ESF is as important as ESD. The calculated ESF for the BCZT700-O_2 and

BCZT800-O_2 thin films at an electric field of 2000 kV/cm are 68 % and 73 % respectively. The variations of ESD and ESF with electric field (up to 2000 kV/cm) are presented in the Fig. 6.6 (a). The Fig. 6.6 (a) shows that ESD for both the BCZT700-O_2 and BCZT800-O_2 thin films increased steadily with electric field up to 54.5 and 64.8 J/cm^3 respectively. Whereas, the ESF is decreased slowly with electric field from 90 % to 68 % for BCZT700-O_2 and from 90 % to 73 % for BCZT 800-O_2. The error bars in Fig. 6.6 (a) indicate the standard deviations for polarization measurements on different capacitors and associated inaccuracy in thickness measurements by cross section TEM. Fig. 6.6 (b) shows the position where the present revelation stands in terms of ESD and ESF compared to the same published so far in the literature. Reported values for ESD and ESF at electric field (E) ≤ 2000 kV/cm were considered for comparison because in the recent years, research on high energy density ferroelectric capacitors is emphasized on the achievement of high ESD at lower electric field [10, 12], since there is a greater risk of electric breakdown at high electric field [10, 11]. It should be noted that the ESD calculated from the ferroelectric hysteresis loops (Fig. 6.5 (b) and 6.5 (c)) for the oxygen-processed BCZT films are much higher than that calculated for the air-processed BCZT films (17 J/cm^3).

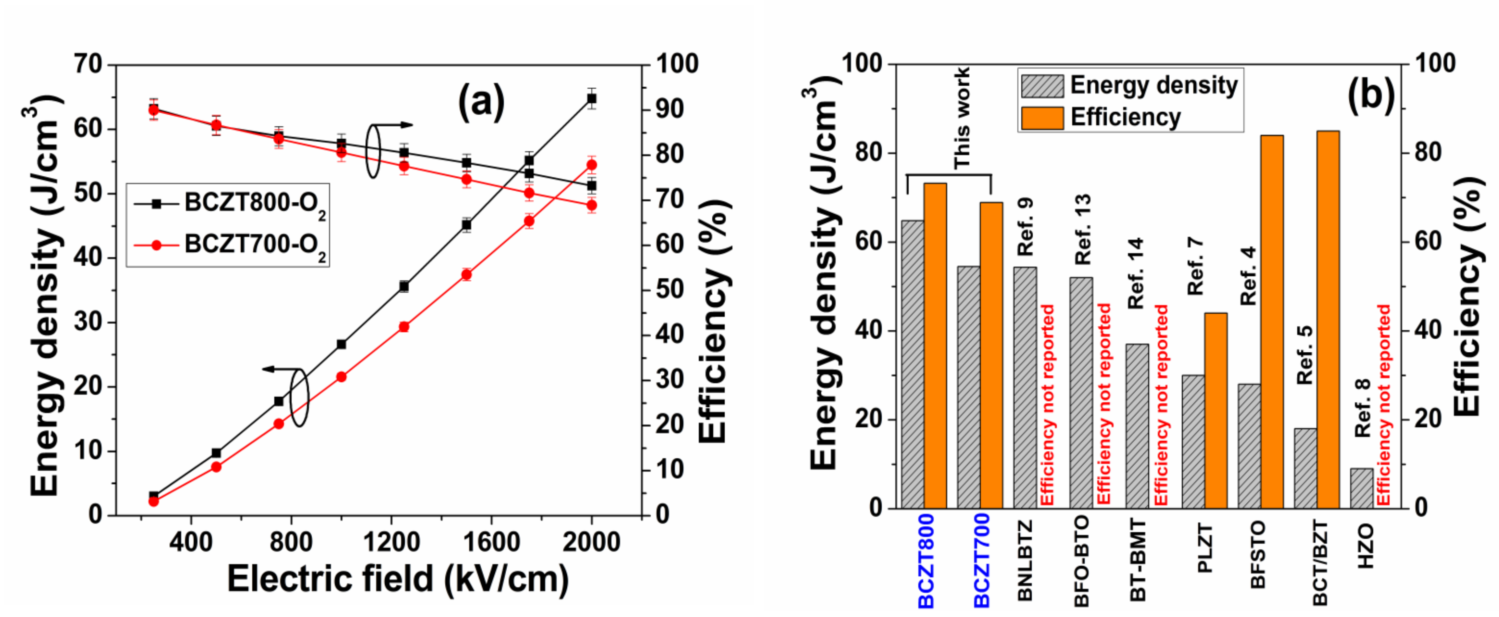

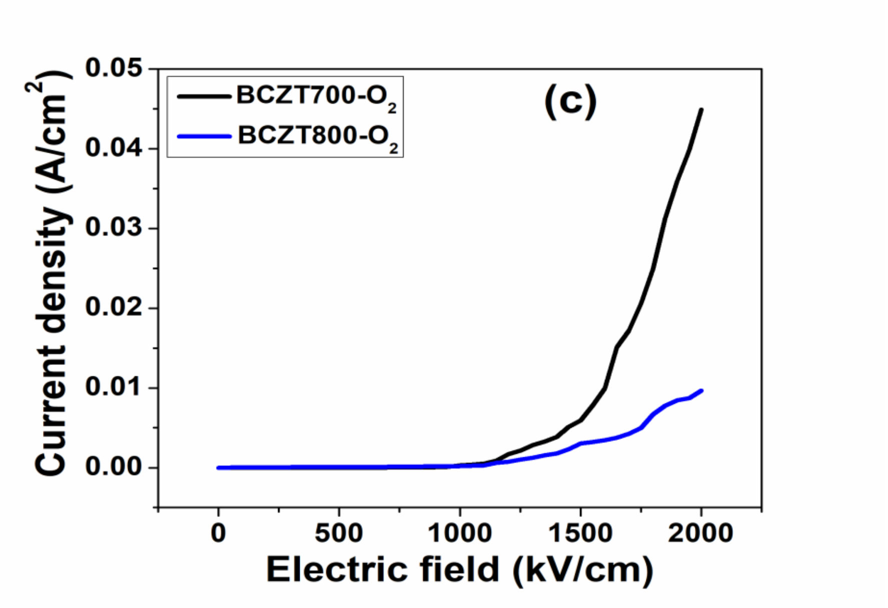

Fig. 6.6 (a) Variation of ESD and ESF with electric field for BCZT-O_2 films, (b) comparison of ESD and ESF that obtained in the present work for the oxygen-processed BCZT films with the literature reported so far and (c) leakage current density as a function of electric field for the BCZT-O_2 films.

Fig. 6.6 (c) represents the variation of leakage current density with electric field for BCZT-O_2 films. It is observed from the plots that current density increased very slowly with electric field up to a very high field of 1100 kV/cm followed by a steep increase up to 2000 kV/cm. Lower current density at higher electric field is very beneficial for ferroelectric energy storage application as it decreases the heating of the energy storage device, operating at high electric field. The measured current density for BCZT800-O_2 films at 100 kV/cm, 400 kV/cm, 500 kV/cm, 1000 kV/cm and 2000 kV/cm are 7.6 x10^{-6}, 5.5 x10^{-5}, 6.5 x10^{-5}, 1.9 x10^{-4} and 9.7 x10^{-3} A/cm^2 respectively. It should be noted that the present oxygen-processed BCZT thin films which were synthesized by chemical solution deposition technique offered much lower leakage current density than that of the PLD processed PZT thin films with oxide electrode (0.1 A/cm^2 at 400 kV/cm) [28], and PLD processed epitaxial BCZT thin film with similar composition grown on $SrTiO_3$ single crystal substrate (3.0 A/cm^2 at 400 kV/cm) [29].

6.3.5 Polarization fatigue test

Polarization fatigue resistance of the ferroelectric film is also an important criterion in ferroelectric energy storage application because any change in P_{max} or P_r during cycling will essentially change both ESD and ESF and hence ferroelectric films with considerably high fatigue resistance are desirable for this purpose. In the present work, the investigations on fatigue were performed by applying 5 V amplitude bipolar pulses with repetition at 1 MHz frequency. Negligible changes in P_{max} and P_r for both the BCZT700-O_2 and BCZT800-O_2 films were noticed even after 10^{10} switching cycles. The recorded P_{max} and P_r for the former after 10^{10} cycles are 85 and 12.5 μC/cm^2 which corresponds to ESD of 50.6 J/cm^3 and ESF of 63 % (Fig. 6.7 (a) and 6.7 (c)). The recorded P_{max} and P_r after 10^{10} switching cycles for the latter are 105 and 13.2 μC/cm^2 (Fig. 6.7 (b) and 6.7 (c)) which corresponds to ESD of 63.6 J/cm^3 and ESF of 71 %. The error bars in Fig. 6.7 (c) indicate the standard deviations for polarization measurements due to the inaccuracy in thickness measurements by cross section TEM.

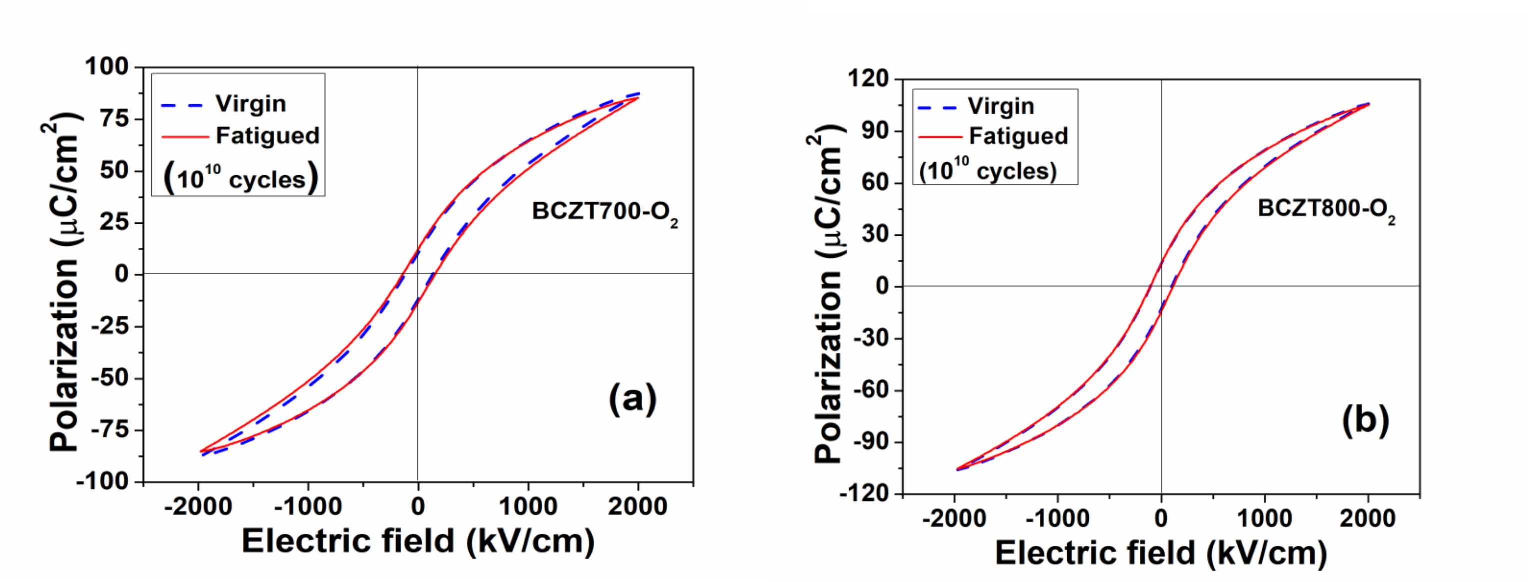

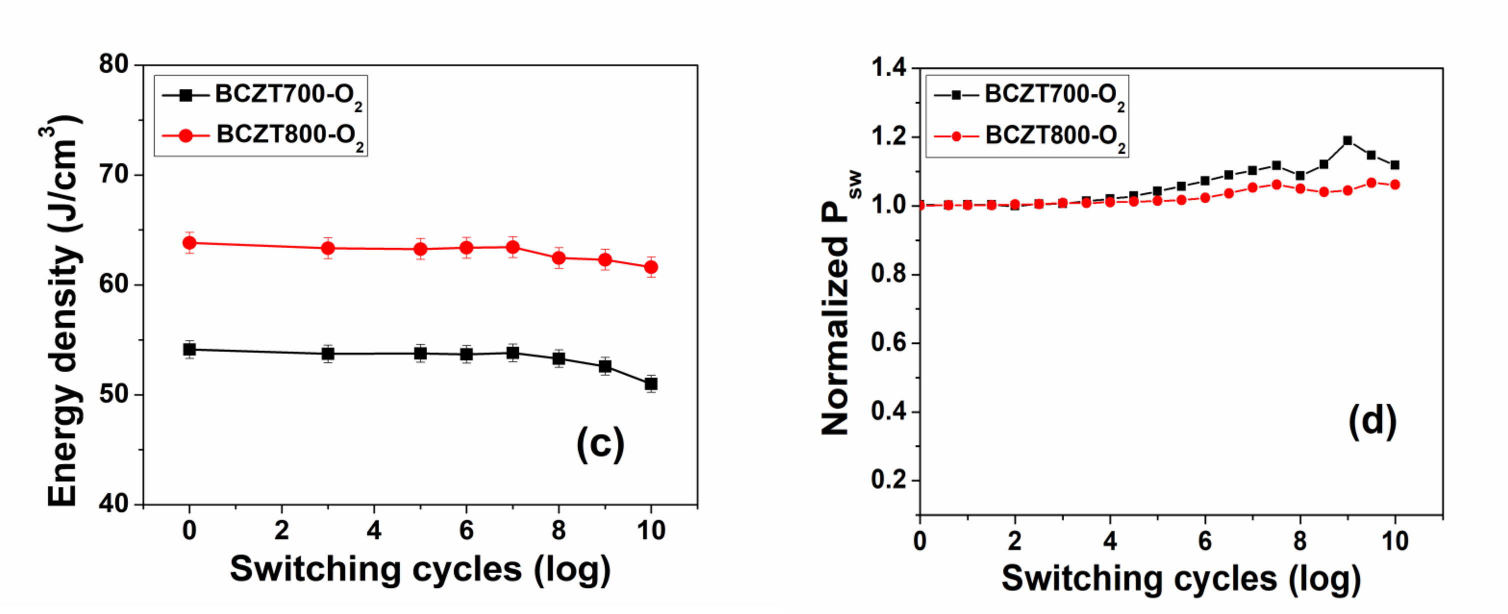

Fig. 6.7 (a)-(b) Virgin and fatigued polarization-electric field hysteresis loops recorded at 10 kHz for the BCZT700-O_2 and BCZT800-O_2 films, (c) energy density variation with switching cycles for BCZT-O_2 films and (d) normalized P_{SW} as a function of number of switching cycles recorded for BCZT-O_2 films.

Fig. 6.7 (d) shows the variation of normalized switchable polarization (P_{SW}) with the number of switching cycles in logarithm scale. A polarization increasing trend was observed up to 5 x10^7 switching cycles for the BCZT700-O_2 and BCZT800-O_2 films. An increasing polarization trend up to first few switching cycles was also theoretically predicted [30] and experimentally verified by different group of researchers for different ferroelectric compositions [31, 32]. Park et al. [8] attributed this phenomenon to the micro-structural evolution of the thin film at the film-electrode interface during cycling and/or to the decrease in density of defects (wake–up effect or polarization- unlocking). However, in the present system the increasing trend was not limited to the first few cycles but continued up to higher number of cycles before the system shows some fatigue. Polarization recovery after polarization degradation due to fatigue in the last few cycles was also observed for both the samples as it was reported by some other researchers for different ferroelectric compositions [32]. It was observed that for both BCZT700-O_2 and BCZT800-O_2 switchable polarization is well above the base line even after 10^{10} switching cycles and this type of polarization switching behavior with negligible fatigue is comparable to that of the PZT based thin film systems with oxide bottom electrodes e.g. RuO_2 , IrO_2 and $SrRuO_3$ [33-35]. It is to be noted that reports on fatigue resistance properties of BCZT thin films particularly of CSD processed BCZT thin films were not published in the literature. Very recently J. P. B. Silva et al. [36] reported ion beam sputtered Pt/BCZT/HfO_2:Al_2O_3/Au multilayered capacitors with energy density of 99.8 J/cm^3 and the capacitors were stable up to 10^8 switching cycles. However, the main disadvantage of ion beam sputtering is its low deposition rate and complexity in obtaining a large area film with uniform thickness.

6.4 Conclusions

Processing of BCZT thin films in oxygen rich atmosphere abruptly modifies the ferroelectric properties of the films which include much slimmer hysteresis loop, drastic increase in P_{max}-P_r, 4-5 fold decrease in coercive field and at least 2 fold increases in electric breakdown strength. The film BCZT800-O_2 showed highest ESD of 64.8 J/cm^3 and ESF of 73% at 2000 kV/cm and these values are higher than that obtained for the BCZT700-O_2 film. ESD increased steadily with applied electric field whereas, ESF decreased slowly with electric field. Leakage current measured on these chemical solution deposited BCZT-O_2 thin films is much lower than that reported for PLD processed PZT thin films and PLD processed BCZT thin films. Both the films showed excellent polarization fatigue properties. 99 % and 97 % of polarization recovery were observed for BCZT800-O_2 and BCZT700-O_2 films respectively even after 10^{10} switching cycles. Leakage current and fatigue properties of the BCZT700-O_2 are comparable to that of the BCZT800-O_2 film, however, the former showed lower energy storage properties than the latter. Therefore, it can be concluded that processing of ferroelectric films in oxygen-rich atmosphere is an effective way to improve the energy storage properties.

6.5 References

1. B. J. Chu, X. Zhou, K. L. Ren, B. Neese, M. R. Lin, Q. Wang, F. Bauer, Q. M. Zhang, Science., **313** (2006) 334-336.
2. B. Peng, Q. Zhang, X. Li, T. Sun, H. Fan, S. Ke, M. Ye, Y. Wang, W. Lu, H. B. Niu, X. Zeng, H. Huang, Appl. Mater. Inter., DOI: 10.1021/acsami.5b02790.
3. P. Khanchaitit, K. Han, M. R. Gadinski, Q. Li, Q. Wang, Nat. Commun., DOI: 10.1038/ ncomms3845.
4. H. Pan, Jing Ma, Ji Ma, Q. Zhang, X. Liu, B. Guan, L. Gu, X. Zhang, Y. J Zhang, L. Li, Y. Shen, Y. H. Lin, C. W. Nan, Nat. Commun., DOI: 10.1038/s41467-018-04189-6.
5. Z. Sun, C. Ma, M. Liu, J. Cui, L. Lu, J. Lu, X. Lou, L. Jin, H. Wang, C. L Jia, Adv. Mater., DOI: 10.1002/adma.201604427.
6. L. Zhu, Q. Qang, Macromolecules., **45** (2012) 2937–2954.
7. Z. Hu, B. Ma, R. E. Koritala, U. Balachandran, Appl. Phys. Lett., **104** (2014) 263902.
8. M. H. Park, H. J. Kim, Y. J. Kim, T. Moon, K. D. Kim, C. S. Hwang, Adv. Energy Mater., **4** (2014) 1400610.
9. B. Peng , Q. Zhang , X. Li , T. Sun , H. Fan , S. Ke , M. Ye , Y. Wang , W. Lu , H. Niu , J. F. Scott , X. Zeng, H. Huang, Adv. Electron. Mater., (2015) 1500052.

10. A. Chauhan, S. Patel, R. Vaish, C. R. Bowen, Materials., **8** (2015) 8009-8031.
11. W. V. Hassenzahl, D. W. Hazelton, B. K. Johnson, P. Komarek, M. Noe, C. T. Reis, , Proc. IEEE., **92** (2004) 1655-74.
12. J. Gao, Y. Wang, Y. Liu, X. Hu, X. Ke, L. Zhong, Y. He, X. Ren, Sci. Reports., DOI:10.1038/srep40916.
13. S. Cho, C. Yun, Y. S. Kim, H. Wang, J. Jian, W. Zhang, J. Huang, X. Wang, H. Wang, J. L. M. Driscoll, Nano energy., **45** (2018) 398-406.
14. D. K. Kwon, M. H. Lee, IEE. Trans. Ultrason. Ferroelec. Freq. control., **59 [9]** (2012) 1894-99.
15. W. Liu, X. Ren, PRL., **103** (2009) 257602.
16. M. T. Escote, F. M. Pontes, E. R. Leite, E. Longo, R. F. Jardim, P. S. Pizani, J. Appl. Phys., **96 [4]** (2004) 2186-91.
17. C. Miot, E. Husson, C. Proust, R. Erre, J. P. Coutures, J. Mater. Res., **12 [9]** (1997) 2388.
18. Y. Tu, S. Chen, X. Li, J. Gorbaciova, W. P. Gillin, S. Krause, J. Briscoe, J. Mater. Chem. C., **6** (2018) 1815.
19. I. Usman, R. S. Rawat, T. L .Tan, P. Lee, R. Chen, H. D. Sun, L. Fengji, S. Zhang, J. Appl. Phys., **110** (2011) 093522.
20. V. Craciun, R. K. Singh, Appl. Phys. Lett., **76 [14]** (2000) 1932.
21. L. Fang, M. Shen, W. Cao, J. Appl. Phys., **95 [11]** (2004) 6483.
22. C. Ang, Z. Yu, L. E. Cross, Phys. Rev. B., **62[1]** (2000) 228.
23. S. Rangaswamy Reddy, V. V. Bhanu Prasad, Pawan Kumar, K. Prabahar, Vishnu Shanker, Subir Roy, J. Mater. Sci. Mater. Elect., **29 [14]** (2018) 12451-12456.

24. C. Wang, M. Takahashi, H. Fujino, X. Zhao, E. Kume, T. Horiuchi, S. Sakai, J. Appl. Phys., **99** (2006) 054104.
25. H. Yang, Y. Q. Wang, H. Wang, Q. X. Jia, Appl. Phys. Lett., **96** (2010) 012909.
26. T. Friessnegg, S. Aggarwal, R. Ramesh, B. Nielsen, E. H. Poindexter, D. J. Keeble, Appl. Phys. Lett., **77 [1]** (2000) 127-129.
27. F. Xia, X. Yao, J. Appl. Phys., **92 [5]** (2002) 2709-16.
28. L. Pintilie, I. Vrejoiu, D. Hesse, G. Lerhun, M. Alexe, Phys. Rev. B., **75** (2007) 104103.
29. Q. Lin, D. Wang, S. Li, J. Am. Ceram. Soc., **98 [7]** (2015) 2094–8.
30. V. Y. Shur, E. L. Rumyantsev, E. V. Nikolaeva, E. I. Shishkin, I. S. Baturin, Phys. Solid state., **44 [11]** (2002) 2049.
31. D. Zhou, J. Xu, Y. Guan, F. Cao, X. Dong, J. Muller, T. Schenk, U. Schroder, Appl. Phys. Lett., **103** (2013) 192904.
32. L. Pintilie, I. Vrejoiu, D. Hesse, M. Alexe, Appl. Phys. Lett., **88** (2006) 102908.
33. H. N. Al-Shareef, O. Auciello, A. I. Kingon, J. Appl. Phys., **77 [5]** (1995) 2146.
34. X. J. Lou, J. Appl. Phys., **105** (2009) 024101.
35. A. K. Tagantsev, I. Stolichnov, E. L. Colla, N. Setter, J. Appl. Phys., **90 [3]** (2001) 1387.
36. J. P. B. Silva, J. M. B. Silva, M. J. S. Oliveira, T. Weingartner, K. C. Sekhar, M. Pereira and M. J. M. Gomes, Adv. Funct. Mater., (2018) 1807196.

Chapter 7

Deposition, microstructure, electrical and nano-mechanical properties of oxygen-processed thicker BCZT films

In this chapter microstructure, dielectric, ferroelectric and nano-mechanical properties investigation on the thicker BCZT films were presented.

7.1 Introduction

Since the invention of MEMs technology piezoelectric thin films have been widely used in sensing and actuating applications [1-4]. However, the degradation of the electromechanical properties of piezoelectric materials by mechanical fatigue has been proved to be an important criterion for actuators, especially those which are in continuous operation. Moreover, thin films show significant variation in mechanical properties as compared with the bulk due to the difference in size, surface forces such as frictional and adhesive forces. Elastic modulus and hardness are the two most important properties for the membrane structure usually observed in MEMS, which can influence the stiffness of the structure [5]. So far several methods such as impulse acoustic method, atomic force microscopy, Brillouin light scattering method and nanoindentation were developed in order to assess the mechanical properties of the thin films. Among these nanoindentation is widely used to measure the mechanical properties of the materials in nano-scale due to the high sensitivity, better resolution and easy operation [6, 7]. Moreover, the nanoindentation test has long been applied to quantitatively assess the adhesion of film-substrate systems. There was much research on nano-mechanical properties of PZT films fabricated by sol–gel and screen printing techniques [8-11]. However, nanoindentation based nano-mechanical properties of Pb-free highly piezoelectric BCZT thin films are still limited [12, 13]. In the present work electrical and nano-mechanical properties on the thicker BCZT film were investigated. A thicker BCZT film (thickness: ~750 nm) was developed on platinum coated Si (100) substrate by sol-gel deposition technique using a polymeric additive: polyvinyl pyrrolidone. The thicker film was used in nanoindentation measurements to allow indentations at penetration depth and mechanical properties thus determined will have negligible effect of substrate.

7.2 Experimental procedure

Thicker $Ba_{0.85}Ca_{0.15}Ti_{0.90}Zr_{0.10}O_3$ (BCZT) films were fabricated on platinum coated Si (100) substrates by following sol-gel deposition technique as described in the section 2.5.1. However for thicker film deposition concentrated BCZT sol with molarity of 0.67 was prepared through solvent evaporation with the aid of polyvinyl pyrrolidone (PVP) binder. For this PVP was added to the BCZT precursor sol in the molar ratio of 1:1 (BCZT:PVP). The concentrated sol was coated on the platinum coated silicon (100) substrate by the spin coater and the wet films were dried at ~150 ^{o}C. The dried films were grown using tubular furnace at 700 and 800 ^{o}C temperatures in oxygen-rich atmosphere. Phase and crystal structure of the deposited films were identified by conventional X-ray diffraction technique using copper-kα radiation. Surface morphology and thickness of the thin films were studied by FESEM. AFM was used to study the topography of the deposited films. Dielectric properties and leakage current behavior of the BCZT films were studied by SCS-4200 system. P-E hysteresis loops were recorded using the advanced ferroelectric evaluation system. The nano-mechanical properties of the BCZT thicker films were evaluated using nanoindenter (UNHT-module, make: CSM Instruments, Switzerland). Microstructure, electrical and nano-mechanical properties of the thicker BCZT films were studied at room temperature.

7.3 Results and discussion

7.3.1 Phase and microstructure

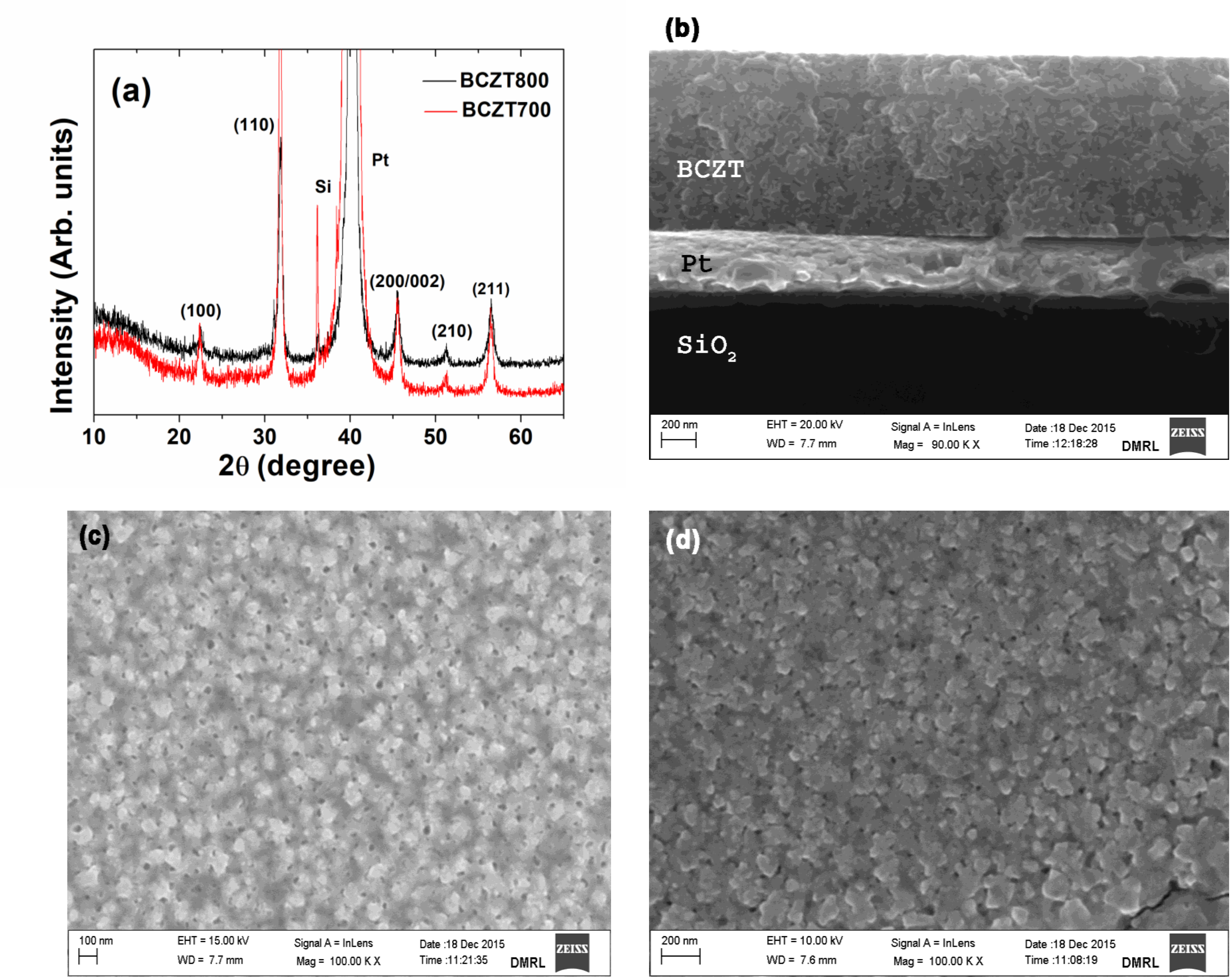

Fig. 7.1 (a) XRD patterns of the oxygen-processed thicker BCZT700 and BCZT800 films, (b) FESEM image of BCZT film cross-section, FESEM image showing the surface morphology of the oxygen-processed thicker (c) BCZT700 and (d) BCZT800 films.

Fig. 7.1 (a) shows the XRD patterns of the oxygen-processed thicker BCZT films crystallized at 700 °C (BCZT700) and 800 °C (BCZT800), respectively. XRD patterns of the both films indicate the presence of perovskite crystal structure and it is consistent with the reported diffraction patterns of the BCZT films [14]. Thickness of the BCZT film was detected by FESEM of the film cross section. The FESEM image given in Fig. 7.1 (b) shows the thickness of the film is ~750 nm. Fig. 7.1 (c) and 7.1 (d) show the FESEM images of the BCZT film surface crystallized at 700 and 800 °C. The image in Fig. 7.1 (c) shows granular surface morphology with grain size ranges between 24 to 136 nm, without indications of uneven grain growth. The grains are separated either by matrix or pores. However, the 800 °C annealed film shows grain agglomeration which is believed to be the initial stage of uneven grain growth at higher annealing temperature. In Fig. 7.1 (d) it is observed that grains are joined together forming plate like agglomerates. The pore size and percentage of porosity is much higher in the BCZT700 film than that in the BCZT800 film. The AFM images in Fig. 7.2 (a) and 7.2 (b) also show higher percentage of porosity in the 700 °C annealed film. The grains of BCZT800 film shows much higher grain growth than that in BCZT700 film.

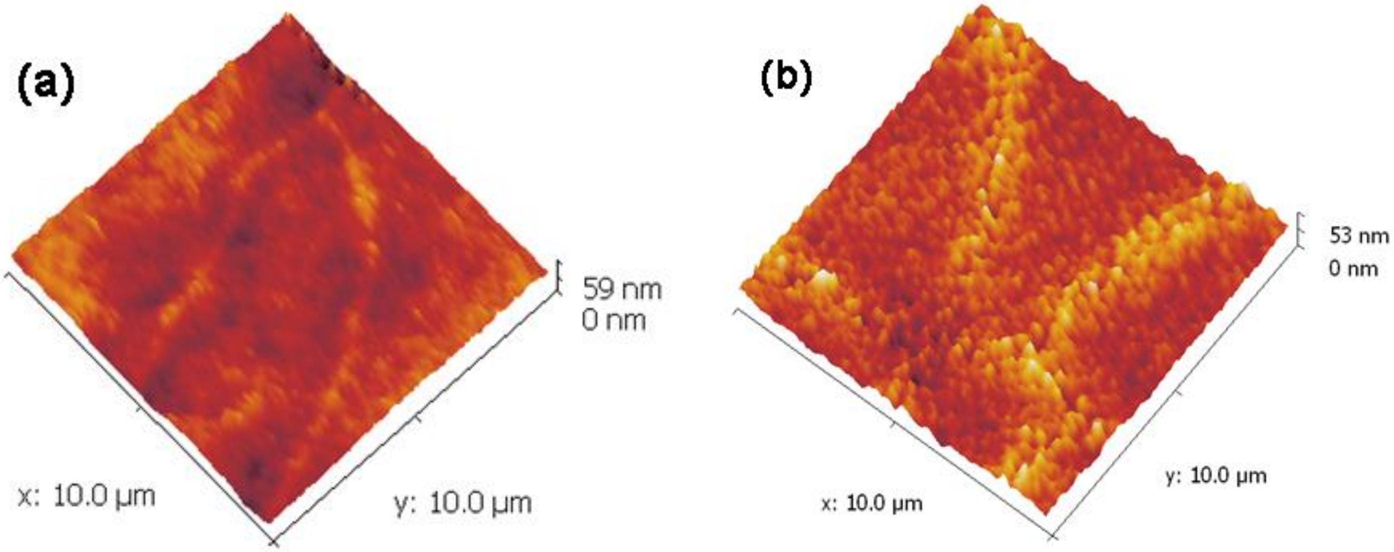

Fig. 7.2 AFM images showing the topography of (a) BCZT700 and (b) BCZT800 films.

7.3.2 Dielectric and ferroelectric property characterization

Fig. 7.3 (a) shows the variation of dielectric constant and loss with the applied frequency for the oxygen-processed thicker BCZT700 and BCZT800 films. The dielectric constant of the BCZT films is almost remains unchanged as frequency is increased. BCZT700 film showed the dielectric constant of 530 at the frequency of 500 kHz whereas the BCZT800 film showed the dielectric constant of 598 at the same frequency. However, the dielectric loss of the films is slightly increased as the frequency is increased. Although the dielectric loss is increased slightly with the frequency the loss of the thicker BCZT films is comparable with its bulk ceramic counterpart [15]. BCZT700 film showed the dielectric loss of 0.033 even at the frequency of 500 kHz whereas the BCZT800 film exhibited the loss of 0.026 at the same frequency.

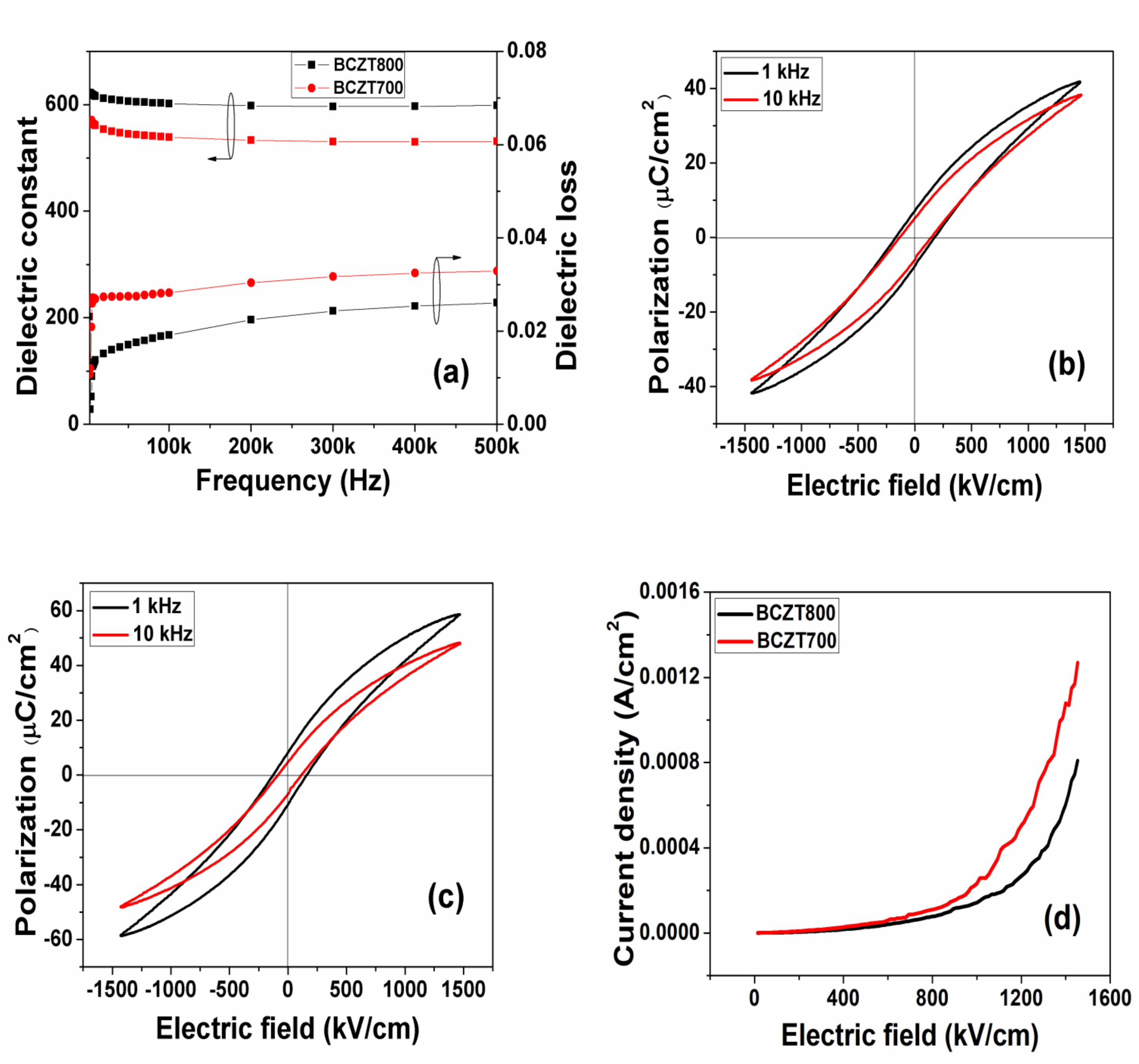

Fig. 7.3 (a) Variation of dielectric constant and loss with frequency for the oxygen-processed thicker BCZT films, (b) P-E hysteresis loops of the BCZT700 film, (c) P-E hysteresis loops of BCZT800 film and (d) leakage current density as a function of electric field for the oxygen-processed thicker BCZT films.

Fig. 7.3 (b) and 7.3 (c) presents the P vs. E hysteresis loops recorded at 1450 kV/cm electric field and at the frequencies of 1 kHz and 10 kHz for thicker BCZT700 and BCZT800 films. The occurrence of P vs. E hysteresis loop (non-linear variation in polarization with the applied electric field) for these films confirms the ferroelectric nature of the BCZT films. Both P_{max} and P_r of the films are decreased as the switching frequency is increased. BCZT700 film showed P_{max} of 41 μC/cm^2 and 2P_r of 14.8 μC/cm^2 whereas the BCZT800 exhibited P_{max} of 58 μC/cm^2 and 2P_r of 18.9 μC/cm^2 at an applied electric field of 1450 kV/cm and at 1 kHz frequency. The higher polarization of the thicker BCZT800 films is attributed to its bigger size grains as compared to the BCZT700 film. BCZT700 film displayed coercivity (2E_c) of 344 kV/cm at 1 kHz switching frequency whereas the same for BCZT800 is 288 kV/cm at the same frequency. The higher E_c for the BCZT700 film is attributed to the smaller size grains [14]. It is well known that low temperature crystallized films are with smaller size grains as compared to the films that were crystallized at higher temperatures. Energy storage properties (ESD and ESF) of the thicker BCZT films were investigated to determine energy storage ability of the BCZT capacitors. The ESD and ESF of the films were calculated from the P vs. E hysteresis loops using the equations (1.7) and (1.8). The thicker BCZT700 films displayed the ESD of 19.87 J/cm^3 and ESF of 62 % at the frequency of 1 kHz whereas the BCZT800 showed the ESD of 27.53 J/cm^3 and ESF of 63 % at the same switching frequency (Table 7.1). The difference in ESD for the BCZT films is due to higher polarization of BCZT800 than the BCZT700 film.

The thicker oxygen-processed BCZT films showed very low leakage current densities (J). The Fig. 7.3 (d) shows the leakage current density as a function of applied electric field for the thicker BCZT films. The BCZT700 film showed the leakage current densities of 2.6 x 10^{-6}, 4 x 10^{-5}, 2.3 x 10^{-4} and 1.27 x 10^{-3} A/cm^2 at the applied electric fields of 100, 500, 1000 and 1450 kV/cm, respectively. Whereas the BCZT800 film exhibited the leakage current densities of 1.4 x 10^{-6}, 2.7 x 10^{-5}, 1.4 x 10^{-4} and 8.1 x 10^{-4} A/cm^2 at the electric fields of 100, 500, 1000 and 1450 kV/cm, respectively. The leakage current densities of these films are much lower as compared to the PZT films, and the BCZT films with the same composition [16, 17]. Moreover, from the electrical property measurements it was observed that these thicker BCZT films showed higher dielectric breakdown strength (~1450 kV/cm).

Table 7.1 Electrical properties of thicker BCZT films.

Film	**ε_r at 500 kHz**	**Loss at 500 kHz**	**P_{max} (μ C/cm^2)**	**$2P_r$ (μ C/cm^2)**	**$2E_c$ (kV/cm)**	**ESD (J/cm^3) at 1 kHz**	**ESF (%) at 1 kHz**	**J (A/cm^2) at 500 kV/cm**
BCZT700	530	0.033	41	14.8	344	19.87	62	4 x 10^{-5}
BCZT800	598	0.026	58	18.9	288	27.53	63	2.7 x 10^{-5}

7.3.3 Nano-mechanical property measurements

Nanoindentation experiments on the ~750 nm thick BCZT films were performed by using a Berkovich tip with radius ~60 nm. Each indentation measurement consist of three steps: (i) loading the indenter up to peak load of 5mN in 30 sec (ii) holding the indenter for a period of 10 sec at the peak load followed by (iii) unloading in 30 sec as shown in Fig. 7.4 (a). During the indentation the load and depth are continuously measured as shown in Fig.7.4 (b). The theoretical reduced modulus, E_r, can be calculated from the equation (7.1) where E_1 and ν_1 are the elastic modulus and poisson’s ratio for the sample and E_2 and ν_2 are the elastic modulus and poisson’s ratio for the tip.

$$\frac{1}{E_r} = \frac{(1-\nu_1^2)}{E_1} + \frac{(1-\nu_2^2)}{E_2} \qquad (7.1)$$

The reduced modulus and hardness (H) were then calculated by the typical Oliver-Pharr method [18]. The reduced modulus was calculated by equation (7.2):

$$E_r = \frac{S\sqrt{\pi}}{2\beta\sqrt{A}} \qquad (7.2)$$

Where, A is the projected contact area, β is a constant which depends on the geometry of the indenter, E_r is the reduced modulus; S is the contact stiffness, calculated by dP/dh, which is calculated as the differential value of P(h) at the maximum indentation depth. The hardness was calculated by the equation (7.3).

$$H = \frac{P_{max}}{A} \qquad (7.3)$$

Where P_{max} is the maximum indentation load and A is the projected contact area.

It was reported earlier that any discontinuity in the load–displacement curve indicates the flaws *e.g.* voids, cracks, delaminations, inhomogeneous packing density etc. present in the film [19]. In the present experiment it is observed that there is no major discontinuity in the load–displacement curve. The cyclic loading at the same position provides valuable information regarding variation of hardness and elastic modulus with the indentation depth. The load-time plot (Fig. 7.4 (a)) which shows sinusoidal profile of load applied on monotonously increasing load during loading cycle in order to determine elastic modulus and hardness as a function of indentation depth. Fig. 7.4 (c) and Fig. 7.4 (d) shows the curves of hardness and elastic modulus versus indentation depth for thicker BCZT films annealed at 700 and 800 °C which were plotted directly from the data obtained for each cycle.

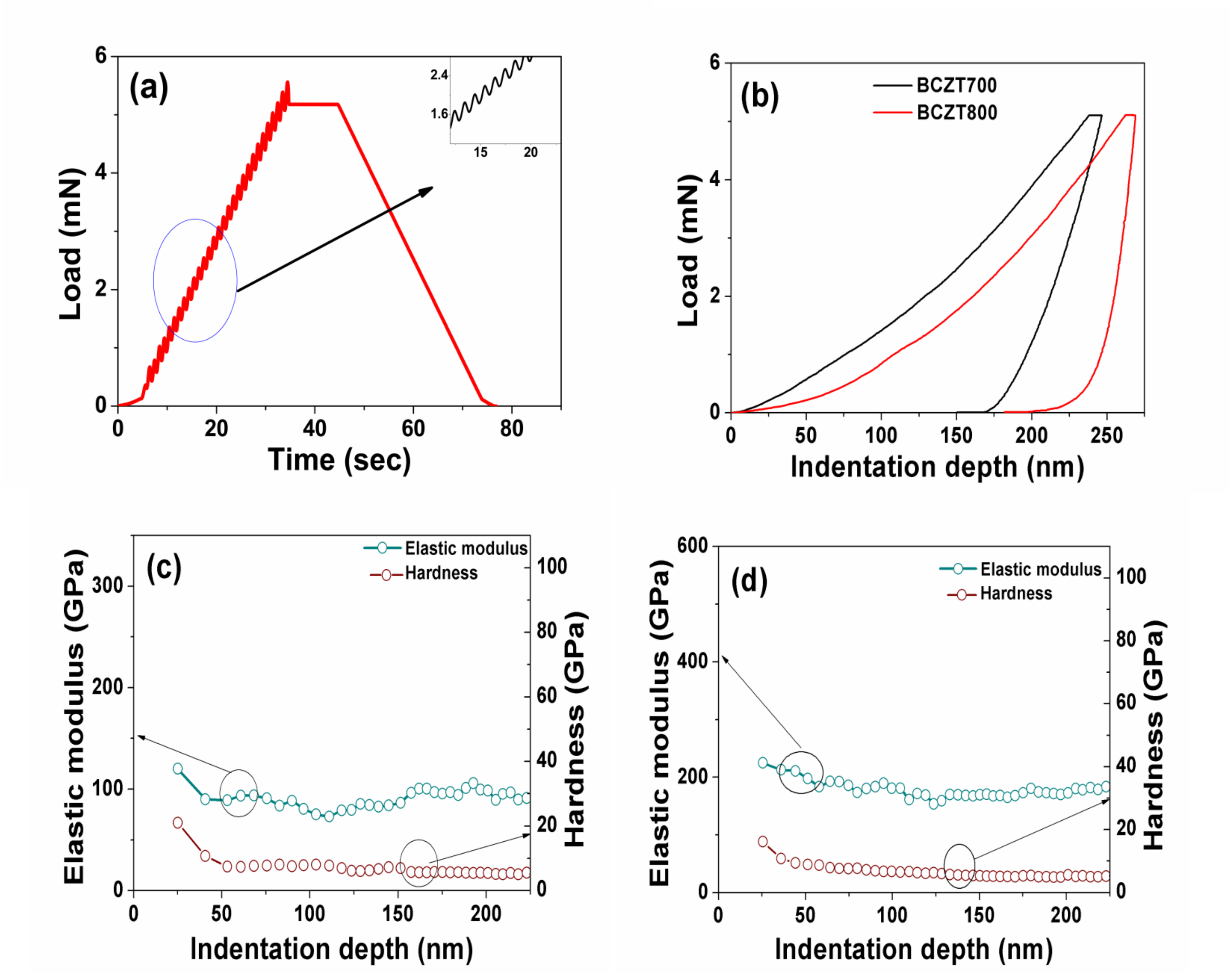

Fig. 7.4 (a) Load-time plot which showing sinusoidal signal applied on monotonously increasing load during loading cycle, (b) typical load-indentation depth curves for the thicker BCZT films annealed at 700 and 800 °C (c) variation of hardness and elastic modulus with indentation depth for BCZT700 and the same for (d) BCZT800 films.

The measured hardness and elastic modulus of the 700 ^{o}C annealed BCZT film are 5.2±0.3 GPa and 87.3±2.6 GPa. The same for the 800 ^{o}C annealed film are 3.9 ±1.02 GPa and 227±28 GPa. The 800 ^{o}C annealed film showed reasonably higher young's modulus than that of the 700 ^{o}C annealed film. Since, for the ionic BCZT material, bonding is de-localized by nature and therefore its mechanical properties are greatly influenced by extrinsic factors such as impurities, precipitates, boundaries (grain boundary, phase boundary and also at their intersection) etc. [20]. It has been well reported in literature that the stresses are concentrated at these boundaries and therefore, the stiffness is reduced as the cracks are easier to generate near these areas [21]. Thus, the films with relatively larger grain size (due to annealing at higher temperatures) or with relatively less grain boundaries are tend to have lower stress concentrations which in turn results in an increase in their mechanical properties [22]. This improvement in mechanical properties of the films annealed at 800 °C as compared to that annealed at 700 °C, cannot be attributed to the increase in crystallinity as no such noticeable change is seen from the XRD patterns (Fig. 1 (a)).

One important characteristic that influences the determination of film's hardness during nanoindentation process is the substrate that the film is deposited on. When probing the film the substrate and the film are both compressed and act to retard the indenter's motion. That is why conventionally the maximum depth of penetration is kept typically less than 10% to minimize the influence of the substrate during the measurement (and also more than 10% of surface roughness). However, in the present nanoindentation measurements it can be seen that hardness variation is almost negligible with indentation depth.

7.4 Conclusions

BCZT films of ~750 nm thickness were deposited on platinum coated silicon substrates by sol-gel deposition technique using PVP additive in oxygen-rich atmosphere. The appearance of P vs. E hysteresis loop i.e. the nonlinear behavior of the polarization with electric field confirms the occurrence of ferroelectric domain switching. The thicker BCZT800 film showed P_{max} of 58 $\mu C/cm^2$ and $2P_r$ of 18.9 $\mu C/cm^2$. ESD of 27.53 J/cm^3 and ESF of 63% were exhibited by the same film. The BCZT700 and BCZT800 films showed very low leakage current density and low dielectric loss. The dielectric loss of these thicker films is comparable to its bulk ceramic counterpart. Moreover, these films exhibited higher breakdown strength (1450 kV/cm). Nanoindentation was performed on the deposited films annealed at 700 and 800 ^oC temperatures to evaluate the nano-mechanical properties and the results could be correlated to the micro-structural properties of the films. The thicker BCZT800 film showed higher elastic modulus (227±28 GPa) than the BCZT700 film. The higher elastic modulus of BCZT800 film is attributed to its bigger size grains.

7.5 References

1. S. M. Spearing, Acta. Mater., **48** (2000) 179–96.
2. N. Ledermann, P. Muralt, J. Baborowski, S. Gentil, K. Mukati, M. Cantoni, A. Seifert, N. Setter, Sens. Actuators A-Phys., **105 [2]** (2003) 162–70.
3. R. Xu, S. Trolier-McKinstry, W. Ren, B. Xu, Z. L. Xie, K. J. Hemker, J. Appl. Phys., **89** (2001) 1336-1348.
4. D. L. Polla, L. F. Francis, Annual Rev. Mater. Sci., **28** (1998) 563-597.
5. J. Zhou, T. McMcollough, S. C. Mantell, S. Zurn, Proc. 13th Symp. On 'Microelectronics',Minneapolis, MN, USA, June 1999, IEEE, 153–157.

6. P. Delobelle, G. S. Wang, E. F. Blanc, D. Remiens, Surf. Coat. Tech., **201** (2006) 3155-62.
7. S. R. Jian, H. W. Chang, Y. C. Tseng, P. H. Chen, J. Y. Juang, Nanoscale Res. Lett., **8** (2013) 297.
8. D. F. Bahr, J. S. Robach, J. S. Wright, L. F. Francis, W. W. Geraberich, Mater. Sci. Eng. A., **A259** (1999) 126.
9. X. J. Zheng, Y. C. Zhou, J. Y. Li, Acta Mater., **51** (2003) 3985– 3997.
10. X. J. Zheng, Y. C. Zhou, J. M. Liu, A. D. Li, Surf. Coat. Tech., **176** (2003) 67–74.
11. W. Vincent, D. Patrick, L. M. Patrice, J. Eric, C. Manue, Sens. Actuat. A, **96A [2–3]** (2002) 157–166.
12. Z. L. Cai, Z. M. Wang, H. H. Wang, Z. X. Cheng, B. W. Li, X. L. Guo, H. Kimura, A. Kasahara, J. Am. Ceram. Soc., **98[1]** (2015) 114–118.
13. Z. M. Wang, Z. L. Cai, K. Zhao, X. L. Guo, J. Chen, W. Sun, Z. X. Cheng, H. Kimura, B. W. Li, G. L. Yuan, J. Yin, Z. G. Liu, Appl. Phys. Lett., **103** (2013) 071902.
14. Z. M. Wang, K. Zhao, X. L. Guo, W. Sun, H. L. Jiang, X. Q. Han, X. T. Tao, Z. X. Cheng, H. Y. Zhao, H. Kimura, G. L. Yuan, J. Yin, Z. G. Liu, J. Mater. Chem. C., **1** (2013) 522-530.
15. S. Rangaswamy Reddy, V. V. Bhanu Prasad, Pawan Kumar, K. Prabahar, Vishnu Shanker, Subir Roy, J. Mater. Sci., Mater. Elect. **29 [14]** (2018) 12451-12456.
16. L. Pintilie, I. Vrejoiu, D. Hesse, G. Lerhun, M. Alexe, Phys. Rev. B. **75** (2007) 104103.
17. Y. Chen, T. Y. Zhang, Q. G. Chi, J. Q. Lin, X. Wang, Q. Q. Lei, J. Alloys Compd., **663** (2016) 818-822.
18. W. C. Oliver, G. M. Pharr, J. Mater. Res., **7** (1992) 1564–1583.

19. Y. K. Vayunandana Reddy, D. Mergel, S. Reuter, V. Buck and M. Sulkowski., J. Phy. D Appl. Phys., **39** (2006**)** 1161.

20. F. Gao, J. He, E. Wu, S. Liu, D. Li, S. Zhang, Y. Tian, Phys. Rev. Lett., **91** (2003) 015502.

21. D. B. Bogy, J. Appl. Mech., **38** (1971) 377.

22. I. V. Belova, G. E. Murch, J. Phys. Chem. Solids., **64** (2003) 873.

Chapter 8

Conclusions and future scope of the work

8.1 Conclusions

In this thesis lead free ferroelectric $Ba_{0.85}Ca_{0.15}Ti_{0.9}Zr_{0.1}O_3$ (BCZT) system was investigated as in the form of bulk ceramics, thin films and thicker films by employing sol-gel technique. The crystal structure, microstructure and electrical properties of these ceramics and films were systematically studied. Excellent electrical properties were obtained in this work on the BCZT system as compared with previous studies reported in literature. The conclusions of these studies are summarized as follows:

- BCZT nano-powders and BCZT bulk ceramics showed perovskite crystal structure with the coexistence of the rhombohedral and tetragonal phases at room temperature. SAED patterns obtained by the HRTEM further confirmed the perovskite structure for the BCZT nano-powders. The size distribution for majority of the nano-particles is 10-50 nm. However, the nano-particle distribution also showed some bigger nano-particle agglomerates of size up to 250 nm.
- BCZT bulk ceramics sintered at 1350 ^{o}C temperature showed high density, better electrical properties and improved Curie point (100 ^{o}C). High converse d_{33} of 680 pm/V, P_r of 6 μC/cm^2 and room temperature dielectric constant (ε_r) of 2400 were exhibited by these BCZT ceramics.
- Microwave sintered BCZT ceramics showed higher T_m, better density, improved dielectric and energy storage properties as compared to the conventional sintered

ceramics. The high T_m of the microwave sintered BCZT ceramics is attributed to its dense microstructure with fine grains. Room temperature ε_r of 2090, dielectric loss of 0.02, ESD of 0.13 J/cm^3 and T_m of 115 ^{o}C were obtained for the microwave sintered BCZT ceramics.

- BCZT thin films as well as thicker films deposited by the sol-gel technique exhibited perovskite crystal structure with the mixture of rhombohedral and tetragonal phases at room temperature.
- Air-processed 200 nm thick BCZT thin films crystallized at 800 ^{o}C showed improved grain growth with bigger size grains, and better electrical properties than the films crystallized at 700 ^{o}C. The BCZT800 film exhibited high dielectric constant of 1550±50, tunability of 50%, P_r of 25±1 μC/cm^2 and ESD of 17 J/cm^3. Interestingly this film displayed very high piezoelectric response with converse d_{33} of ~250 pm/V.
- Processing of BCZT films in oxygen-rich atmosphere significantly reduced the oxygen vacancy concentration in the films which led to very slim P vs. E loops. Oxygen-processed 200 nm thick BCZT films showed very low dielectric loss, large dielectric breakdown strength, low P_r, substantially low coercivity and superior energy storage properties than the air-processed BCZT thin films.
- BCZT800 film processed in oxygen-rich atmosphere showed the dielectric loss of 0.028, P_{max} of 106 μC/cm^2, P_r of 12.9 μC/cm^2, ESD of 64.8 J/cm^3 and ESF of 73%. Furthermore, the oxygen-processed BCZT800 films displayed excellent fatigue resistance by retaining 99% of polarization even after 10^{10} switching cycles.
- The oxygen-processed thicker BCZT films (thickness of ~750 nm) exhibited high dielectric breakdown strength and good ferroelectric properties. BCZT800 film showed

P_{max} of 58 µC/cm^2 and 2P_r of 18.9 µC/cm^2 at an applied electric field of 1450 kV/cm and at 1 kHz frequency. Apart from this, these films exhibited very low dielectric loss and leakage current density.

- The thicker BCZT800 film showed significantly higher elastic modulus than that of the film annealed at 700 ^{o}C. The BCZT800 film displayed hardness of 3.9±1.02 GPa and elastic modulus of 227±28 GPa. The higher elastic modulus of this film is attributed to it's the bigger size grains and low porosity.

8.2 Future scope of the work

In this work the electrical properties and Curie point for the BCZT ceramics were improved by employing the optimized sol-gel synthesis route and by changing the sintering technique. Moreover, the processing temperature of the BCZT ceramics is noticeably reduced. Furthermore, the electrical and nano-mechanical properties of the BCZT films were significantly enhanced by synthesizing the films through the modified sol-gel route and by the modification of the processing atmosphere. However, to our opinion further research efforts are necessary for the improvement of the electrical properties and T_C of the BCZT system. The possibilities to improve the system are as follows,

- Processing of BCZT bulk ceramics with high degree of texture through template grain growth method. Texturing enhances the ferroelectric, piezoelectric and dielectric properties since it increases the fraction of domains oriented along the applied electric field.
- Development of BCZT bulk ceramics and films by the replacement of A or B site cations with donor dopants. Donor dopants improve the ferroelectric softening, remanent

polarization, dielectric and piezoelectric properties by increasing the domain wall mobility.

- Although improved T_C obtained for the BCZT ceramics but it is low as far as practical applications of this system are concerned. Therefore, it is required to increase the T_C of the BCZT system without degradation of electrical properties in order to utilize the system for high temperature piezoelectric applications. For this purpose, the compounds such as $(K,Na)NbO_3$, $Bi(Mg,Ti)O_3$ and $BiScO_3$ may be helpful to synthesize solid solutions with the BCZT system.
- Growth of BCZT thin films on the seed layer to decrease the crystallization temperature. Furthermore, development of BCZT coatings on nickel electrodes to reduce the cost of multilayered capacitors.
- Development of relaxor-behavior induced BCZT ceramics and films by increasing the zirconium content (up to 0.25 moles) in the composition to enhance the energy storage properties. It is known that relaxor-ferroelectric material displays better energy storage properties than the normal ferroelectric material.
- BCZT ceramics and films could be utilized for the replacements of their PZT counterparts in some applications which reduce the lead toxicity in the environment. Furthermore, BCZT ceramics may be utilized for the biomedical applications due to good biocompatibility and low cytotoxicity.
- BCZT bulk ceramics may be considered for low temperature piezoelectric applications, and for capacitor applications.
- BCZT thin films with high d_{33}, ESD and with excellent polarization fatigue may be utilized for pulse power applications, and for MEMs.

List of publications

Journals

- **S. Rangaswamy Reddy**, V. V. Bhanu Prasad, Sandip Bysakh, Vishnu Shanker, Neha Hebalkar and Subir Roy, Superior energy storage performance and fatigue resistance in ferroelectric BCZT thin films grown in an oxygen-rich atmosphere, ***J. Mat. Chem. C., 2019, 7, 7073.***
- **S. Rangaswamy Reddy**, V. V. Bhanu Prasad, Sandip Bysakh, Vishnu Shanker, Joydip Joardar and Subir Roy, Ferroelectric and piezoelectric properties of $Ba_{0.85}Ca_{0.15}Ti_{0.90}Zr_{0.10}O_3$ films in 200 nm thickness range, ***J. Am. Ceram. Soc., 2019, 102, 1277-86.***
- **S. Rangaswamy Reddy**, V. V. Bhanu Prasad, Pawan Kumar, K. Prabahar, Vishnu Shanker and Subir Roy, Microwave sintered lead free ferroelectric BZT-50BCT ceramics with higher Curie temperature and improved dielectric properties, ***J. Mater. Sci. Mater. Elect., 2018, 29(14), 12451-12456.***
- Subir Roy, Rajalaxmi Maharana, **S. Rangaswamy Reddy**, Sarabjit Singh, Pawan Kumar, T. Karthik, Saket Asthana, V.V. Bhanu Prasad, and S.V. Kamat, Structural, ferroelectric and piezoelectric properties of chemically processed, low temperature sintered piezoelectric BZT-BCT ceramics, ***Mater. Res. Express., 2016, 3, 035702.***

Manuscript under process

- Microstructure, nano-mechanical and ferroelectric properties of chemical solution deposited lead free ferroelectric BCZT films.

Journal (Not a part of this thesis work)

- Subir Roy, **S. Rangaswamy Reddy**, P. Sindhuja, Dipak Das, V. V. Bhanu Prasad, $AlPO_4$-C composite coating on Ni-based alloy substrates for high emissivity applications: Experimentation on dip coating and spray coating, ***Defence Science Journal., 2016, 66(4), 425.***

Patent filed (Not a part of this thesis work)

- Patent entitled "A method to develop high temperature stable high emissivity ceramic coating" has been filed with the ***application no. 201811047860.*** (Inventors: Subir Roy, **S. Rangaswamy Reddy,** V. V. Bhanu Prasad).

Contributions to international conferences

- **S. Rangaswamy Reddy**, Rajalaxmi Maharana, Manivel Raja, V. V. Bhanu Prasad and Subir Roy, 'High temperature stable carbon coated metal nano-particles in amorphous $AlPO_4$ based matrix for magnetic and catalytic applications', International conference on magnetic materials and applications (ICMAGMA-2017), Leonia Resorts, Hyderabad.
- **S. Rangaswamy Reddy**, V. V. Bhanu Prasad, Vishnu Shanker and Subir Roy, 'Structural and piezoelectric characterizations of the sol-gel derived lead free BCZT thin films', International conference on technologically advanced materials (ICTAM) and Asian meeting on ferroelectricity (AMF10), 2016, University of Delhi, New Delhi.
- Subir Roy, **S. Rangaswamy Reddy**, Atul Kumar, V. V. Bhanu Prasad and S. V. Kamat, 'Development of ferroelectric BZT-BCT thin films by chemical solution deposition

method’, International conference on ceramic and advanced materials for energy and environment (CAMEE-2015), Christ University, Bangalore**.**